# HIGH RESOLUTION MICROWAVE SPECTROSCOPY OF ULTRA COLD RYDBERG ATOMS AS A PROBE OF ELECTRIC AND MAGNETIC FIELDS

by

Parisa Bohlouli Zanjani

A thesis
presented to the University of Waterloo
in fulfillment of the
thesis requirement for the degree of
Master of Science
in
Physics

Waterloo, Ontario, 2003

I hereby declare that I am the sole author of this thesis. This is a true copy of the thesis, including any required final revisions, as accepted by my examiners.

I understand that my thesis may be made electronically available to the public.

# Abstract

In highly excited Rydberg atoms, the excited electron is in a large, loosely bound orbit. Hence, in contrast with the ground states, the Rydberg states are very sensitive to external electric field and can be ionized in rather weak fields. The low ionization threshold of Rydberg states results in effective state-specific detection by the selective field ionization technique.

In this thesis, high-resolution spectroscopy of Rydberg states of Rubidium using millimeter wave transitions and selective field ionization has been used as a probe of external electric and magnetic fields. Laser cooling and trapping techniques in a magneto-optical trap (MOT) are employed to have a high density and narrow velocity distribution for the atomic sample.

In this work the magnetic field inhomogeneity inherent in a MOT is minimized and the stray electric field present at the trap region is compensated in order to have resolved spectra.

The Stark line broadening of the spectra obtained in this work may be used to determine the electric field distribution in an expanding ultra-cold neutral plasma.

**Acknowledgements**

The development and completion of this work would not have been possible without the support and encouragement of a number of individuals to whom I am deeply in gratitude. First, I would like to sincerely thank my supervisor Dr. James D. D. Martin for his valuable insights, enthusiasm, support and encouragements. I greatly appreciate the time that he spent and his effort for guiding me through this research experience and providing me with invaluable feedback on this thesis.

I would like to extend my grateful acknowledgment to my M.Sc. thesis examination committee: Dr. W.-K. Liu and Dr. Donna Strickland for their time and comments on this work.

My special thanks to administrative staff of the Physics Department, specially Judy McDonnell and Margaret O'Neill for their help and assistance. I would also like to thank Andy Colclough in the Physics Student Machine Shop for his help, suggestions, and mechanical expertise. Many thanks to all members of the Laser Cooling and Trapping group, Koroush Afrousheh, Maria Fedorov, Joel Keller, Ashton Mugford, and Poya Haghnegahdar for their assistance and support and also Dhrov Vagale for providing many comments and suggestions throughout the editing process.

I am extremely lucky to have met a remarkable group of friends over the last 2 years. Your contributions are many, and I hope that these bonds continue to strengthen after our time at Waterloo.

A very special thanks to my family for their life long support in helping me to succeed. I would like to thank my mother for the many kind words that kept me positive through many hard times. She taught me how to be patient and strong in the face of adversity. A warm thank you to my father who inspired me with the love of science. His intelligence, self reliance, self determination and love for nature have always been guiding principles to me. Thank you both very much, you are far beyond any appreciation!

I would also like to thank my brother, Hamid Reza, and my sisters Nazila, Sanaz, and Golnaz. Their friendship, understanding, and continuous encouragement was priceless.

And finally, special thanks to my husband, Ali. His intellect, knowledge, and loving inspiration was an incredible assistance to me during my graduate study. He put up with lots of late nights and was always supportive. Without your care, love and understanding, I would never

have managed to continue this work.

# Contents

# List of Tables

# List of Figures

# Chapter 1

# Introduction

## 1.1 Rydberg Atoms

A Rydberg atom is an atom with a single valence electron in a high principal quantum number, $n$, state. Brief discussions of Rydberg atoms can be found in Refs. [1] and [2].

The excited valence electron is shielded from the electric field of the nucleus by the electrons in the ion core of a Rydberg atom. Therefore the excited electron sees the nucleus with only one proton, like the electron of a Hydrogen atom. The energy levels of Hydrogen can be obtained from the Rydberg formula:

$$E = \frac{-R_y}{n^2} \tag{1.1}$$

where for an atom with nuclear mass $M$, $R_y$ is,

$$R_y = M(M + m_e)^{-1} R_\infty \tag{1.2}$$

with [3],

$$R_\infty = \frac{m_e c \alpha^2}{2h} = 10\ 973\ 731.568\ 62(9)\ \ \mathrm{m}^{-1} = 13.605\ 698(4)\ \ \mathrm{eV}\,. \tag{1.3}$$

In the above equations, $m_e$ is the mass of the electron and $R_\infty$ is the Rydberg constant. Since the electron is much lighter than the proton, $R_y \approx R_\infty$.

The energy levels of atoms other than Hydrogen deviate from the relation in Eq. 1.1. When

the valence electron is far from the ionic core (high angular momentum, $l$, states) it is only sensitive to the net charge and behaves like the Hydrogen atom. On the other hand, when the valence electron comes near the ionic core (low-$l$ states) it can polarize and penetrate the ionic core. To adjust the Rydberg equation for this penetration of the inner core electrons, a correction term called the "quantum defect" is introduced. The Rydberg relation is modified to include the quantum defect of the element being studied,

$$E = \frac{-R_y}{(n - \delta_l)^2} \tag{1.4}$$

where $\delta_l$ is the quantum defect of the state of angular momentum $l$.

The quantum defect is different for different angular momentum states. For low-$l$ states the penetration and polarization of the core electrons by the valence electron lead to large quantum defects.

The radius of the charge distribution of the valence electron scales as $n^2$. Thus, the electric dipole moment scales as $n^2$. This leads to high induced transition probabilities. If the initial state $n$ and the final state $n'$ are close to each other, the energy difference, $E_n - E_{n'}$, scales as $n^{-3}$. Therefore Rydberg atoms strongly absorb microwave radiation over a certain range of relatively high $n$.

The large Rydberg atom orbits have longer natural lifetimes than those of less excited atoms. For Rydberg states other than Hydrogen the lifetimes scales as $n^3$ for low-$l$ states and as $n^5$ for high-$l$ states [4].

In the Rydberg states, the excited electron is in a large, loosely bound orbit. Hence, in contrast with the ground states, the Rydberg states are very sensitive to external electric field and can be ionized in rather weak fields. For example, the classical field for ionization of the ground state of atomic hydrogen is $3.2 \times 10^8\,\mathrm{V/cm}$, while the field required to ionize a Rydberg state with $n = 47$, is $65.9\,\mathrm{V/cm}$ - which can be obtained easily in the laboratory. The low ionization threshold of Rydberg states results in effective detection of such states by the selective field ionization technique.

However, before the invention and development of frequency tunable dye lasers in the early 1970's, it was difficult to generate Rydberg atoms in the laboratory. Narrow bandwidth tunable

dye lasers made it possible to selectively populate highly excited states, hence spectroscopic studies of Rydberg states became more common.

## 1.2 Rydberg Atom Spectroscopy Using Microwave Transitions

High-resolution spectroscopy of Rydberg atoms using millimeter wave (mm-wave) transitions has been used as a probe of external electric or magnetic field and also for precise measurement of fine and hyperfine structure intervals.

W. E. Lamb *et al* (1956) [5] observed the first mm-wave induced transitions between the excited states of hydrogen. The $3s_{1/2} \rightarrow 3p_{1/2}, 3s_{1/2} \rightarrow 3p_{3/2}$, and $3p_{3/2} \rightarrow 3d_{5/2}$ transitions were observed and the fine structure of Hydrogen atoms in the $n = 3$ states were measured.

P. Goy *et al*. (1981) [6] used double-resonance spectroscopy of Rydberg atoms of Cesium with mm-waves and obtained relatively precise values for quantum defects in the $s$, $p$, $d$, and $f$ Rydberg levels (for principal quantum number, $n = 23 - 45$). They measured the transition frequencies between two states with $n \geq 20$ and $l \leq 3$, with an accuracy of about a MHz. Fine and hyperfine structures in these levels were also measured.

F. Merkt *et al*. (1998) [7] obtained a resolution of 250 kHz in the spectra of high Rydberg states of Argon for $n = 60 - 200$ in a double-resonance experiment. This resulted in more accurate effective quantum numbers and a more precise measurement of fine-structure intervals for $l \leq 3$.

W. Li *et al*. (2003) [8] observed two photon mm-wave transitions of cold Rydberg atoms of Rubidium in a magneto-optical trap (MOT), with 100 kHz spectral resolution. The accuracy of quantum defects for $s$, $p$, and $d$ states were improved by an order of magnitude. This was the first microwave study of Rydberg atoms obtained by laser cooling.

In the present experiments, the Rydberg states of the Rb atom are used. Rb is an alkali metal atom with 36 electrons in a closed core and one optically accessible valence electron. Laser cooling and trapping techniques in a MOT are employed to have a higher density and lower velocity distribution for the atomic sample. The valence electron of Rb can be optically excited from its ground state, $5s$, to the excited state, $5p$, by a cw diode laser also being used for cooling and trapping the atoms. It is subsequently excited to the Rydberg state, $47s$, by a

pulsed tunable dye laser and then to the $47p$ state by absorption of the microwaves.

## 1.3 Measuring Plasma Induced Electric Field Distributions Using mm-wave Spectroscopy of Cold Rydberg Atoms

The electric field distribution of an ultra-cold neutral plasma can be studied using a combination of laser-cooling and trapping methods together with Rydberg-atom spectroscopy. Highly excited Rydberg atoms are very sensitive to static and ac electric fields and can be used for the measurement of the plasma induced electric fields.

A definition of a plasma is given here. A plasma is an ionized gas. It contains free electrons and positive ions. The charged particles in a plasma exhibit collective effects. The distance at which the electron is shielded by the surrounding positive ions or vice versa, is the Debye screening length $\lambda_D$, and is given by [9],

$$\lambda_D = \sqrt{\epsilon_0 k_B T_e / e^2 n}. \tag{1.5}$$

Here $\epsilon_0$ is the electric permittivity of vacuum, $k_B$ is the Boltzman constant, $e$ is the elementary charge, $T_e$ is the electron temperature, and $n$ is the plasma density. An ionized gas is not a plasma unless the Debye length is smaller than the size of the system [9].

Until recently (1999) neutral plasma temperatures ranged from $10^{16}\,\mathrm{K}$ in a magnetosphere of a pulsar to $300\,\mathrm{K}$ in the earth's ionosphere. T. C. Killian *et al.* [10] were able to create a plasma with an electron temperature $T_e = 100$ mK, an ion temperature $T_e = 10\ \mu$K, and densities as high as $n = 2 \times 10^9\,\mathrm{cm}^{-3}$. This novel plasma was obtained by photoionization of laser-cooled Xenon atoms and is known as ultra-cold neutral plasma (UCNP).

Electric fields in dc and high frequency discharge plasmas have been diagnosed by the spectroscopy of Rydberg atoms [11], [12], and [13]. J. Neukammer *et al.* [14] used Rydberg atoms to measure and compensate weak static electric fields.

D. Feldbaum *et al.* [15] used Rydberg atom spectroscopy to study the electric field of an ultra-cold non-neutral plasma created in a MOT. The remaining neutral atoms in the ion plasma were excited to Rydberg states by a blue dye laser pulse. They measured the electric field in the cloud of cold $Rb^+$ ions using the electric field dependence of these transitions. Due to the laser

linewidth, electric fields lower than $\sim 12\,\mathrm{V}\,/\,\mathrm{cm}$, such as microfields, were not detectable. The macroscopic electric field of a plasma is the net field due to the continuous charge distribution, whereas microfields refer to the distribution of electric fields that are encountered due to the discrete charges in the plasma. For example, in a neutral plasma the macroscopic electric field is zero. However at a point in space nearby an individual electron or ion, the electric field is very high. The actual electric field is best described by a probability distribution known as the microfield.

In the experiments presented in this thesis, the high resolution spectroscopy of Rydberg states of laser cooled Rb atoms is studied by driving 'one photon' microwave transitions between the Rydberg states of $47s_{1/2}$ and $47p_{1/2}$. Microwave excitation instead of optical excitation makes it possible to have a high degree of control over pulse length, intensity and frequency. This is ideal for the detection of microfields.

In this experiment Rb atoms were first laser cooled and trapped in a MOT. Atom trapping in a MOT relies on magnetic field inhomogeneity. Therefore, spatial inhomogeneity of the energy levels of the atoms due to the magnetic field inhomogeneity inside MOT broadens the transition frequencies and limits the precision of spectroscopy. In this work, magnetic field inhomogeneity is minimized and the stray electric field present at the trap region is compensated in order to have resolved spectra.

## 1.4 Structure of Thesis

This thesis is organized as follows:

In chapter two, the experimental techniques that were used to built a MOT are described. Many of these techniques have been developed by others [16], [17], [18], [19], but they are included as a reference for future experiments.

In chapter three, the initial observations of microwave transitions are presented and the power broadening effect of the microwave field on the transitions is described.

In chapter four, a theoretical overview of the behavior of the ground state and Rydberg states of Rb in the presence of a magnetic field is discussed and the experimental data showing the effect of this field on the microwave transitions between adjacent Rydberg states are presented.

The experimental data related to the inhomogeneous magnetic field reduction is also presented in this chapter.

In chapter five, a theoretical review of the effect of an external electric field on atomic Hydrogen and alkali metal atoms such as Rb is given. The theoretically calculated energy shifts (Stark maps) of the Rb atom due to an external electric field are illustrated and the experimental data for compensating stray electric field is presented. Some of the experimental limitations encountered are presented. The Holtsmark distribution of plasma induced electric fields is also discussed in this chapter using two typical cold plasma densities [20], [10].

Chapter six contains the summary and a discussion of future work.

# Chapter 2

# Experimental Techniques

## 2.1 Doppler Cooling

The idea of Doppler cooling is to slow particle velocity using light pressure [21] by illuminating atoms from all directions with light tuned slightly below an atomic absorption line. This is illustrated for 1-D in Fig. 2-1.

Here a moving atom sees the light it moves towards Doppler shifted closer to resonance, whereas the light it moves away from is shifted away from resonance. Thus, the atom predominantly scatters photons from the direction that it is moving towards and is slowed down. Doppler cooling can be extended to 3-D by using six beams, forming three orthogonal standing waves. In our experiment Rubidium is loaded into a region where three pairs of counter propagating mutually orthogonal laser beams intersect. This configuration is sometimes referred to as optical molasses. An atom will see a viscous damping force, $F = -\alpha v$ from all directions, opposing its motion (Fig. 2-2).

Although optical molasses provides viscous damping, it is not a trap. The atoms are free to diffuse. Typically, a molasses contains ten times fewer atoms than a magneto-optical trap for similar beam powers [22]. A magneto-optical trap provides a spatially dependent force in addition to the optical molasses, resulting in a true neutral atom trap.

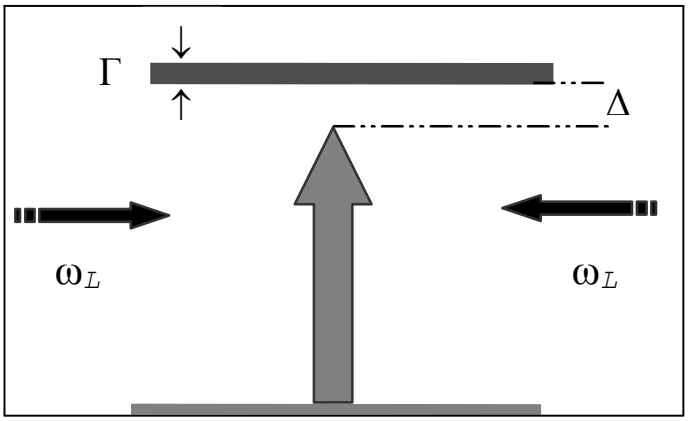


Figure 2-1: One-dimensional Doppler cooling. The frequency of the standing laser field $\omega_L$ is detuned by $\Delta$ from the atomic resonance, which has a linewidth $\Gamma$.

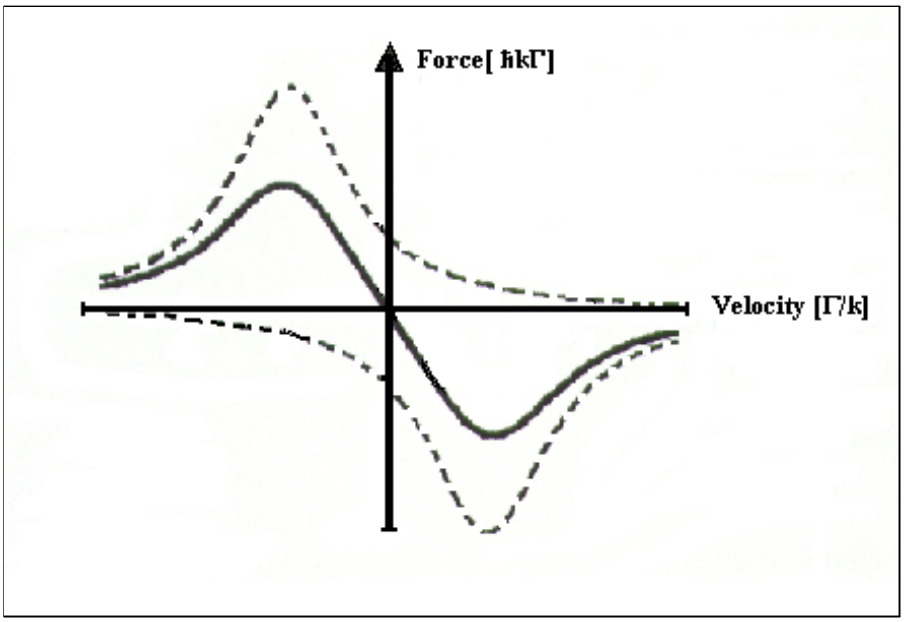


Figure 2-2: Velocity dependence of the optical damping force for 1-D optical molasses. The two dotted traces show the force from each beam, and the thick curve is the combined force, displaying viscous damping around $v = 0$ [21].

## 2.2 Magneto-Optical Trap (MOT)

A Magneto-Optical Trap (MOT) employs both optical and magnetic fields to trap neutral atoms (first demonstrated in 1987 [18]). It greatly reduces the random thermal motions of the atoms and makes it possible to measure energy level structure and excited state lifetimes with high accuracy.

The MOT consists of three orthogonal pairs of circularly polarized counter propagating laser beams and an anti-Helmholtz magnetic field $B = B(z)$ which is produced using two identical coils carrying opposite current. This trap has a single center where the magnetic field is zero (Fig. 2-3).

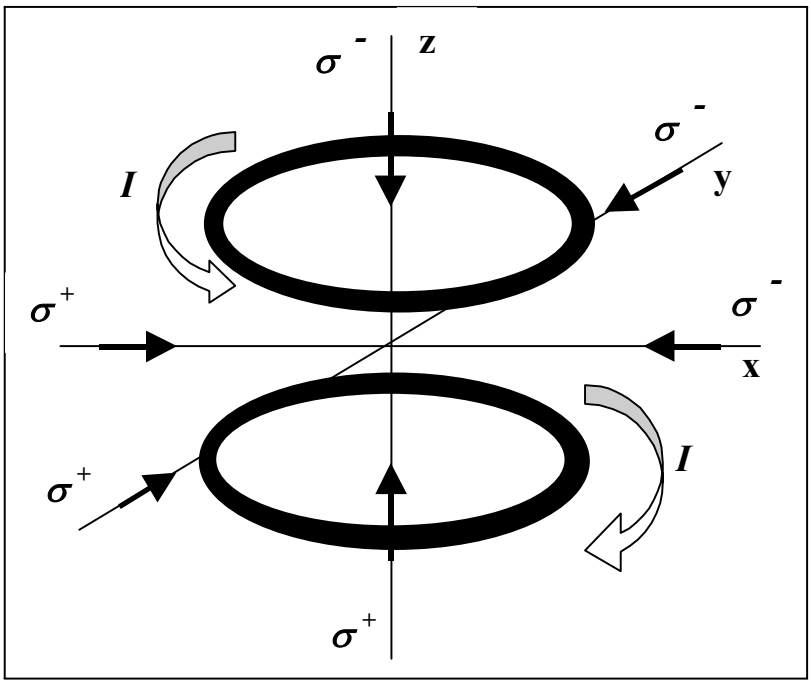


Figure 2-3: Schematic diagram of the anti-Helmholtz coils configuration of MOT and three orthogonal $\sigma^+\sigma^-$ standing waves. Since the currents in the two coils are in opposite directions, there is a $|B| = 0$ point at the center.

The idea is to use the circularly polarized light for optical molasses and add the magnetic field such that an atom which moves away from the origin is Zeeman shifted into resonance with a beam which pushes it back. Here, it is explained how this works using a simplified model of

an atom in 1-D.

A simple scheme for an atomic transition with $J_{\mathbf{g}} = 0 \longrightarrow J_{\mathbf{e}} = 1$ has three Zeeman components in a magnetic field. Because of the Zeeman shift, the excited state $M_{J_{\mathbf{e}}} = 1$ is shifted up for $B > 0$, whereas the state with $M_{J_{\mathbf{e}}} = -1$ is shifted down, as shown in Fig. 2-4.

In Fig. 2-4 two counter propagating laser beams of opposite circular polarization, each detuned below the zero field atomic resonance by $\delta$, are incident on the atoms.

At position $z_1$ in Fig. 2-4, the beams propagating in the $\pm z$ direction have $\sigma^{\pm}$ polarizations. Due to the electric dipole selection rules, $\Delta M_S = 0$ and $\Delta M_L = \pm 1$ for $\sigma^{\pm}$ polarizations (page 157 [23]), these beams (propagating in the $\pm z$ direction) drive $\Delta M_J = \pm 1$ transitions respectively. The magnetic field therefore tunes the $\Delta M_J = -1$ transition closer to the resonance and the $\Delta M_J = +1$ transition further out of resonance. If the polarization of the laser beam incident from the right is chosen to be $\sigma^-$ and correspondingly $\sigma^+$ for the other beam, then more light is scattered from the $\sigma^-$ beam than from the $\sigma^+$ beam. Thus, the atoms are driven toward the center of the trap where the magnetic field is zero. Similarly on the other side of the center of the trap an atom with $z < 0$, scatters more $\sigma^+$ photons, and is also pushed towards $z = 0$. In other words, atoms interact more with the laser field that pushes them back into the trap than with the laser field that pushes them out. The effect here operates in position-space and the atoms experience a restoring force $F = -kz$, whereas for molasses it operates in velocity-space. Since the laser is detuned below the atomic resonance, compression and cooling of the atoms is obtained simultaneously in a MOT. The MOT scheme can easily be extended to 3-D by using six instead of two laser beams.

### 2.2.1 Trap and Repump Lasers

Cooling and trapping alkali atoms in a MOT usually requires laser light at two frequencies, one for cooling and trapping and another one for repumping (Fig. 2-5). This is required since alkali atoms are not perfect two level systems. In the experiment presented in this text, $^{85}$Rb atom is used.

For cooling and trapping $^{85}$Rb in a MOT, the most common technique is used. The laser light is detuned a few line widths to the red of the $5^2S_{1/2}(F = 3) \longrightarrow 5^2P_{3/2}(F' = 4)$ resonance [25] (Fig. 2-5). The most important reason for choosing this transition is that an atom in the

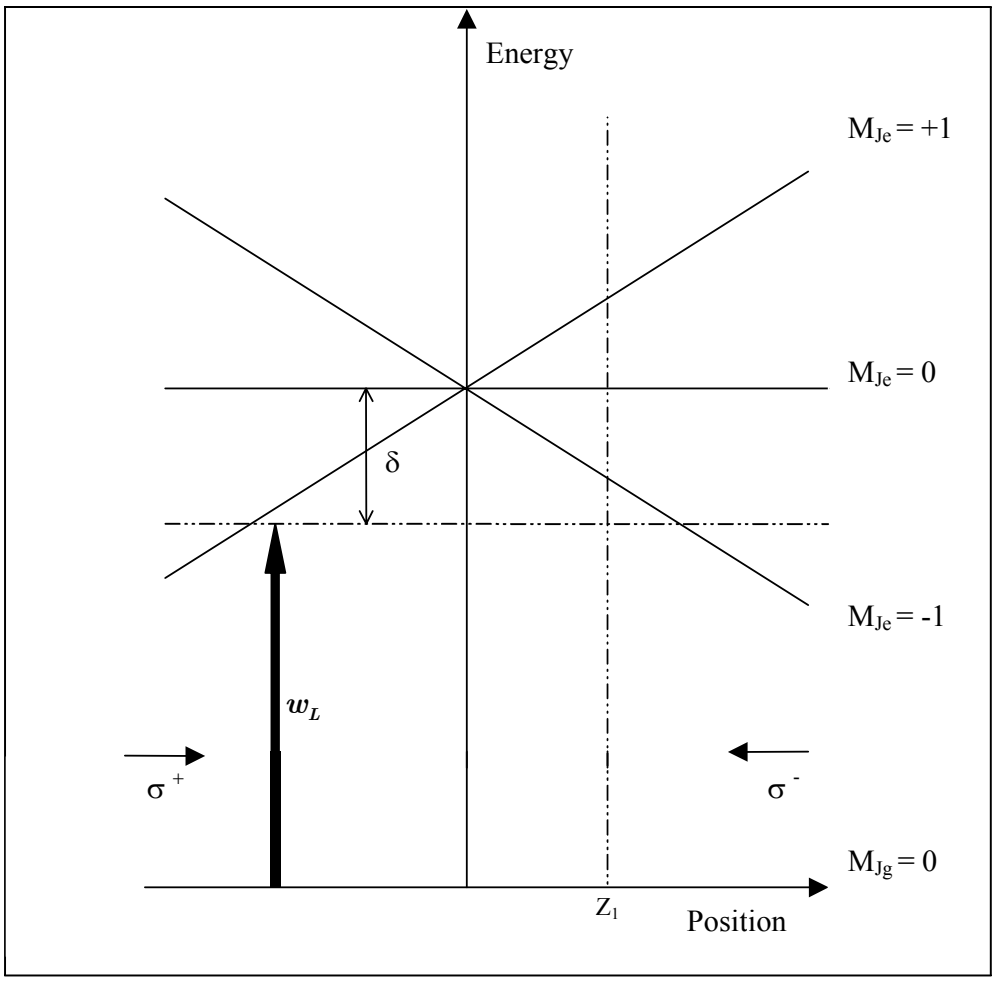


Figure 2-4: The magneto-optical trap in 1-D. The magnetic field changes linearly as a function of position. The horizontal dashed line shows the laser frequency seen by an atom at rest in the center of the trap. For an atom at $z = z_1$, the $\sigma^-$ beam, driving the $\Delta M_J = -1$ transition, is Zeeman shifted into resonance and pushes the atom back towards the center of the trap where $z = 0$.

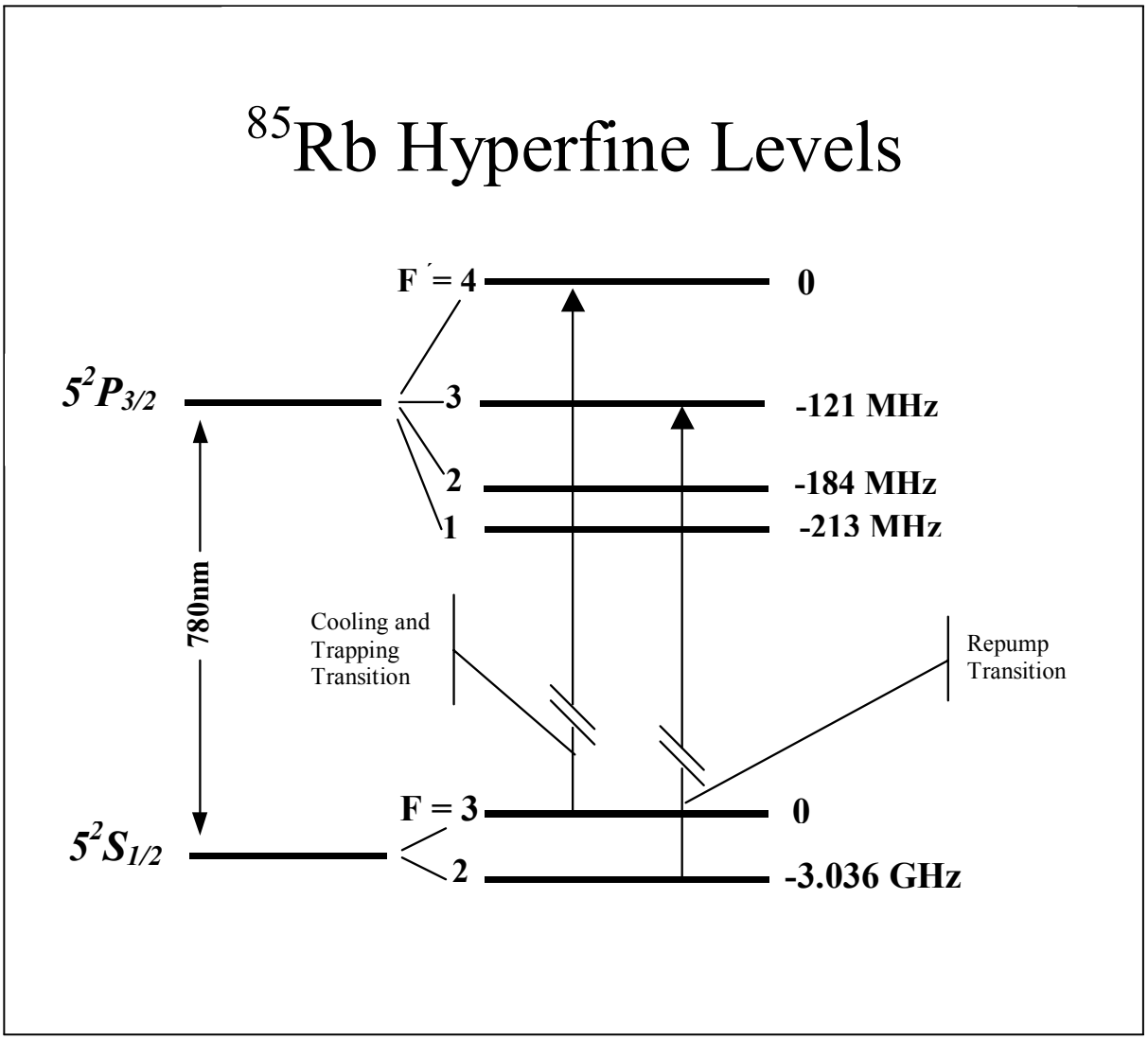


Figure 2-5: Hyperfine structure of the $5^2S_{1/2}$ and $5^2P_{3/2}$ states of $^{85}$Rb, showing the cooling, trapping and repump transitions (page 41 of [23], [24]).

$F' = 4$ excited state is only allowed to decay back to the $F = 3$ ground state, where it can be immediately reexcited.

Since the splitting of the two excited states $F' = 4$ and $F' = 3$ is very small (121 MHz, see Fig. 2-5), there is a probability that after absorbing a photon, $^{85}$Rb is excited to $F' = 3$ instead and drops out of the cooling cycle and ends up in the $5^2S_{1/2}(F = 2)$ state. Thus, a second laser system is needed to remove atoms from the $F = 2$ state by exciting the $F = 2 \longrightarrow F' = 2$ or 3 transition. From the $F' = 2$ or 3 states, the atom can decay back to the $F = 3$ state, where they will be trapped once again. Without a mechanism for removing atoms from the $F = 2$ state, the trap would cease to function. This second laser is referred to as the repump laser. It overlaps the intersection region of the trapping laser beams.

## 2.3 MOT Apparatus

### 2.3.1 Vacuum Chamber

The equipment to trap atoms in the MOT, in our case, includes an ultra-high-vacuum (UHV) chamber, which is connected to a vacuum pump, two electric field plates, a detection system, and a source of Rb (getter), as shown in Fig. 2-6. The vacuum pump is operated continuously to maintain high vacuum. The trap could be loaded by resistively heating the Rb getter. The chamber and all the components to be contained within are designed to be UHV compatible and can be baked out up to at least 100 °C.

For cooling and trapping optical access must be present through three orthogonal axes. Our chamber consists of two fused silica and four Pyrex windows for this purpose. Fused silica is a very low thermal expansion material and is extremely thermal shock resistant. It also has high homogeneity and good transmission in the ultraviolet and near infrared spectral regions. It is transparent for the trapping lasers (780 nm) and non-trapping laser inputs such as the microwave beam and pulsed Rydberg excitation laser (480 nm). The Pyrex windows are also transparent for the trapping lasers and easily withstand a bake out of up to 150 °C.

There is another Pyrex viewport at the bottom of the chamber, along a fourth axis, to provide additional optical access for trap imaging and also two extra view ports for future modifications.

Electrical feed throughs are provided for the detection system, electric field plates connections and Rb getter containers. The Rb getter containers are mounted on a conflat flange by feed throughs. The microchannel plate detector (MCP) and its electrical feed throughs are premounted on a UHV compatible flange. Our MCP are UHV compatible and can be baked to 300 °C.

Figure 2-6 shows a drawing of the vacuum chamber. One port of the ten ports of the octagonal UHV chamber is connected to a four way cross port which provides us with extra ports. One of the ports is connected to a UHV valve for rough pumping the system, another one is connected to a clean UHV pump, and the third port is connected to a conflat mounted ionization gauge. The ionization gauge provides a second measurement of the pressure, the other one is the magnitude of the ion pump current.

### 2.3.2 Vacuum Pumps

Since we have a small vacuum chamber we use Sputter-ion pump to obtain UHV. We use a Duniway triode sputter-ion pump (RVA-20-TR/M) with a pumping speed of 20 l/s, this pump withstands a bake out up to 200 °C [26]. The ion pump has an array of cylindrical anode cells which are placed between parallel cathode plates constructed of strips of Titanium. The electrodes are charged with a 5 kV dc power supply with a negative voltage polarity. A magnet with a field of few kG surrounds the body of the pump.

All of the pumping systems must be free of oil to prevent organic compounds from back streaming into the chamber. A clean roughing pump is needed to assure that the pump reaches a pressure low enough for sputter-ion pump to start, a pressure below 10 millitorr indicates adequate roughing pump performance. A variety of rough vacuum pumps are available, including rotary mechanical pumps, turbo molecular pumps and sorption pump. The cleanest roughing pump technology is the sorption pump which we used for rough pumping the chamber. The sorption pump uses ultra-high surface area material. Such a molecular sieve, which are chilled to liquid nitrogen temperature (77 K), absorbs most gases at a temperature dependent rate. Water vapor, oxygen, nitrogen, argon and most organic vapors are pumped by our sorption pump except $H_2$, He, and Ne. This pump reduces the pressure to a few millitorr.

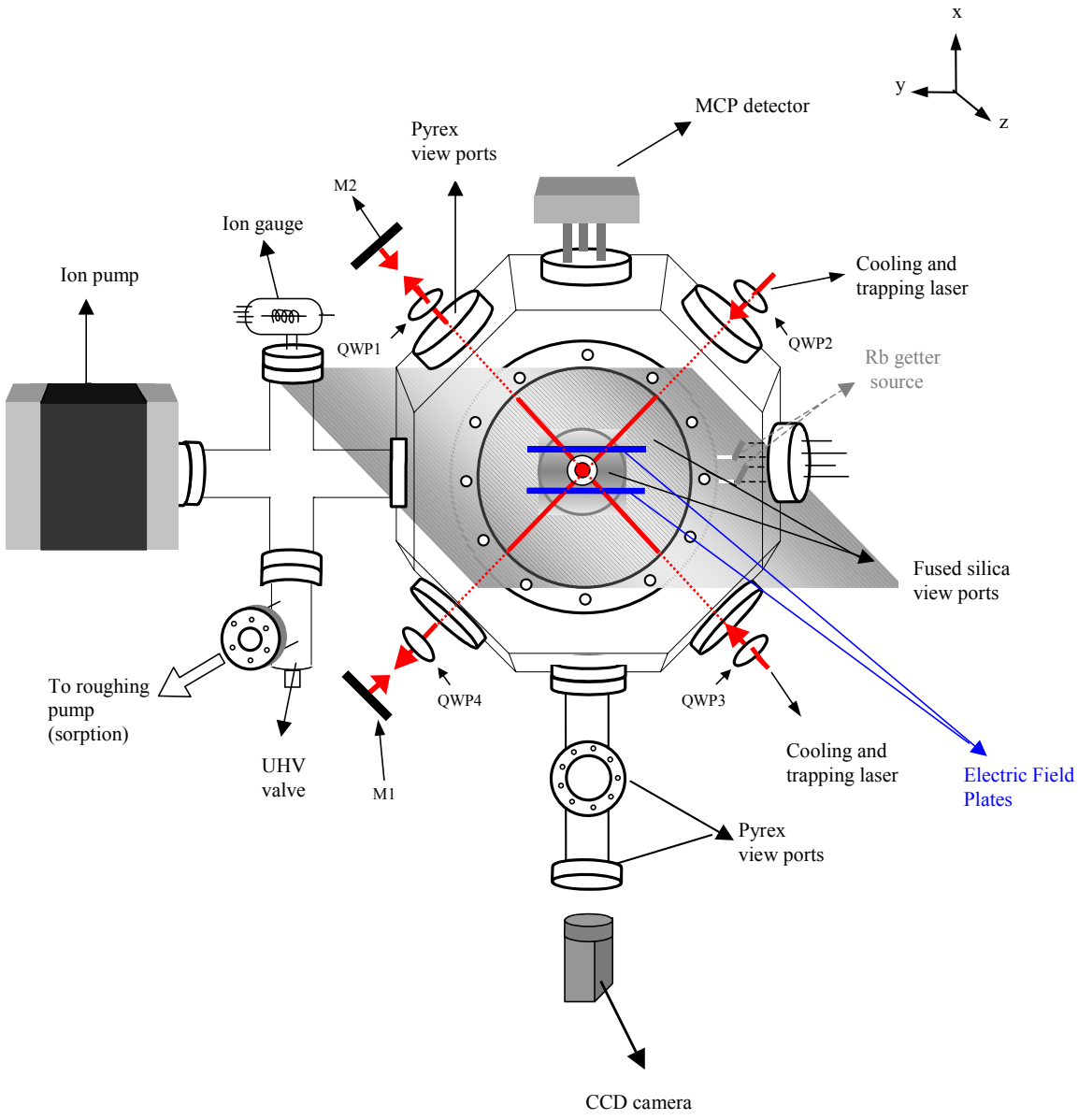


Figure 2-6: Schematic drawing of the vacuum chamber, valves, Rb source, ion pump, MCP detector and CCD camera (not to scale). Quarter wave plates are labelled QWP and retro reflecting mirrors are labelled M. The third trapping beam, perpendicular to the page, is shown by a dot at the center of the chamber.

### 2.3.3 Chamber Cleaning Process

The most important thing to obtain UHV pressures is to make sure all of the vacuum components are clean. The cleaning process for the parts which were machined was,

1. Washing the parts with a liquid detergent then rinsing with hot distilled water, acetone, and methanol. The parts received from the factory should be checked for any stains or small particles. If there are particles on the surfaces, they should be removed using a clean oil-free compressed air. The compressed air capsule should not be tilted more than 40 ° otherwise, it leaves some residual on the components. The rest of cleaning procedure is the same for both machined parts and the ones received from factory.

2. The submersible parts (no valves) were placed in an ultrasonic cleaner with strong degreaser such as trichloroethylene for 1/2 hour. The long cleaning time allows the degreaser to remove residual oil from the machining. After the ultrasonic bath the parts are rinsed with methanol.

3. The parts are baked in air for 2 hours at 130 °C to drive off any residual material still on the parts. Once the parts have cooled they are wrapped in oil-free aluminum foil until assembly.

All knife edges and copper gaskets are wiped with ultra-pure methanol before installation to remove any factory residue. The above procedure should be done wearing powder-free latex gloves to avoid contamination of the vacuum components.

Silvered bolts are used to attach the flanges to the chamber, to reduce the possibility of the bolts seizing during bake out.

Now the entire vacuum system can be assembled. The system is initially pumped out by the sorption pump and checked for leaks. After making sure that the vacuum chamber pressure is low enough for sputter-ion pump to start (below 10 millitorr), the UHV valve is closed and the ion pump is started. The system is pumped on overnight before the bake out is started.

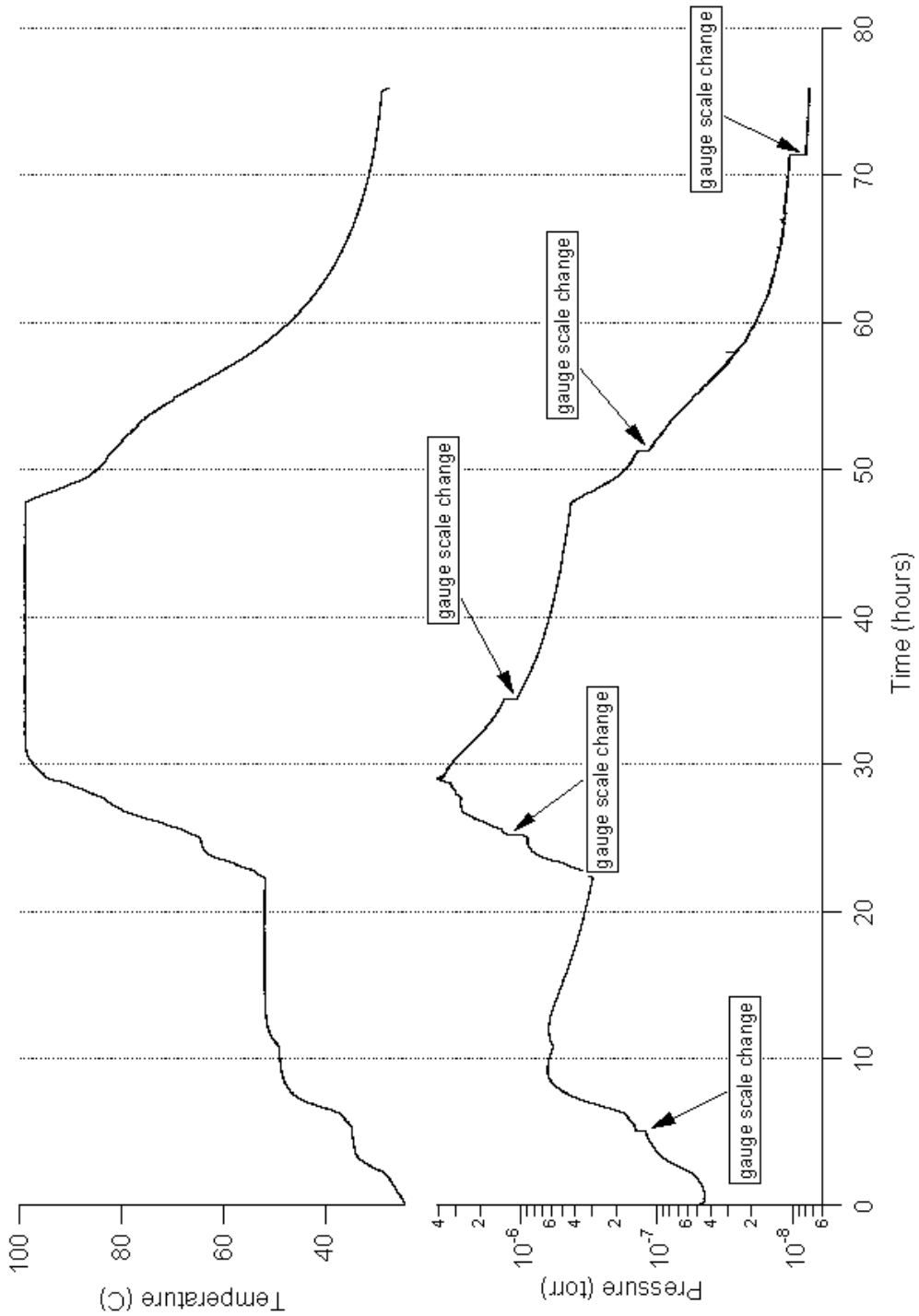


Figure 2-7: The temperature of the vacuum chamber and the ionization gauge pressure during the bake out.

### 2.3.4 Chamber Bake Out

The vacuum system must be baked at high temperatures under vacuum to remove contaminants and obtain UHV pressures. The entire bake out procedure took approximately 75 hours.

After assembly and initial pump down of the chamber, it is placed in an oven. Three thermocouples are placed in the oven at critical places. The entire system including the ion pump and the magnets (coils) are baked. Figure 2-7 shows the temperature and the ionization gauge pressure reading during the bake out. The system is slowly brought up to the final temperature over ∼30 hours. Throughout the warming up process, thermocouple and pressure readings are recorded using a Labview program. Once the temperature of the system reached 100 °C, the system was baked for ∼ 20 hours at the same temperature with the ion pump on. The system was cooled down slowly over ∼ 25 hours. At this point the ion pump indicated a pressure of $2.5 \times 10^{-9}$ torr .

### 2.3.5 Anti-Helmholtz Coils (AHC)

As discussed briefly at the beginning of this chapter, in order to operate the MOT a magnetic field is required which has a single zero field center at the intersection of the trapping laser beams. The magnitude of the magnetic field should increase in all directions from the zero field point. An anti-helmholtz coil, which is a coaxial pair of coils (quadrupole) carrying opposite currents, produces such a field.

If the separation of the coils is $2A$ and they have $2R$ diameter, the transverse, $B_z$, and axial, $B_\rho$, magnetic field components can be expanded as [27],

$$B_z = \sum_n b_n B_{zn} = b_1 z + b_3(z^3 - \frac{3z\rho^2}{2}) + ... \tag{2.1}$$

$$B_\rho = \sum_n b_n B_{\rho n} = b_1(-\frac{\rho}{2}) + b_3(\frac{-3\rho z^2}{2} + \frac{3\rho^2 z}{8}) + ... \tag{2.2}$$

where $z$ is along the axis of the coils lying in the $z = \pm A$ plane and,

$$b_1 = \frac{3\mu_0 I A R^2}{(R^2 + A^2)^{5/2}} \tag{2.3}$$

$$b_3 = \frac{5(4A^2 - 3R^2)}{6(A^2 + R^2)^2} \times b1 \tag{2.4}$$

where $\mu_0 = 4\pi \times 10^{-7}\,\mathrm{T\,m\,A^{-1}}$ [27].

In the Eqs. 2.1 and 2.2, the coils are perpendicular to the $z$ axis and centered at $z = \pm A$. In our geometry the field magnitude increases almost linearly in all directions from the coil center because the coefficient $b_3$ is much smaller than $b_1$ and can be neglected. Hence the magnetic field gradients are,

$$\frac{dB}{dz} = b_1 = -2\frac{dB}{d\rho} \tag{2.5}$$

In our case the coils are on the outside of the chamber so the radius of the coils should be large enough not to block the windows for optical access. Water is circulated through the coils to dissipate heat. Each coils consists of 200 turns of 1.5 mm diameter, 15 gauge, copper wire insulated with enamel jacket. This copper wire has a resistance of 3.249 Ω per 1000 ft at 20 °C [28].

The coils have effective radius of 8.9 cm. The coils are separated by $2A = 12.06$ cm. Inserting these values into Eqs. 2.3, and 2.5, the field gradient is,

$$\frac{dB}{dz}(\mathrm{G\,/\,cm}) = 0.0125 \times n \times I \tag{2.6}$$

where $I$ is the current going through a single coil in amperes and $n = 200$ is the number of turns. A typical operating current is 7.5 A, which yields a field gradient in the $z$ direction of 18.75 G / cm. As shown in Eq. 2.5, axially the field gradient is half of the field gradient in the $z$ direction.

### 2.3.6 Compensating Coils

The apparatus also contains three pairs of coils in the Helmholtz configuration which are called compensating coils or nulling coils. These coils have two applications. Due to the earth, there is stray magnetic field at the trapping region. By adjusting the current running through the coils this stray field can be canceled. This is why these coils are called compensating coils or nulling coils. The coils can also move the trap spatially by a distance of a couple of millimeters.

All the nulling coils contain 50 turns of wire. The largest coils are separated by 13.52 cm, the

smaller set of the coils are separated by 11.74 cm and the smallest set of coils are separated by 9.2 cm. Due to the magnetic field induced by the ion pump and the fact that the zero magnetic field induced by the AHC is not exactly at the center of the trap (since the electric field plates were not mounted exactly at the center of the chamber) only one pair of nulling coils seems to have a positive effect on the trap. This pair of coils generate fields along the $z$ axis, shown in Fig. 2-6. They produce a field of 6.37 G with an operating current of 2.7 A.

## 2.4 Structure and Properties of Rubidium

Because Rb has a single electron outside of closed shells, it has an almost hydrogen like structure of energy levels. Naturally occurring Rb is made of two isotopes, $^{85}$Rb ( 72.17% natural abundance) and $^{87}$Rb ( 27.83% natural abundance) with masses of 84.9117 and 86.909 atomic mass units and a melting point of 38.89 °C [29]. The nucleus of $^{85}$Rb has a spin of $I = 5/2$ while the nuclear spin of $^{87}$Rb is $I = 3/2$.

The ground and first excited states of Rb are $5^2S_{1/2}$ and $5^2P_{1/2,3/2}$ respectively. As we can see in Fig. 2-5, the nuclear spin of $^{85}$Rb, $I = 5/2$, causes hyperfine splitting, but all of the transitions shown have wavelengths around 780 nm and can be achieved with an inexpensive diode laser.

The $5P_{3/2}$ state has a natural linewidth of 5.89 MHz and lifetime of 27 nanoseconds [29]. Total spin, $F$, is the coupling of nuclear spin, $I$, to the total electronic spin, $J$. For the ground $5S$ state,$^{85}$Rb has $F = 2$ or 3, and $^{87}$Rb has $F = 1$ or 2. In the excited $5P_{3/2}$ state, $^{85}$Rb has $F = 1, 2, 3$ or 4, and $^{87}$Rb has $F = 0, 1, 2$ or 3. The hyperfine energy splitting, $\Delta_{hfs}$, between these levels are shown in Table 2.1 and Fig. 2-8

The selection rules for hyperfine transitions are [23],

$\Delta J = 0, \pm 1$

$\Delta F = 0, \pm 1$, not $F = 0 \rightarrow F = 0$

These selection rules determine the allowed hyperfine transitions presented in Fig. 2-8.

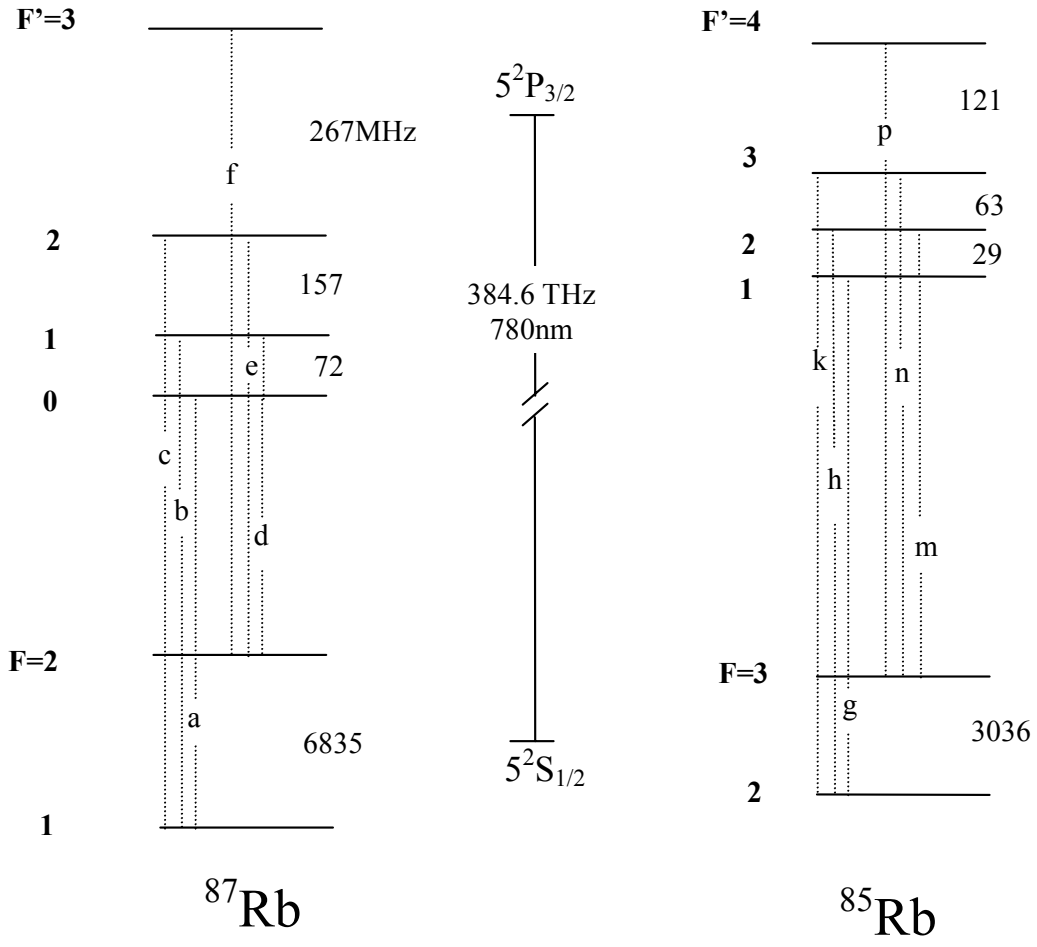


Figure 2-8: Hyperfine splittings (not to scale) of the allowed hyperfine transitions ($\Delta F = 1$) for $^{85}$Rb and $^{87}$Rb. Energy splittings are in MHz. The diagram of the overall transition shown at the center is not linearly scaled. The labels on the lines correspond to the labels in Fig. 2-10 [30].

| Electronic state | Isotope | I | J | F | $\Delta_{hfs}$(MHz) |
|---|---|---|---|---|---|
| $5S_{1/2}$ | $^{85}$Rb | 5/2 | 1/2 | 2,3 | 3036 |
| $5S_{1/2}$ | $^{87}$Rb | 3/2 | 1/2 | 1,2 | 6835 |
| $5P_{3/2}$ | $^{85}$Rb | 5/2 | 3/2 | 1,2,3,4 | 29,63,121 |
| $5P_{3/2}$ | $^{87}$Rb | 3/2 | 3/2 | 0,1,2,3 | 72,157,267 |

Table 2.1: Nuclear angular momenta, I, and hyperfine intervals for the ground and first excited states, J=3/2, of both naturally occuring isotopes of Rubidium [30].

## 2.5 Diode Laser

### 2.5.1 External Cavity Diode Laser (ECDL)

Two different laser frequencies are required for the MOT. External cavity diode lasers (ECDL) are employed for this purpose.

Figure 2-9 shows the ECDL used in the present experiments. This laser was built ([31], [32]) based on the ECDL design of K. B. MacAdam *et al.* [16]. A useful description of ECDL can be found in Refs. [16], [33], and [34]. The output beam reflects off the grating and the first order beam diffracts back into the laser diode. The optical feedback from the grating narrows the laser line width to $< 1\,\mathrm{MHz}$. The grating can be tuned by two adjustment knobs, connected to the grating mount, vertically and horizontally. For the fine tuning of the grating a piezoelectric transducer (PZT stack) is used. A Lexan shield covers the entire set-up to protect it against dust, noise and temperature drifts of the surrounding air.

The semiconductor laser diode used in this experiment is the Sanyo DL7140-201, which produces 70 mW of power at 780 nm.

### 2.5.2 Frequency Control and Stabilization

Both trapping and pumping lasers are locked to atomic transitions in $^{85}$Rb using the dichroic atomic-vapor laser lock (DAVLL) technique [17]. Saturated absorption spectroscopy (SAS) [35] was used to identify the desired atomic transitions and be able to lock the laser at the right frequency. Since these type of frequency stabilizations are standard, they will not be described here in detail.

The basic idea of SAS is to produce sub-Doppler spectral lines. Figure 2-10 shows the SAS and DAVLL spectrum of hyperfine structure of $^{85}$Rb. The labels on the lines correspond to

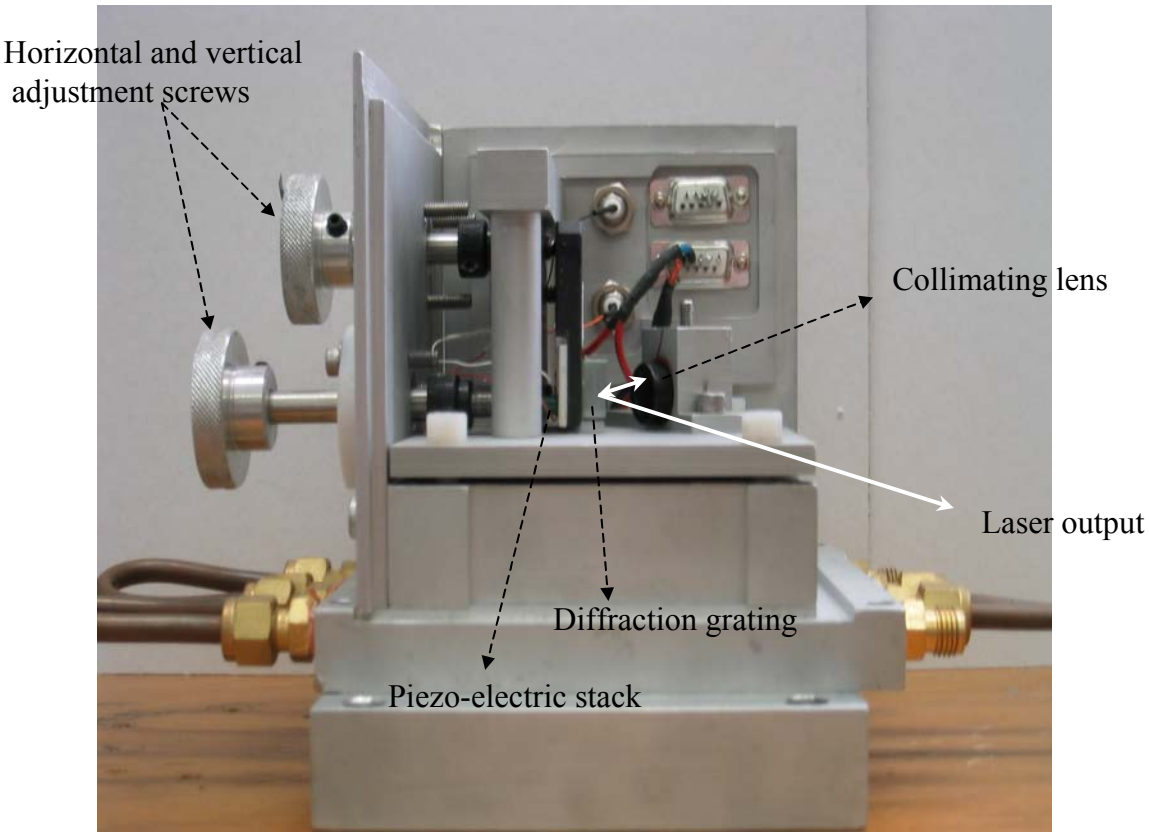


Figure 2-9: ECDL used in the present experiment. It consists of a laser diode, a collimating lens and a diffraction grating [31], [32].

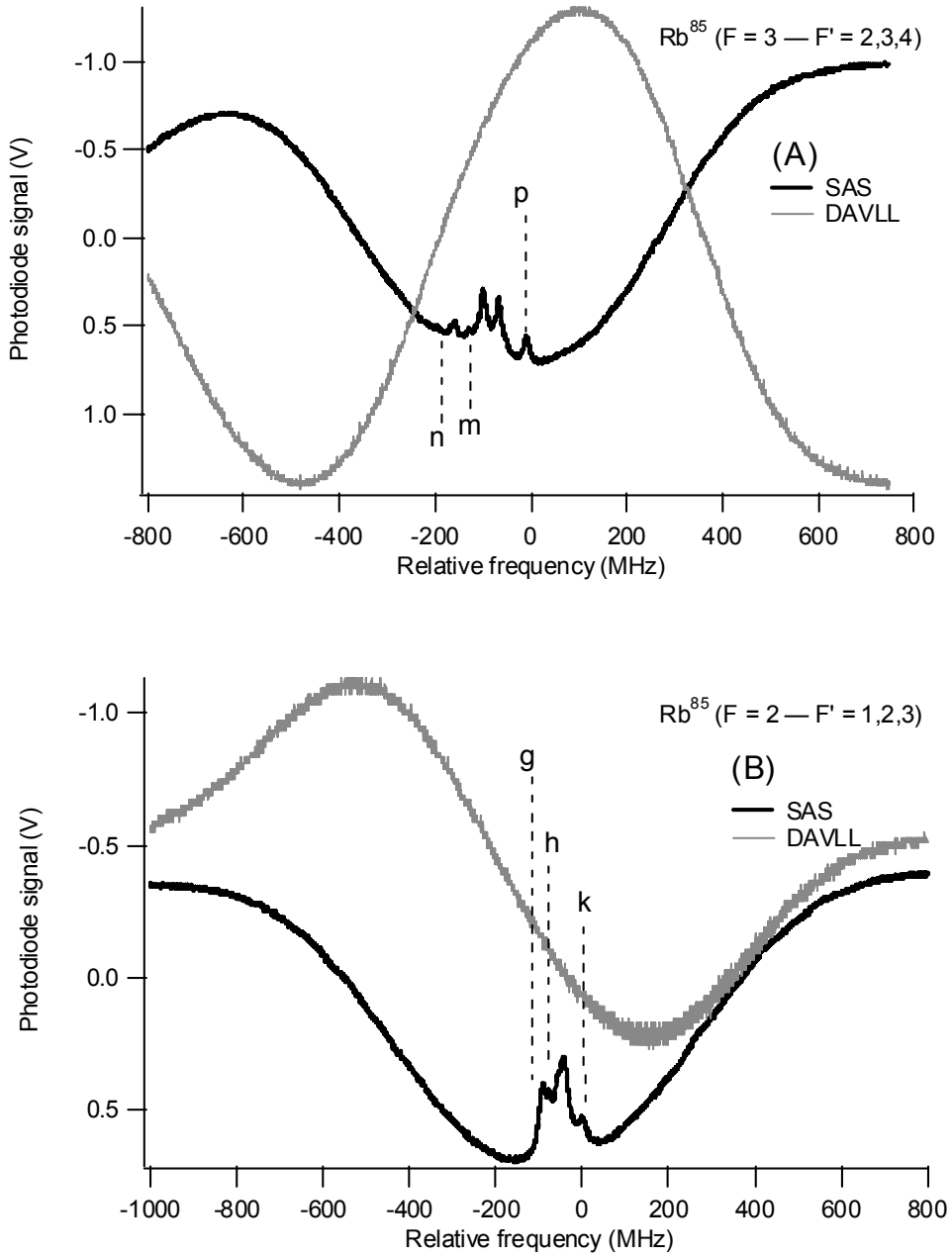


Figure 2-10: SAS and DAVLL spectra of $^{85}$Rb $F = 2$ to $F' = 1, 2, 3$ (for repumping) and $F = 3$ to $F' = 2, 3, 4$ (for trapping). The labels on the lines correspond to the labels in Fig. 2-8. The widths and relative heights of the peaks are affected by beam alignment and intensity.

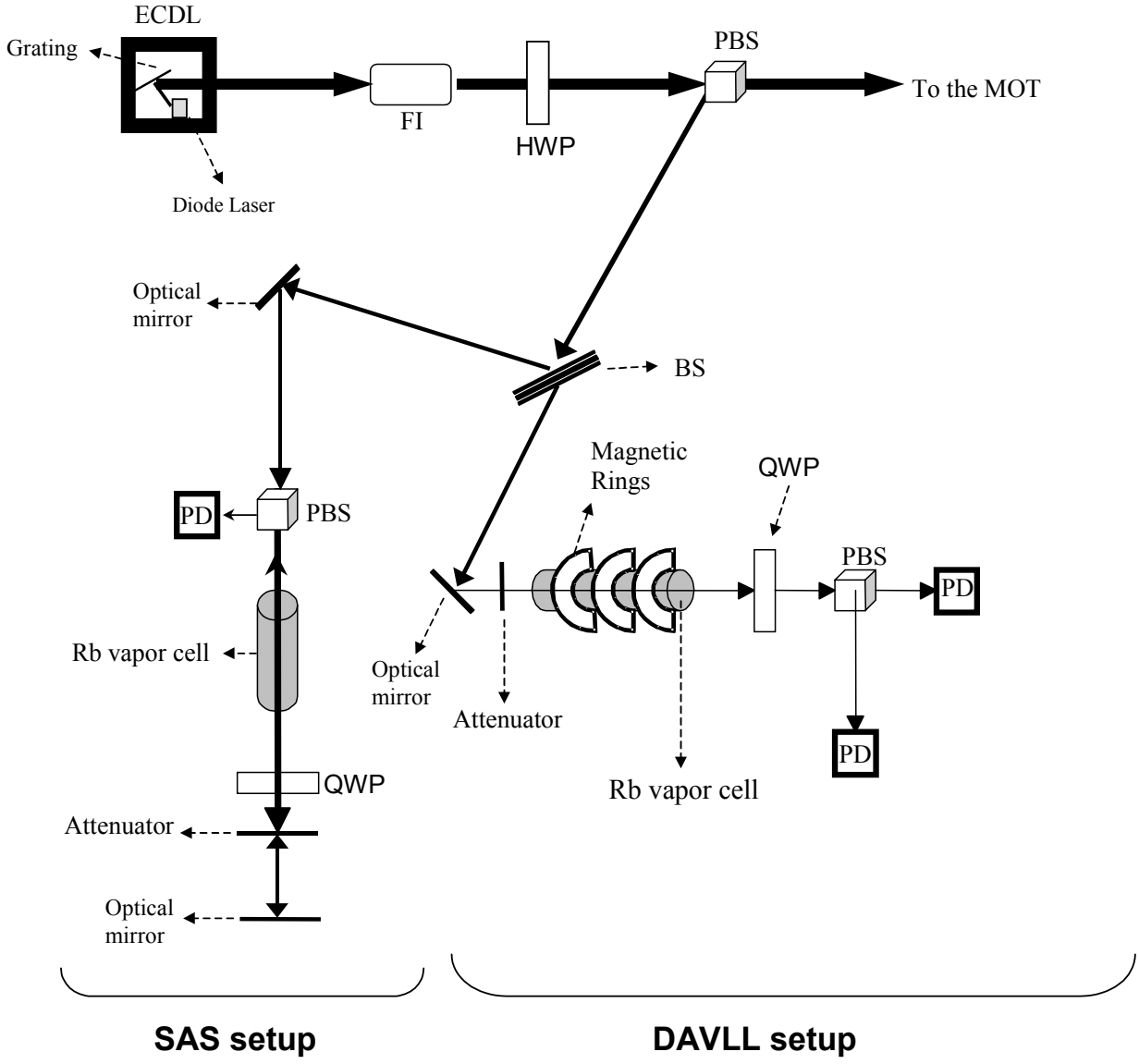


Figure 2-11: Optical layout for the SAS and the DAVLL system. The output beam from the ECDL passes through a beam splitter and a small amount of power is split off to be used for locking and the rest is sent to the MOT. Quarter wave plates, half wave plates, photodiodes, and polarizing beam splitters are labelled QWP, HWP, PD, and PBS respectively. The Faraday isolator is labelled FI and the beam splitters are labelled BS.

the labels in Fig. 2-8. The trapping light is red detuned by several natural linewidths from the $5^2S_{1/2}(F = 3) \longrightarrow 5^2P_{3/2}(F' = 4)$ cooling transition (label p in Fig. 2-10). The repump laser is locked directly to the $5^2S_{1/2}(F = 2) \longrightarrow 5^2P_{3/2}(F' = 3)$ transition (label k in Fig. 2-10).

Each laser can be locked to the peak or the side of an atomic transition. However, the disadvantage of both peak and side locking is the small capture range, which prevents them from recovering from perturbations (such as, mechanical fluctuations in beam alignments and fluctuation of light intensity) that cause drift in the laser frequency.

In order to overcome the problems associated with the SAS technique, the DAVLL system is used [31]. This method employs a weak magnetic field to generate Zeeman splitting of Rb transitions allowing the differential absorption of different circular polarization to be observed. The resulting profile is anti-symmetric and has a sharp slope around the central frequency. This steep slope makes the DAVLL signal less sensitive to noise, and makes it easy to integrate into an electrical feedback circuit that will bring the laser frequency back to the central frequency. Compared to SAS, the DAVLL signal maintains the same slope over a much larger frequency range which translates to larger frequency recapture range. On the other hand SAS provides the necessary reference point for obtaining the DAVLL signal. Therefore a combination of DAVLL and SAS is used for locking the laser frequency. The optical layout for SAS and DAVLL is shown in Fig. 2-11.

## 2.6 MOT Performance

Fluorescence diverging from the collection of trapped atoms over a small solid angle is reflected by a mirror towards a beam splitter. The mirror is installed underneath the trap. The beam splitter splits the light into two beams. One beam is directed towards a CCD camera. The other beam is detected by a non-imaging trap intensity detector [36]. The amplified output of the detector is monitored on an oscilloscope.

The number of atoms in the trap, $n_a$, depends on the trapping laser intensity, amount of Rb released into the trap (which is dictated by Rb getter current) and the current running through the AHC. Using the non-imaging trap intensity detector, at a Rb getter current of $I_g = 10.5\,\mathrm{A}$, and AHC's current of $I_{AHC} = 7.2\,\mathrm{A}$, the amplified trap signal was $2.5 \times 10^{-3}\,\mathrm{V}$,

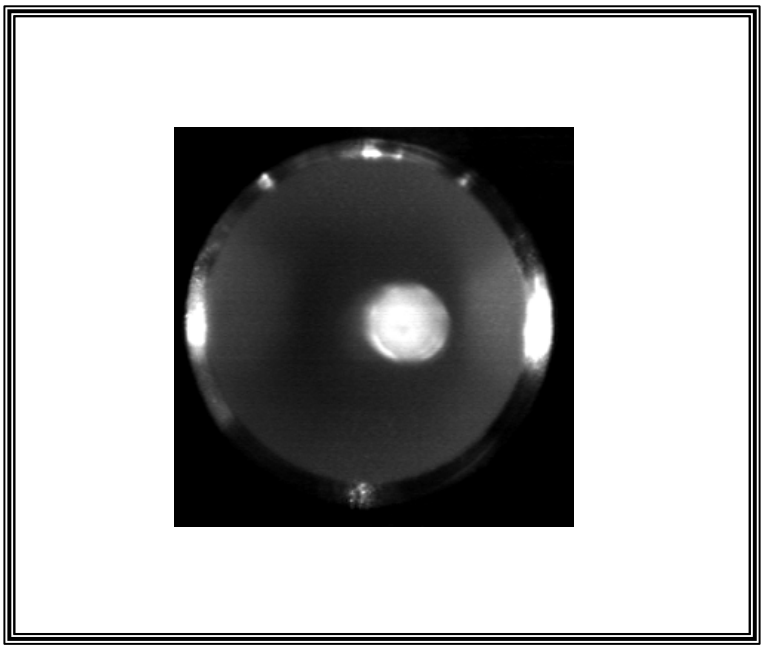

Figure 2-12: CCD snapshot of our MOT.

which corresponds to $5\times10^{-10}$ W of the light power. The solid angle over which light is gathered is limited by the geometry of the mirror. Considering this limit and other accountable losses such as the beam splitter, the partial trap light power read was calculated to be equivalent to 0.0157% of the total trap light power. Therefore the total trap light power was $P_{tt} = 3.19\times10^{-6}$ W. The total number of atoms in the trap, $n_a$, was found to be $2.089 \times 10^6$ atoms, using the following equation [37],

$$P_{tt} = n_a n_p h \frac{c}{\lambda} \tag{2.7}$$

where $h = 6.626 \times 10^{-34}$(J s) is the Planck's constant, $c$ is the speed of light, $n_p = 6 \times 10^6 \frac{(photon/sec)}{atom}$ [37] is the number of photons emitted from a Rb atom per second, and $\lambda = 780 \times 10^{-9}$ m is the wavelength of the trapping light.

Figure 2-12 is a snapshot from a CCD camera showing the cloud of cold trapped atoms in the MOT. The bright circle at the middle of the image is the cloud of atoms and the larger ring around the cloud is the 1/4 inch hole on the lower electric field plate.

## 2.7 Dye Laser

### 2.7.1 Modeless Dye Laser

The ground state of $^{85}$Rb, $5s_{1/2} \rightarrow 5p_{3/2}$, transition is driven by the cw diode cooling and trapping lasers. Transitions from the $5p_{3/2}$ to the $47s_{1/2}$ Rydberg state ($20817.37\,\mathrm{cm}^{-1} = 480.37\,\mathrm{nm}$ [38]) are driven with a pulsed dye laser. The dye laser is pumped by a frequency-tripled Nd:YAG laser. The YAG laser is Q-switched to produce 8 ns long pulse at a 10 Hz repetition rate.

The dye laser used to excite the Rydberg states is a modeless tunable dye laser, first demonstrated by P. Ewart (1985) [19]. In this design, light from the YAG laser is split by a multi-faceted prism into four beams. A cylindrical lens focuses the diverging beams into the dye cell to excite dye molecules flowing through a dye cell making four pumped regions.

Figure 2-13 shows the basic geometry of the modeless dye laser. The multiple pumped regions of the single dye cell are used as the amplifiers, and the frequency selective elements are illuminated strips on a single diffraction grating. All of the frequency selective elements are tuned simultaneously by changing the angle of the tuning reflector with respect to the grating. Hence wavelength adjustment is performed in the same way as for a conventional

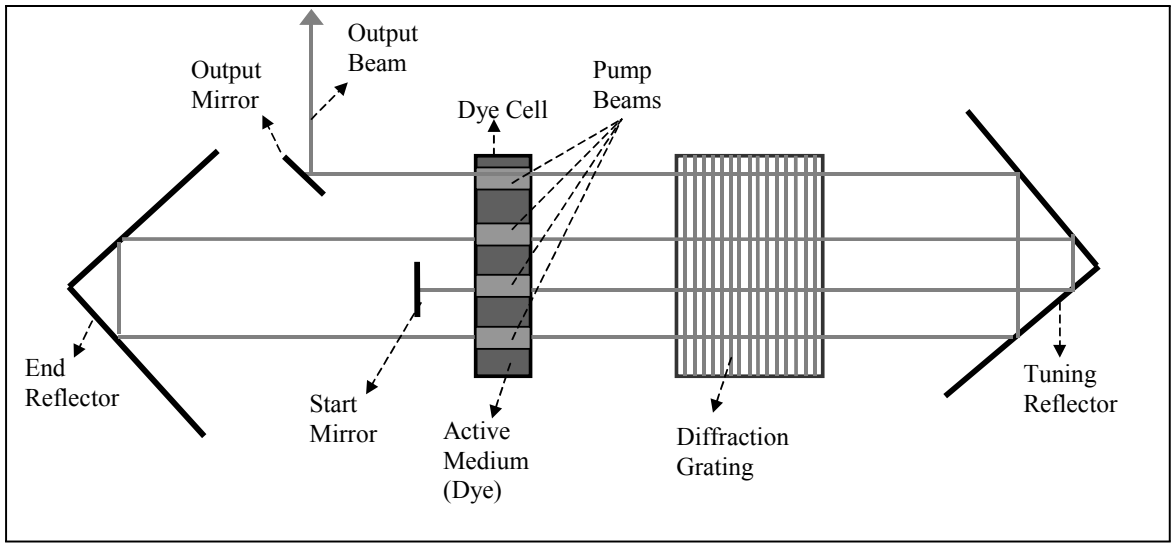


Figure 2-13: Basic geometry of a modeless dye laser (after Ref. [39]).

grazing-incidence dye laser [40].

This type of dye laser was constructed in the lab [39] after Ewart's design [19]. This laser uses perpendicular flat mirrors as tuning and end reflectors, to reduce back reflection and cost compared to Ewart's design. The gain medium is Coumarin 480 dye which is an appropriate choice for the desired operational wavelength of $\sim 480\,\mathrm{nm}$. The wavelength selective element is a 3600 lines/mm holographic diffraction grating. The tuning reflector is rotated by a stepper motor. The stepper motor is operated by a stepper motor driver (Newport, ESP300) and the driver is controlled by a Labview program which will be discussed in Sec. 2.10.

### 2.7.2 Wavelength Calibration

The dye laser wavelength was calibrated by observation of tabulated transitions of Ne [41], using the Optogalvanic (OG) effect in a hallow-cathode (filled with U and Ne) discharge [42]. The light from the pulsed dye laser induces U and Ne transitions. These transitions can be measured electrically, using the OG effect, in an external circuit. The output signal of this circuit is gated using a boxcar integrator. The output of the boxcar is digitized and recorded as a function of the stepper motor position. The resultant spectrum has peaks which can be assigned to the tabulated Ne transitions.

A small amount of dye laser output (10%) was split off and directed towards a diverging lens ($-16.5\,\mathrm{cm}$ focal length), followed by a fused silica etalon ($1.14\,\mathrm{cm}^{-1}$ Free Spectral Range, 80% reflectivity for $479-490\,\mathrm{nm}$ and $594-603\,\mathrm{nm}$, LightMachinery). This setup created a fringe pattern. A photodiode was placed at the screen of the fringe pattern, approximately $35\,\mathrm{cm}$ from the etalon, and recorded the passing fringes as the wavelength was scanned.

The rest of the dye laser light (90%) passed through one single-pass dye amplifier. The amplifier is a dye cell with flowing dye and is also pumped by the third harmonic of the YAG laser. The third harmonic of the YAG laser is split into two beams to pump the modeless dye laser and the amplifier at the same time. The modeless dye laser is pumped by $3.5\,\mathrm{mJ}$ /pulse, corresponding to an average power of $35\,\mathrm{mW}$ and the amplifier is pumped by $9\,\mathrm{mJ}$ /pulse, corresponding to an average power of $90\,\mathrm{mW}$ at $355\,\mathrm{nm}$.

The same Labview program which collects the OG signal also records the output signal of the photodiode simultaneously as a function of stepper motor position. The etalon frequency

markers were used to study the behavior of the laser light and as constant frequency markers between Ne transitions.

Traces (a) and (b) in Fig. 2-14, show the fringe pattern and the corresponding OG spectrum recorded simultaneously as a function of stepper motor position. The lines in trace (b) can be assigned to Ne transitions using "Tables of spectral lines of neutral and ionized atoms" by A. R. Striganov *et al.* [41].

The assigned OG lines can be used to form a relationship between the stepper motor position and vacuum wavelength. This relationship can be used for any wavelengths in the range enclosed by the calibration points.

Wavelength in vacuum can be converted to wavenumber in $\mathrm{cm}^{-1}$ by,

$$E(\mathrm{cm}^{-1}) = \frac{10^7}{\lambda_{vac}(\mathrm{nm})} \tag{2.8}$$

where $\lambda_{vac} = \lambda_{air} \times 1.0003$.

In Sec 3.1, it will be explained how to identify the highly excited Rydberg states of $^{85}$Rb using the calibrated dye laser energy ($\mathrm{cm}^{-1}$).

## 2.8 Microwave Components

To generate microwaves, a microwave signal generator (Agilent-E8254) is used. This source can generate frequencies from 250 kHz to 40 GHz. The cw output of the synthesizer is formed into pulses using a digital delay generator (SRS-DG535).

To direct the microwaves from the synthesizer to the trap region, the output of the synthesizer passes through the following components:

1. A 24" long coaxial cable with 1.25 dB/ ft insertion loss. The cable has connectors at each end. Each of the connectors has 0.25 dB insertion loss. The total insertion loss of the cable with its connectors is 3 dB.

2. An aluminium WR-28 waveguide to coax adapter with 0.3 dB insertion loss.

3. Straight 4" long WR-28 waveguide with $\sim 0.9$ dB insertion loss.

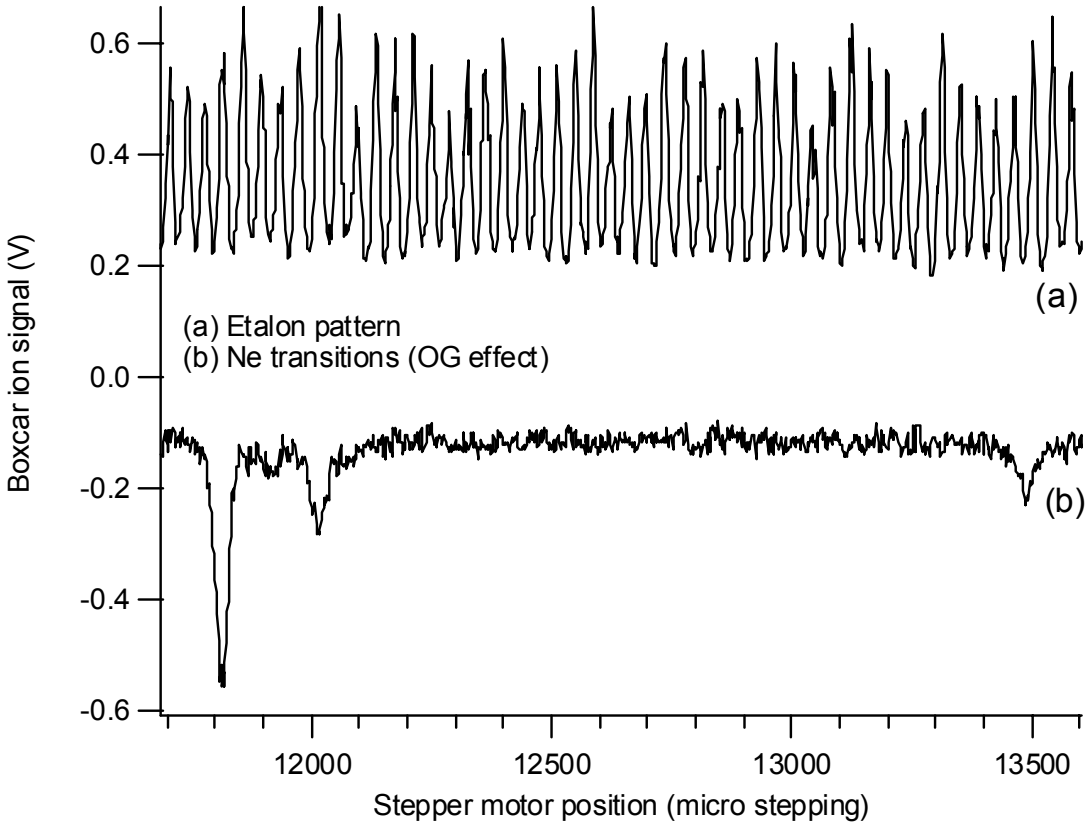


Figure 2-14: The spectrum of typical Etalon pattern, trace(a), and OG, trace(b), as a function of the stepper motor position.

4. Standard 20 dB gain horn antenna, to launch the microwaves through the largest window of the vacuum chamber towards the trap region.

The operational frequency range for the above microwave components is $26.5 - 40\,\mathrm{GHz}$.

## 2.9 Detection System

The low ionization threshold of the Rydberg atoms makes them quite susceptible to dc electric fields. One of the most sensitive methods for detection of Rydberg atoms is the selective field ionization technique, which will be explained in the following Section. The instruments used to generate the electric field and detect the ion signals are also discussed in Secs. 2.9.2 and 2.9.3.

### 2.9.1 Selective Field Ionization (SFI)

The ionization threshold of Rydberg atoms scales as $n^{-4}$, where $n$ is the principal quantum number. If the energy shift of a Rydberg state in the presence of an electric field is ignored,

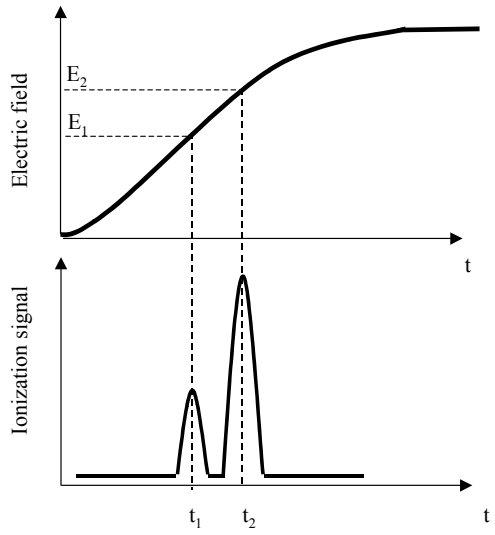


Figure 2-15: Scheme of SFI detection of Rydberg states. The top graph shows a time resolved (slowly rising) electric field $E$, started after the Rydberg state excitation by laser light. At times $t_1$ and $t_2$, the $E$ field reaches the ionization thresholds $E_1$ and $E_2$ for the Rydberg states $n_1$ and $n_2$ . The bottom graph shows, corresponding ionization signals of the levels $n_1$ and $n_2$ (after Ref. [43]).

then the classical field for ionization in terms of $n$ is [1],

$$E = \frac{1}{16n^4}. \tag{2.9}$$

As soon as a field on this order is applied, the Rydberg atoms are ionized and the resultant ions and electrons can be accelerated and detected by a microchannel plate detector (see Sec. 2.9.3). The binding energy of the Rydberg states depends on the principal quantum number, $n$, angular momentum, $l$, and also varies between different levels with different sublevels, $m_l$. Since the ionization threshold depends on the binding energy, the excited states can be detected selectively.

Electric field ionization uses either a fast rising electric pulse (square pulse) or a slowly rising (time resolved) pulse. The fast rising pulse is used to detect different Rydberg states as the laser frequency is being scanned. On the other hand, in order to detect the initial and final states of the microwave transition $47s_{1/2} \rightarrow 47p_{1/2}$ simultaneously, a slowly rising pulse is used. The slowly rising pulse makes it possible to detect and resolve Rydberg states that have different binding energies.

Figure 2-15 shows the scheme for SFI of the Rydberg states $n_1$ and $n_2$ using a time varying electric field, $E$. After the atoms are excited to these Rydberg states, an $E$ ramp is applied. The $E$ field reaches the ionization thresholds, $E_1$ and $E_2$ of the Rydberg states $n_1$ and $n_2$ at different times $t_1$ and $t_2$ respectively. Therefore, a time-resolved peak appears for each of the states in the ionization signal (Fig. 2-15, bottom graph).

This detection method of Rydberg states is simple, sensitive and energy selective. In the experiments presented in this thesis, the Rydberg states $47s_{1/2}$, $47p_{1/2}$ and $47p_{3/2}$ can be detected selectively in this way. The ionization potentials of the states $47p_{1/2}$ and $47p_{3/2}$ are very close, thus these two states cannot be distinguished at the same time.

The slowly rising field ionization pulse is initiated $3\mu$s after the Q-switch and has a peak value of $99.8\,\mathrm{V/cm}$. A trigger from the Q-switch is sent to the digital delay generator which sends a trigger pulse to a homemade [44] high voltage (HV) pulse generator which field ionizes the atoms.

The fast rising field ionization pulse is initiated $1\mu$s after the Q-switch of the YAG laser

and has a peak value of $112.5\,\mathrm{V}\,/\,\mathrm{cm}$. A trigger from the Q-switch of the YAG laser is sent to a digital delay generator (SRS - DG535) which sends a trigger pulse to another homemade [45] HV pulse generator which field ionizes the atoms.

### 2.9.2 Electric Field Plates

The Rydberg states are detected via selective field ionization and subsequent collection of ions by a microchannel plate (MCP) detector.

Figure 2-16, shows a pair of stainless steel electric field plates separated by $3.556\,\mathrm{cm}$. Each plate is $3.313 \times 1.75\,\mathrm{in}^2$ in size. These plates have two purposes: to provide the high voltage ionizing field pulse and to provide an offset voltage for stray electric field compensation.

A field ionizing pulse is applied to the region between the plates. This pulsed electric field, ionizes the excited atoms and also serves as an extraction pulse, directing the ions up into the MCP. Figure 2-6, shows how these two plates are mounted inside the vacuum chamber. The field ionization pulse is applied to the bottom plate. The offset voltage is also applied to these plates.

Each plate has two rectangular holes ($0.25 \times 0.375\,\mathrm{in}^2$) to allow passage of the trapping beams. The upper plate has a 1/4 inch circular hole for ion extraction towards the MCP and the lower plate also has a 1/4 inch circular hole to allow imaging of the trap by a CCD camera.

The ionizing voltages are applied to the plate farthest from the detector (bottom plate). The field plate closest to the detector is grounded, to shield the MCP detector from the field ionization pulse (FIP). However, when the offset voltage is required to be applied, this plate is connected to an arbitrary waveform generator, AWG, (Agilent 33250A) in order to generate and control a dc voltage.

### 2.9.3 Microchannel Plate Detector (MCP)

Once the field ionizing and extraction pulse is applied, the ions are drawn up to the microchannel plate (MCP) detector. The ions hit the front plate of a double microchannel plate detector [46]. This MCP consists of two microchannel plates. The wiring of this detector is shown in Fig. 2-17 [47].

A charged particle incident on the surface of the input microchannel plate will free electrons

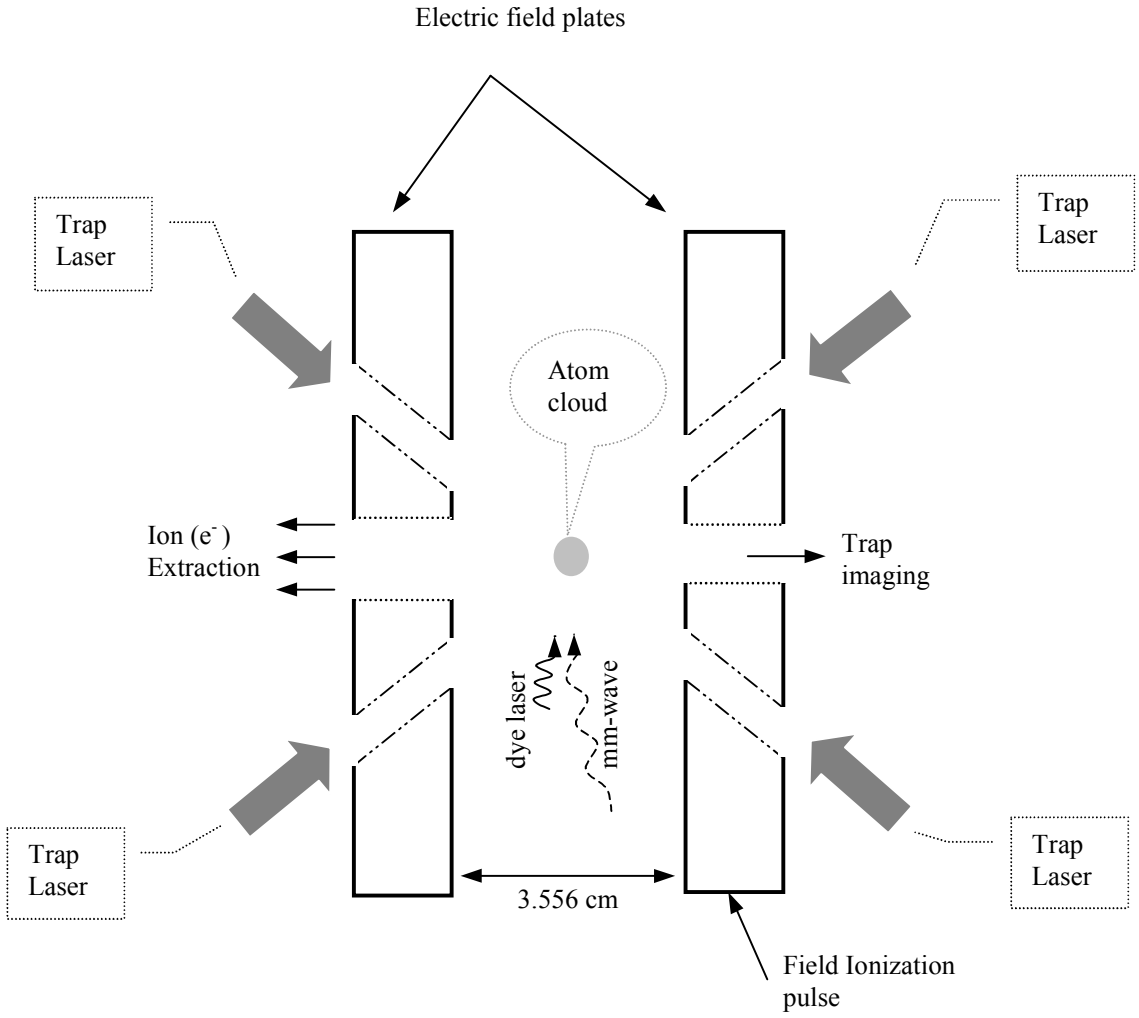


Figure 2-16: Schematic geometry of the electric field plates.

from the channel wall. An electron accelerating potential difference ($\sim -1400\,\mathrm{V}$) is applied across the length of the channel. The initial electron strikes the adjacent wall, freeing several electrons (via secondary emission). These electrons will be accelerated along the channel until they in turn strike the channel surface, giving rise to more electrons. Eventually this process yields a cloud of several thousand electrons which emerge from the rear of the plate. The multiplied electron signal is collected by an anode and generates a voltage across a 50 $\Omega$ resistor, which is then amplified by modular amplifiers (Minicircuit ZF500). The necessary voltage to the MCP is slowly increased by 100V steps until the optimum voltage is reached.

Figure 2-6 shows the place of the MCP installed inside the vacuum chamber. The microchannel plate detector is mounted on a UHV flange and is held a few centimeters above the extraction hole on the upper electric field plates.

## 2.10 Data Collection Technique

LabVIEW was used to collect data in all the experiments. LabVIEW is a visual programming language that is widely used for data collection and automation. The OG spectrum, etalon fringe pattern, Rydberg state ion signal, microwave spectrum, and fluorescence signal of the trapped atoms were all collected using LabVIEW programs.

Figure 2-18 is a snapshot of the main panel of the program. This program is able to sweep the dye laser frequency while the signals of OG, etalon pattern and ion signal are averaged over many laser shots. The outputs and inputs of the program are numbered in this figure and their functions are described below.

**(1) - GPIB address of stepper motor**

The GPIB address of the instrument to be driven by the program, such as stepper motor driver or microwave signal generator.

**(2) - number of scans to acquire**

A 16-channel digitizer (National Instruments) is used to digitize the analogue time-averaged output signals of two boxcar integrators. A subroutine communicates with this digitizer and collects the signals from different channels. The number of laser shots to be averaged is set by this input, (2). For example, in the illustrated program each step is averaged over 20 laser

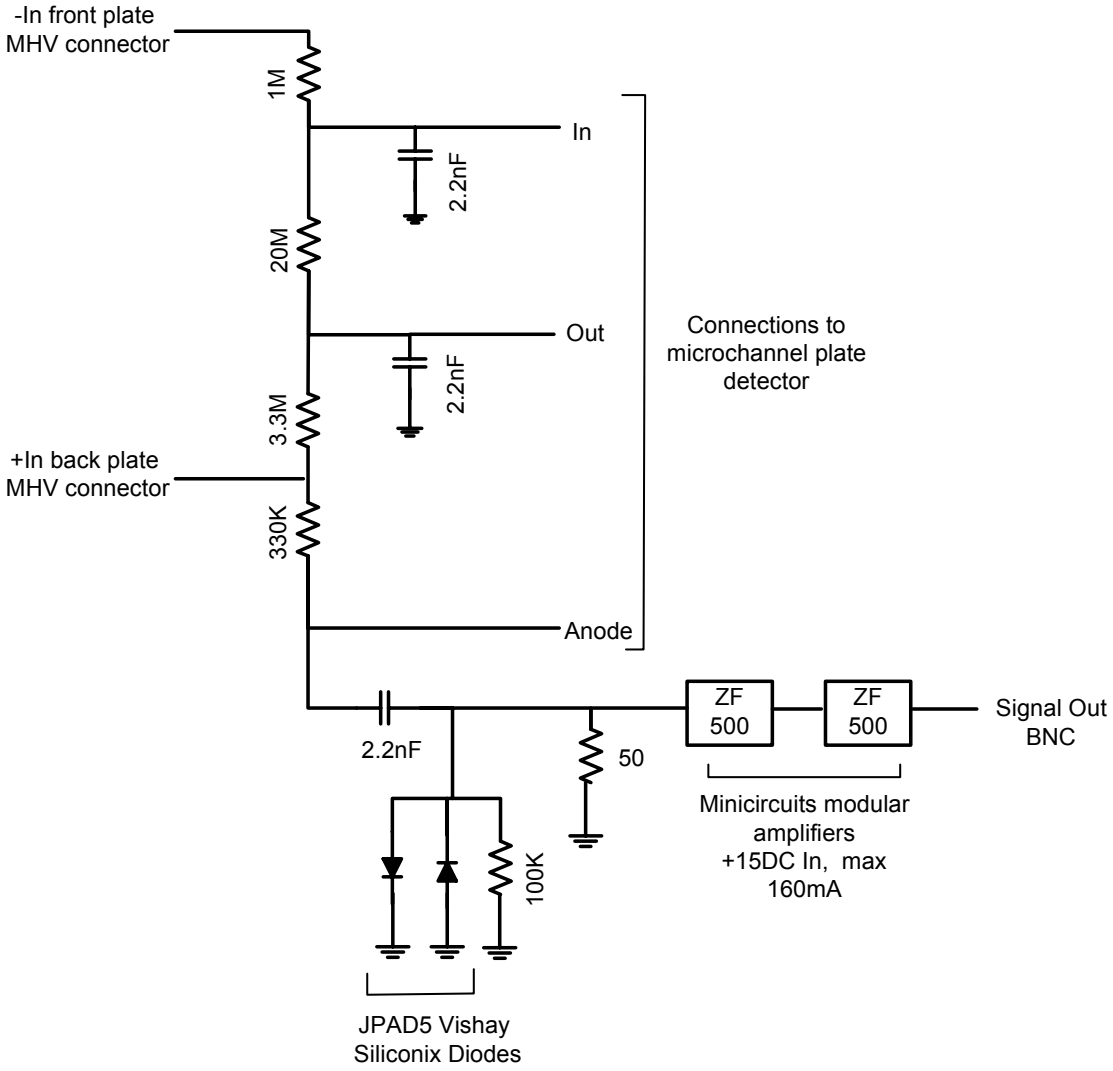


Figure 2-17: Microchannel plate detector wiring diagram, after Ref. [47].

shots.

**(3) - channels**

This part shows the channels are being recorded. The program shown in Fig. 2-7 records and shows the data collected from three different channels of the digitizer as a function of stepper motor position.

**(4, 5) - start & stop position**

The start and stop position of the stepper motor (or start and stop frequency of the microwaves).

**(6) - number of steps/point**

The increment of stepper motor position (or microwave frequency).

**(7) - axis number**

the axis of the stepper motor driver to be controlled.

**(8, 9) - position before move & current position**

Output 8 displays the position of the stepper motor before the program starts moving the position. Output 9 indicates the position of the stepper motor while the program is running.

Finally, graphs number 10, 11, and 12 display the recorded and averaged signals as the program is running.

With slight modifications to the program shown in Fig. 2-7, it is possible to drive the microwave signal generator and sweep the microwave frequency while the signal is averaged over many laser shots. A typical scan of microwave frequency is stepped in increments of 80 kHz, and each step is averaged over 40 laser shots.

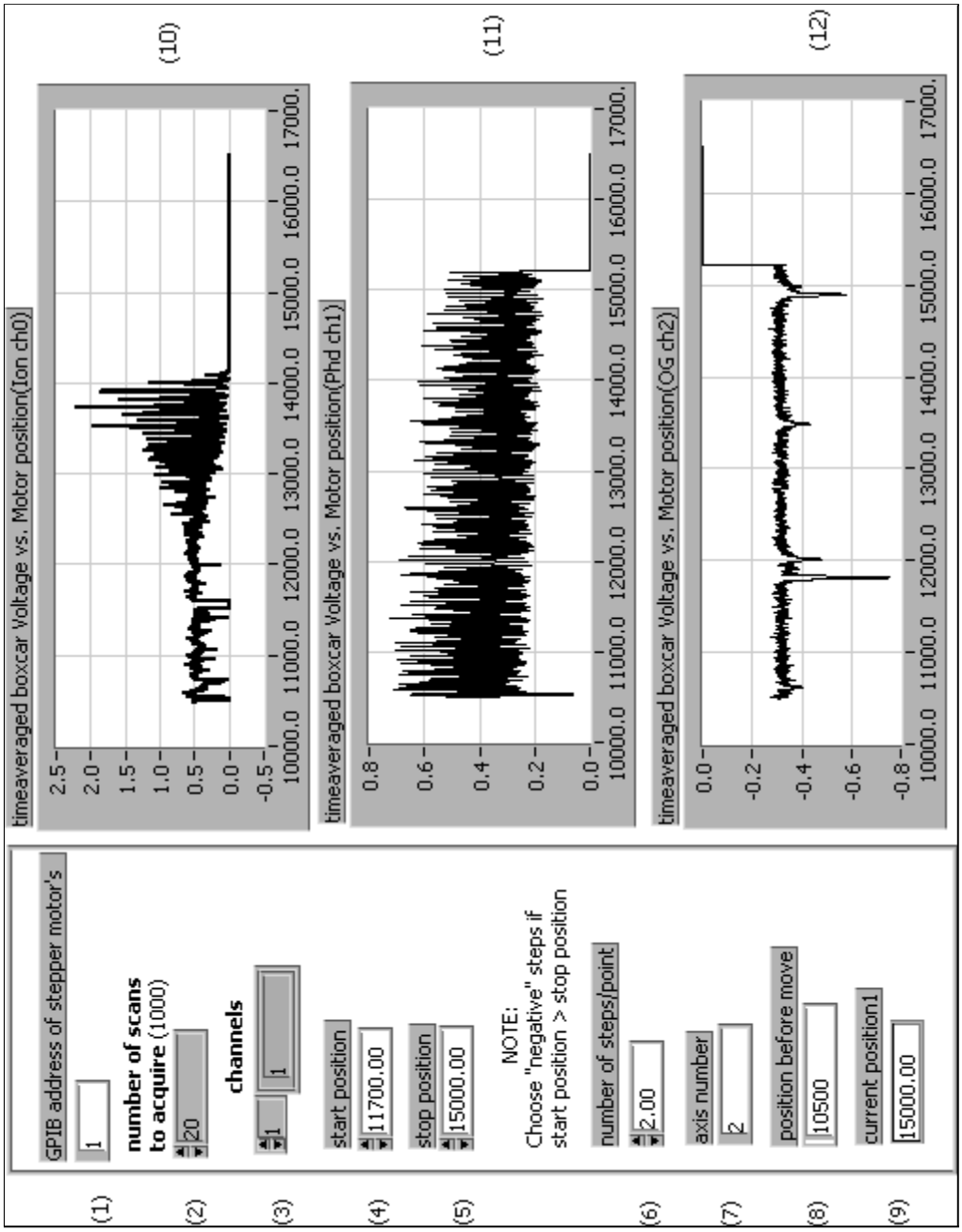


Figure 2-18: Snapshot of panel page of the LabVIEW data collection program. The Rydberg state ion signal, etalon fringe pattern, and OG spectrum are being collected as shown in graphs 10, 11, and 12 respectively. The function of each part (1-12) is explained in the text.

# Chapter 3

# Initial Observations

This chapter begins with a description of the experimental procedure performed to identify the Rydberg states using the calibrated dye laser wavelength (Sec. 3.1). In Sec. 3.2, the effect of the intensity of the microwave field on the linewidth of the microwave transitions ($47s_{1/2} \rightarrow 47p_{3/2}$) is explained and the experimental data are analyzed and interpreted. This effect must be minimized in order to improve the experimental resolution.

## 3.1 Experimental

The modeless dye laser excites trapped atoms in the MOT to Rydberg states. The $47s_{1/2}$ Rydberg state lies $20817.37\,\mathrm{cm}^{-1}$ above the $5p_{3/2}$ state [38], which corresponds to $\lambda_{vac} = 480.37\,\mathrm{nm}$ using Eq. 2.8. In order to excite the atoms to the $47s_{1/2}$ states, the dye laser should be carefully adjusted to this wavelength.

First, the frequency of the dye laser is tuned $\sim 10\,\mathrm{cm}^{-1}$ above the ionization potential (IP) of Rb[1]. Then, the laser frequency is scanned and the fast rising field ionization pulse (FIP), field-ionizes the Rydberg states and the ion signals are detected by the MCP. The detected signals are collected as a function of laser frequency (or energy ($\mathrm{cm}^{-1}$)). Finally, the observed transitions can be identified using the tabulated atomic energy levels of C. E. Moore [38].

To identify the Rydberg states precisely, the dye laser frequency was scanned and the OG spectrum, etalon pattern and the ion signals of the Rydberg states were collected simultaneously

[1]The IP of Rb lies $20874.46\,\mathrm{cm}^{-1}(\lambda_{vac} = 479.0543\,\mathrm{nm})$ above the $5p_{3/2}$ state [38].

using a LabVIEW program. Figure 3-1 shows the spectrum of OG, etalon pattern, and the ion signal of the Rydberg states as a function of the excitation energy relative to the ground state $5s_{1/2}$. Figure 3-2 shows the assigned Rydberg states. To collect the data shown in Fig. 3-2, the ion signal was gated and averaged using a boxcar averager.

After the desired state was identified, the stepper motor, which turns the tuning mirror of the modeless dye laser, was moved back (to $\sim 10\,\mathrm{cm}^{-1}$ above the IP) and scanned to the right transition. In Fig. 3-2, the desired transition, $47s_{1/2}$, is marked by an arrow.

To collect the spectrum in Fig. 3-2, a small amount of dye laser output (10%), was split and directed towards the fused silica etalon to collect the etalon pattern. The rest of the laser light passed through the single-pass dye amplifier. The amplified light was split into two beams by a neutral density filter (ND 0.5) with 31% transmittance. The transmitted beam was sent to the OG hollow cathode lamp and the reflected beam was directed towards the trap to excite the atoms to Rydberg states.

In order to observe the microwave transition $47s_{1/2} \rightarrow 47p_{1/2}$ the following procedure is performed.

The fast rising FIP is switched to the slowly rising (time resolved) FIP. A trigger from the Q-switch of the YAG laser initiates the timing sequence of most of the experiments. The trigger is sent to a digital delay generator (SRS - DG535) which sends a trigger pulse to a high voltage (HV) pulse generator 3 $\mu s$ later, field ionizing the atoms. Figure 3-3 shows traces of the slowly rising FIP signal along with the ion signal of $47s_{1/2}$ and $47p_{1/2}$ detected by the MCP on an oscilloscope. Due to the slow rise time of the FIP and the different field ionization thresholds, different Rydberg states ionize at different times with respect to the onset of the ionization pulse.

A boxcar gate is set to detect the $47p_{1/2}$ state (Fig. 3-4). The Labview program, described in Sec. 2.10, is used to sweep the microwave frequency while the signal is averaged over many laser shots. A typical scan of microwave frequency is stepped in increments of 80 kHz and each step is averaged over 40 shots of the laser. The ion signal is averaged by the boxcar over a 105 ns time-period starting $\sim 10$ $\mu$s after the light pulse (Fig. 3-4).

The delay generator also sends another trigger pulse to the microwave signal generator (Agilent-E8254) to switch off the microwaves right before the onset of the ionizing pulse and

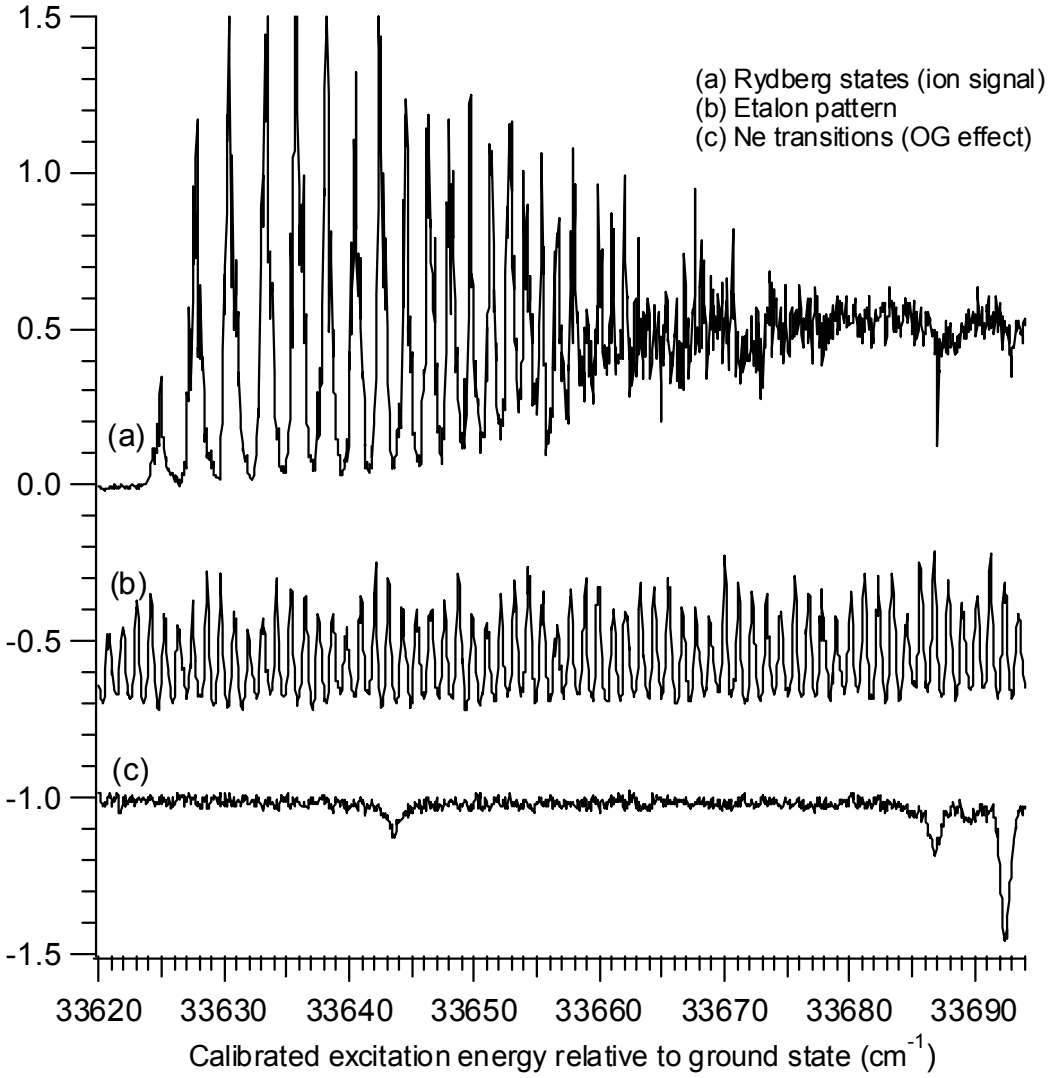


Figure 3-1: The spectrum of the ion signal of the Rydberg states (trace(a)), etalon pattern (trace(b)), and typical OG signal (trace(c)). For the sake of clarity, traces (c) and (b) have vertical offsets $-0.7$ and $-0.9$ respectively.

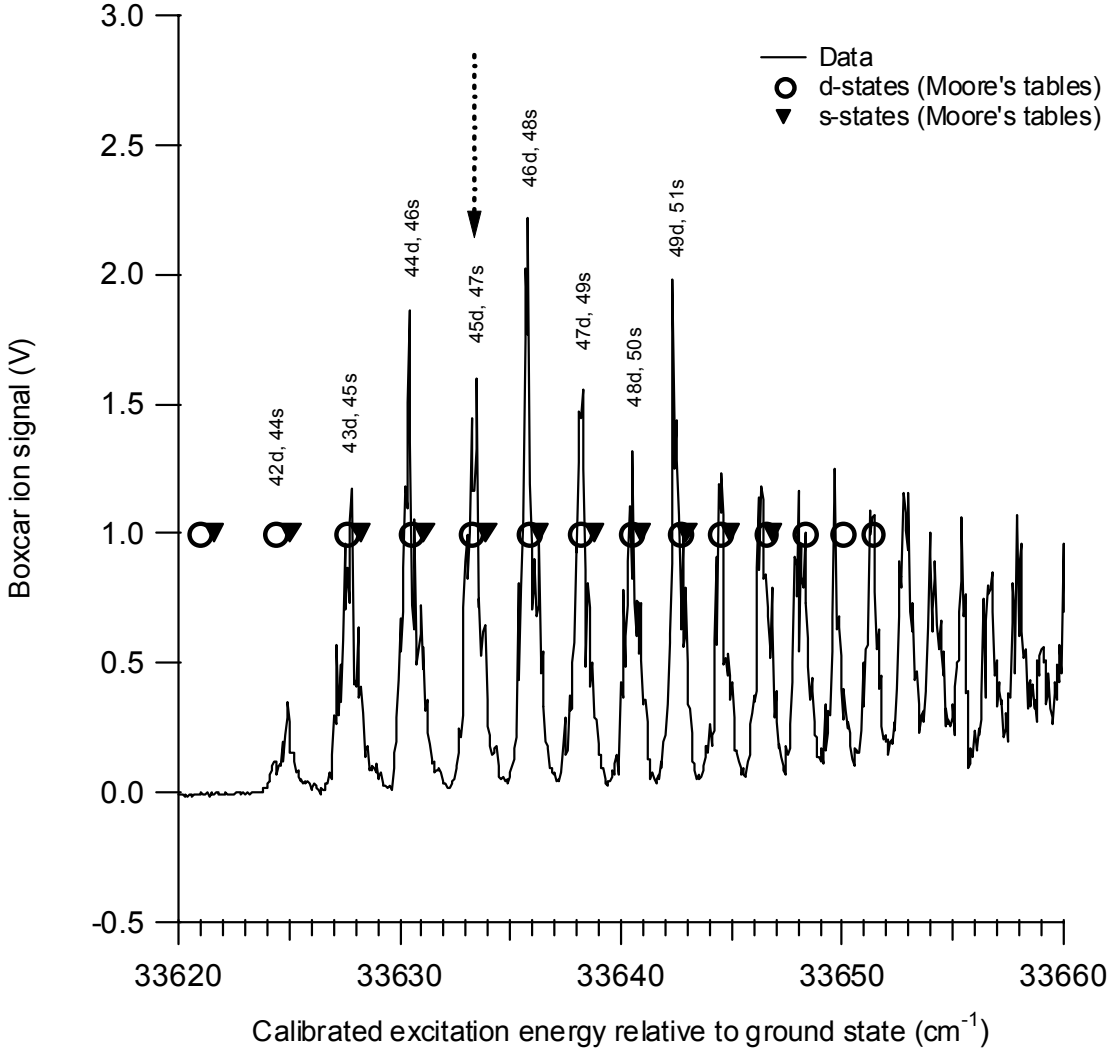


Figure 3-2: The assigned spectrum of the Rydberg states of Rb. The high lying states are unresolved due to the line width of the excitation source (dye laser). The ion signals were collected by pulsing on an electric field (fast rising FIP,112.5 V / cm) shortly after photoexcitation ($1\mu s$).

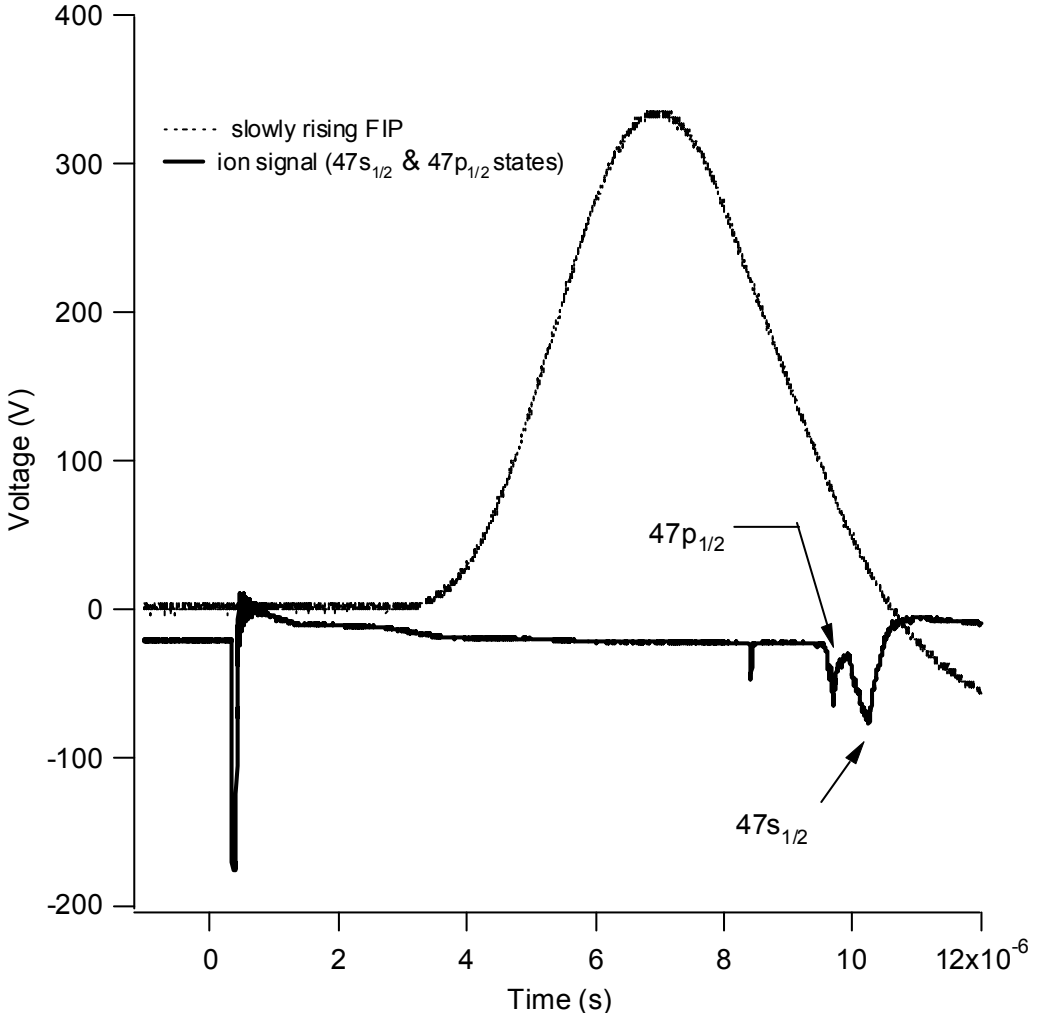


Figure 3-3: Traces of FIP signal and ion signals of $47s_{1/2}$ and $47p_{1/2}$ states observed on an oscilloscope. The ion signals are expected to appear around the peak of the FIP. Since the MCP detector detects the ions after a certain time of flight (TOF), the ion signals appear on the oscilloscope at an slightly later time.

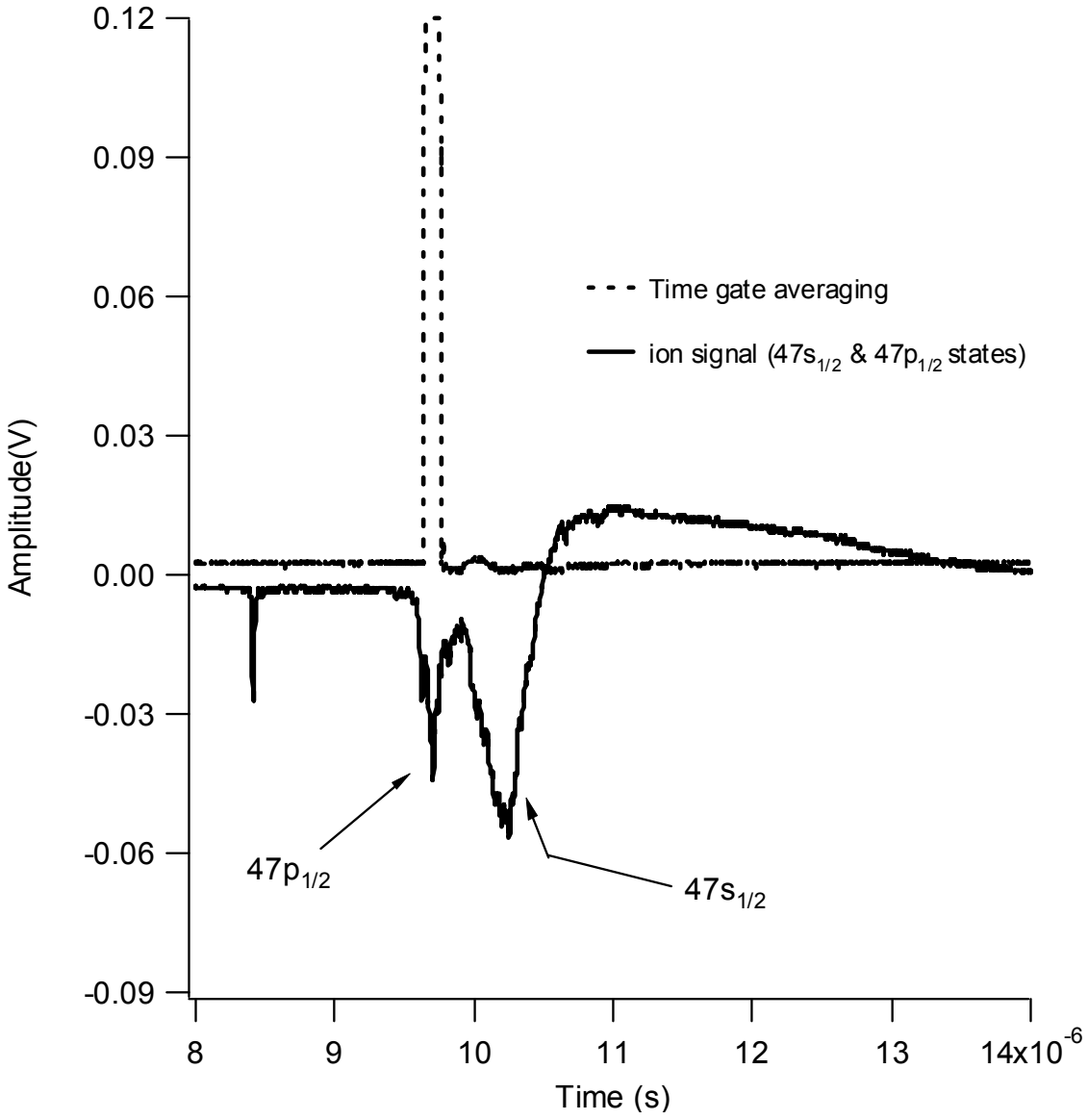


Figure 3-4: Traces of the timing gate of a boxcar and ion signals of $47s_{1/2}$ and $47p_{1/2}$ states observed on an oscilloscope. The ion signal is being averaged over 105 ns time-period starting $\sim$10 $\mu s$ after the light pulse.

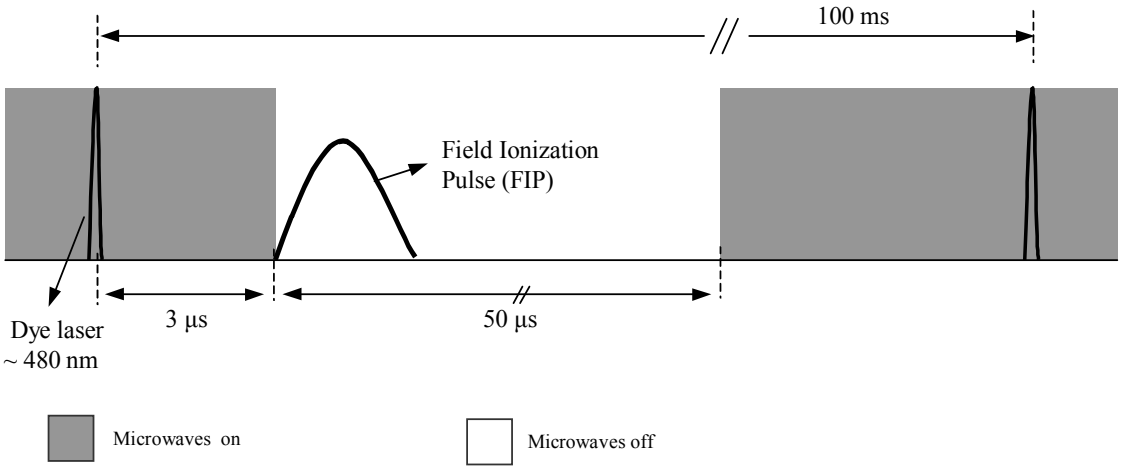


Figure 3-5: Timing diagram of the experiment to observe microwave transitions. The atoms were excited using microwaves from $47s_{1/2}$ to $47p_{1/2}$. The microwaves were turned off right before the FIP pulse, that is 3 $\mu s$ after the trigger from Q-switch of the YAG laser, and turned on 50 $\mu s$ after the FIP pulse. This was repeated every 100 ms (every laser shot).

turn them back on $50\mu s$ later. The microwaves are kept on for most of the time between laser pulses. The reason is that the power of the microwaves inside the synthesizer is being measured after the switch that pulses the signal. Therefore, the power meter inside the device can not measure the power of the microwaves properly if the microwaves have a low duty cycle.

As shown in the timing diagram in Fig. 3-5, the atoms are excited to Rydberg states in the presence of the microwave field and the ionizing electric field comes about $3\mu s$ after the laser pulse.

## 3.2 Power Broadening

The linewidth of the microwave transitions between the $47s_{1/2}$ and $47p_{3/2}$ Rydberg states of Rb can be influenced by the intensity of the microwave field. The interaction of the time-varying electric field of the microwaves with the Rydberg states can broaden the observed transitions. In this section, the Rabi theory is employed to investigate this interaction [48]. The experimental data showing the effect of microwave power on the observed transitions will also be presented.

The microwave field can be described by a classical EM plane wave,

$$\mathbf{E} = \mathbf{E}_0 \cos(\omega t - kz). \tag{3.1}$$

Since in the present experiments the microwave frequency is only resonant with the energy levels $47s_{1/2}$ and $47p_{3/2}$, it is possible to consider a two-level atomic system with energy levels $E_a$ and $E_b$ for this discussion. Excitation of an atomic transition by microwaves leads to a time-dependent probability of the atom being in either the upper or the lower level. If all atoms were initially in state $a$, the probability of an atom, $b(t)b^*(t)$, being in the level with energy $E_b$ is [34],

$$|b(t)|^2 = (\frac{R_{ab}}{\Omega})^2 \sin^2(\frac{\Omega t}{2}) \tag{3.2}$$

in which

$$R_{ab}^2 = (\frac{D_{ab}E_0}{\hbar})^2 \tag{3.3}$$

$$\Omega = \sqrt{(\omega_{ba} - \omega)^2 + (\frac{D_{ab}E_0}{\hbar})^2} \tag{3.4}$$

where $D_{ab}$ is the atomic dipole matrix element, $\omega$ is the microwave frequency, $\omega_{ba}$ is equal to $(E_b - E_a)/\hbar$, $\hbar = 1.0546 \times 10^{-34}$ J . s is Planck's constant, and $t$ is the duration of the time that the atom is being exposed to the microwaves. $R_{ab}$ is known as the Rabi frequency. Equation 3.2 shows that the probability of an atom being in the energy states $E_a$ or $E_b$ oscillates with the frequency $\Omega/2\pi$.

In the experiment described in this section, the atomic dipole matrix element $D_{ab}$ is,

$$D_{47p_{3/2},47s_{1/2}} =< 47p_{3/2}(m_j = 1/2) \ \ |r\cos\theta| \ \ 47s_{1/2}(m_j = 1/2) >= 1038.2 \ \ a.u. \tag{3.5}$$

This calculation is a by-product of the Stark map calculation which will be discussed later in Sec. 5.2.2 [49].

In Eq. 3.2 the average of the $\sin^2(\frac{\Omega t}{2})$ term, 1/2, must be taken into account. The reasons that this term should be replaced by its average are as follows.

1. Rydberg states are Zeeman shifted inside the trap due to the magnetic field inhomogeneity

induced by the anti-Helmholtz coils (AHC). Thus, $\omega_{ba} = (E_b - E_a)/\hbar$ in Eq. 3.4 is not the same for all of the atoms inside the trap.

2. The atoms are not being excited to the $47s_{1/2}$ states by the dye laser at the same time due to the 10 ns width of the laser pulse. Therefore, they are not being exposed to the microwaves for the same amount of time. If the frequency, $\Omega$, is calculated for a value of the $\omega$ close to $\omega_{ba}$, and $E_0 = 0.55\,\mathrm{V/m}$, then $\Omega$ would be on the order of $\sim 10^7\,\mathrm{Hz}$, while the reciprocal of the exposure time, $1/t$, for a microwave pulse width, $t = 3\mu s$, would be on the order of $10^5\,\mathrm{Hz}$. Hence, the population of the atoms oscillates between the energy levels $E_a$ and $E_b$ many times during the time that it is being irradiated by the microwaves. This leads to random phase variations much greater than $2\pi$. Thus, for uniformly distributed random phase the $\sin^2(\frac{\Omega t}{2})$ term averages to 1/2.

Now, considering the average of the $\sin^2(\frac{\Omega t}{2})$ term in Eq. 3.2, the population probability, $|b(t)|^2$, has a Lorentzian profile with half width,

$$(HW) = \frac{D_{ab}E_0}{\hbar}. \tag{3.6}$$

Since $(HW)$ is proportional to the amplitude of the electromagnetic wave, $E_0$, the linewidth increases with increasing intensity. This is called power broadening.

Figure 3-6 shows the effect of microwave power broadening on the $47s_{1/2} \rightarrow 47p_{3/2}$ transition. The spectra was taken with three different microwave powers, $-25$ dBm, $-40$ dBm, and $-50$ dBm, which results in 29.20 MHz, 4.67 MHz, and 4.62 MHz full width half maxima (FWHM). This also results in $E_0$ being $1.032\,\mathrm{V/m}, 0.166\,\mathrm{V/m}, 0.165\,\mathrm{V/m}$ respectively, using Eqs. 3.5 and 3.6.

By estimating the microwave power density at the location of the trapped atoms, $E_0$ may be determined independently. The insertion losses of the microwave components must be subtracted from the output power of the synthesizer. The amount of microwave power being absorbed by the atoms also depends on the location of the trap with respect to the antenna.

Consider $-25$ dBm output power for the microwaves. After including the insertion losses (Sec. 2.8), 4.2 dB, the microwave power radiated from the antenna decreases to $-29.2$ dBm ($1.20 \times 10^{-6}\,\mathrm{W}$). It is also considered that roughly half of the output power is bounded between

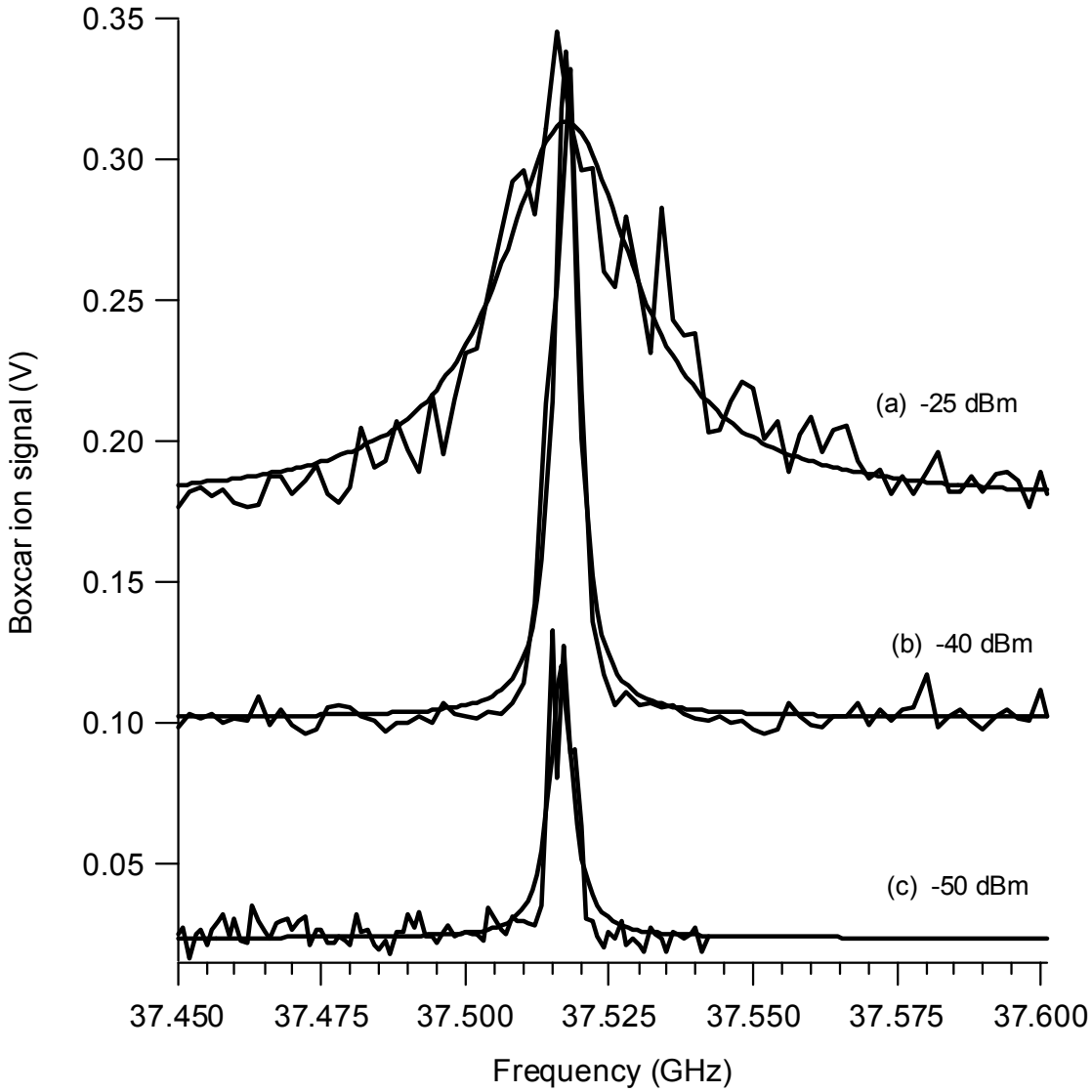


Figure 3-6: Power broadening effect of microwaves on the $47s_{1/2} \rightarrow 47p_{3/2}$ transition. The spectra were taken with three different microwave powers; trace (a), $-25$ dBm, trace (b), $-40$ dBm; trace (c) $-50$ dBm. The full width half maxima of the spectra are 29.20 MHz, 4.67 MHz, and 4.62 MHz respectively. For the sake of clarity, traces (a) and (b) have vertical offsets 0.15 and 0.075. The time averaged boxcar gain was changed for each spectra to enhance the signal, hence the vertical scales of these spectra can not be compared to each other.

the Half Power Beamwidth[2] (HPBW) of the antenna. Now using the HPBW information and the separation of the antenna from the trap, which is 5.7 cm, the microwave power density in the trap region would be $1.375 \times 10^{-8}\,\mathrm{W}\,/\,\mathrm{cm}^2$. The Poynting vector equation can be used to estimate $E_0$ [50],

$$I = \frac{1}{2}\,\frac{1}{377\Omega}\,|E_0|^2 \tag{3.7}$$

where $I$ is the microwave power density in $\mathrm{W}\,/\,\mathrm{cm}^2$ and $E_0$ is in the units of $\mathrm{V}\,/\,\mathrm{cm}$. From this equation, in contrast from the observed linewidth and the Rabi theory, it was found that $E_0 = 0.323, 0.057$, and $0.018\,\mathrm{V}\,/\,\mathrm{cm}$ for corresponding output powers of $-25$ dBm, 40 dBm, and $-50$ dBm.

The discrepancies between these values of $E_0$ and the values calculated using the linewidths of the experimentally observed transitions and Eq. 3.6 can be explained as follows. In considering the radiation pattern of the antenna, it is assumed that roughly half of the power is uniformly distributed within the Half Power Beamwidth (HPBW). However, this is an approximation which is likely to underestimate $E_0$. The chamber reflects microwaves to the trap which also could increase $E_0$.

Reducing the output power of the microwaves to $-60$ dBm did not improve the linewidth, instead, it reduced the intensity of the signal. As illustrated in Fig. 3-6 lowering the output power from $-40$ dBm to $-50$ dBm (traces (b) and (c)) did not improve the linewidth as much as it did when reduced from $-25$ dBm to $-40$ dBm (traces (a) and (b)). Therefore, the linewidth in trace (c) must be due to another effect that broadens the transitions, independent of the microwave power. The effect of the magnetic field inhomogeneity induced by the AHC on the Rydberg states broadens the transitions. This will be discussed in chapter 4 and also it will be shown how this effect was minimized by switching the AHC's winding current on and off.

For all the experiments which will be presented in chapters 4 and 5, the microwave power is $P = -50$ dBm. It would be useful to estimate the line broadening of the microwave transitions due to the power broadening for $P = -50$ dBm. The following calculations lead to this result.

[2]The HPBW is the angular width between the two directions of the microwave antenna at which the main beam gain function is one-half its maximum value within a plane containing the maximum gain of the main beam lobe.

From Eq. 3.7 it is realized that,

$$E_0(\mathrm{V\,/\,cm}) \propto \sqrt{I(\mathrm{W\,/\,cm^2})}. \tag{3.8}$$

The power density at the trap region, $I$, is proportional to the total microwave power, $P$,

$$I(\mathrm{W\,/\,cm^2}) \propto P(\mathrm{W}). \tag{3.9}$$

The numerical constants which turn the above relations into an equality are identical for all three spectra shown in Fig. 3-6, due to the same experimental conditions. Hence, they do not need to be taken into account in the following calculations. From Eqs. 3.8 and 3.9,

$$E_0(\mathrm{V\,/\,cm}) = k\sqrt{P(\mathrm{W})} \tag{3.10}$$

where $k$ is also a numerical constant, identical for all the spectra. Therefore, Eq. 3.6 can be rewritten as,

$$(HW) = \frac{D_{ab}k\sqrt{P}}{\hbar}. \tag{3.11}$$

The constant numerical factor $D_{ab}k/\hbar$ can be calculated from this equation and the observations. The same result is expected to be obtained for the two output powers $-25$dBm and $-40$dBm, but a different result for $-50$dBm. The line broadening for this case is due to other effects, independent of that of the power broadening.

If the $HW$'s for the traces (a) and (b) in Fig. 3-6 are inserted in Eq. 3.11 along with their relative powers, the values obtained for $D_{ab}k/\hbar$ would be 259.63 and 233.5 respectively. Their average value is $\langle D_{ab}k/\hbar\rangle = 246.56$. Using Eq. 3.11, the line broadening $(HW)$ due to the power broadening effect for an output power $-50$dBm is 0.78 MHz .

However, it should be mentioned that in the above calculations the $47s_{1/2} \rightarrow 47p_{3/2}$ transition is considered, while the $47s_{1/2} \rightarrow 47p_{1/2}$ transition is studied in chapters 4 and 5. Since the matrix element $D_{ab}$ is different for these two transitions, by considering Eq. 3.6, the line broadening $(HW)$ due to the power broadening effect is slightly smaller, 0.748 MHz.

It will be shown in Sec. 4.4.1 that the effective coupling will be different between different $M_J$ states, in the $M_J$ resolved case (see for example, Fig. 4-13, the microwave spectrum of the

$47^2S_{1/2} - 47^2P_{1/2}(\Delta M_J = 0, \pm 1)$ transitions).

# Chapter 4

# Magnetic field

## 4.1 Introduction

Precision spectroscopy of trapped atoms in a Magneto-Optical Trap (MOT) is difficult, since a MOT relies on the spatial inhomogeneity of the atomic energy levels induced by the inhomogeneous anti-Helmholtz magnetic field. Spatial inhomogeneity of the energy levels broadens the transition frequencies, thus limiting the precision of spectroscopy. In this experiment, the current in the Anti-Helmholtz coils (AHC) was switched off to minimize field inhomogeneity, which resulted in a better resolution.

This chapter begins with a description of the Zeeman effect of fine ($LS$ coupling) and hyperfine structure ($IJ$ coupling). These effects must be considered in order to determine the observed transitions. The range of inhomogeneous magnetic fields that the atoms in the trap experience is estimated in section 4.3. In section 4.4, experimental results are presented for microwave spectra in the case where the current to the AHC is left on and when it is switched off. The results are interpreted in this section.

## 4.2 Zeeman Effect of Fine and Hyperfine Structures

In all the experiments described in this thesis, the interaction of the atomic electrons with an inhomogeneous external magnetic field $B$ should be considered. Although there is a field gradient inside the atomic cloud due to the AHC, each atom sees a homogeneous magnetic

field due to its small size compared to the field gradient, which is equal to $18.75\,\mathrm{G}\,/\,\mathrm{cm}$ (from Eq.2.6). Hence a homogeneous $B$ field can be considered in describing the Zeeman effect. This section is adapted from Refs. [51] and [52].

It is easiest first to consider the Rb atom without hyperfine structure. In this case $M_J$ is a good quantum number and the atom has a $2J+1$ degeneracy associated with the different possible values of $M_J$. In the presence of the external magnetic field $B$, these different states will have different energies due to different orientations of the magnetic dipoles in the external field. The splitting of these energy levels is called the Zeeman effect.

In the presence of an external magnetic field of strength $B$, the following magnetic interaction energies have to be considered,

$$H_1 = \zeta \mathbf{L}\cdot\mathbf{S}; \qquad H_M = -\boldsymbol{\mu}\cdot\mathbf{B} \tag{4.1}$$

where for Hydrogen-like atoms,

$$\zeta = -\frac{e}{2c^2 m_0^2}\frac{1}{r}\frac{dV}{dr} \tag{4.2}$$

and $r$ is the radial distance of the valance electron from nucleus. In Eq. 4.1, $H_M$ is the Hamiltonian of the Zeeman effect and $\boldsymbol{\mu}$ is the total magnetic moment of the electrons. The total magnetic moment of the electrons, $\boldsymbol{\mu}$, can be written in terms of the orbital and spin magnetic moments,

$$\boldsymbol{\mu} = \boldsymbol{\mu}_l + \boldsymbol{\mu}_s = -\mu_B(g_l\mathbf{L} + g_s\mathbf{S}) \tag{4.3}$$

where $\mu_B = e\hbar/2m_0 = 9.2732\times10^{-24}\,\mathrm{J}\,/\,\mathrm{T}$ is the Bohr magneton and the orbital and spin $g$-factors are $g_l \equiv 1$ and $g_s \approx 2$ respectively.

By considering the weak field approximation in which $H_1 \gg H_M$ (Eq. 4.1), the energy splitting, $\sim \mu_B B$, produced by the external field is small compared to the fine structure.

The Zeeman energy shift in first order perturbation theory is given by,

$$\Delta E = \langle \gamma LSJM_J \,|H_M|\, \gamma LSJM_J \rangle \tag{4.4}$$

where the fine-structure level is labelled by $(\gamma LSJ)$ in a weak field. The effective form of $H_M$

is, (from Eq. 4.1 and 4.3),

$$\begin{aligned} H_M &= \mu_B(\mathbf{L}+g_s\mathbf{S})\cdot\mathbf{B} \\ &= \mu_B B(L_z+g_s S_z), \end{aligned} \tag{4.5}$$

where the magnetic field $B$ is applied along the z-axis.

To evaluate the matrix element of $L_z$ and $S_z$, first $\mathbf{L}$ must be projected on to $\mathbf{J}$, and then projected on to the $z$-axis,

$$\langle \gamma LSJM_J \left| L_z \right| \gamma LSJM_J \rangle = \langle \gamma LSJM_J \left| \frac{(\mathbf{L}\cdot\mathbf{J})}{J(J+1)} J_z \right| \gamma LSJM_J \rangle. \tag{4.6}$$

Similarly for $S_z$,

$$\mathbf{S}\cdot\mathbf{J} = \frac{1}{2}(\mathbf{J}^2 - \mathbf{L}^2 + \mathbf{S}^2) \tag{4.7}$$

$$\mathbf{L}\cdot\mathbf{J} = \frac{1}{2}(\mathbf{J}^2 + \mathbf{L}^2 - \mathbf{S}^2). \tag{4.8}$$

The energy shift from Eq. 4.4 and Eq. 4.5 can be rewritten as,

$$\Delta E = \langle \gamma LSJM_J \left| g_J \mu_B B J_z \right| \gamma LSJM_J \rangle = g_J \mu_B B M_J \tag{4.9}$$

where $g_J$ is the Landé $g$ factor for the particular state being considered,

$$g_J = \frac{J(J+1)+L(L+1)-S(S+1)}{2J(J+1)} + g_s \frac{J(J+1)-L(L+1)+S(S+1)}{2J(J+1)}. \tag{4.10}$$

From Eq. 4.9 and Eq. 4.10, it can be seen that the energy shift caused by the Zeeman effect is linear in $B$ and $M_J$. Thus, for a set of states with particular values of $n, L$, and $J$, the individual states with different $M_J$ will be equally spaced in energy, separated by $g_J \mu_B B$ (Fig. 4-1). However, the spacing will in general be different for a set of states with different $n$, $L$, and $J$, due to the difference in the Landé $g$ factor.

Figure 4-1 shows the Zeeman effect of the fine structure of Rb for the $^2S_{1/2} - ^2P_{1/2}$ and $^2S_{1/2} - ^2P_{3/2}$ resonances, and all the allowed transitions due to the electric dipole selection rules

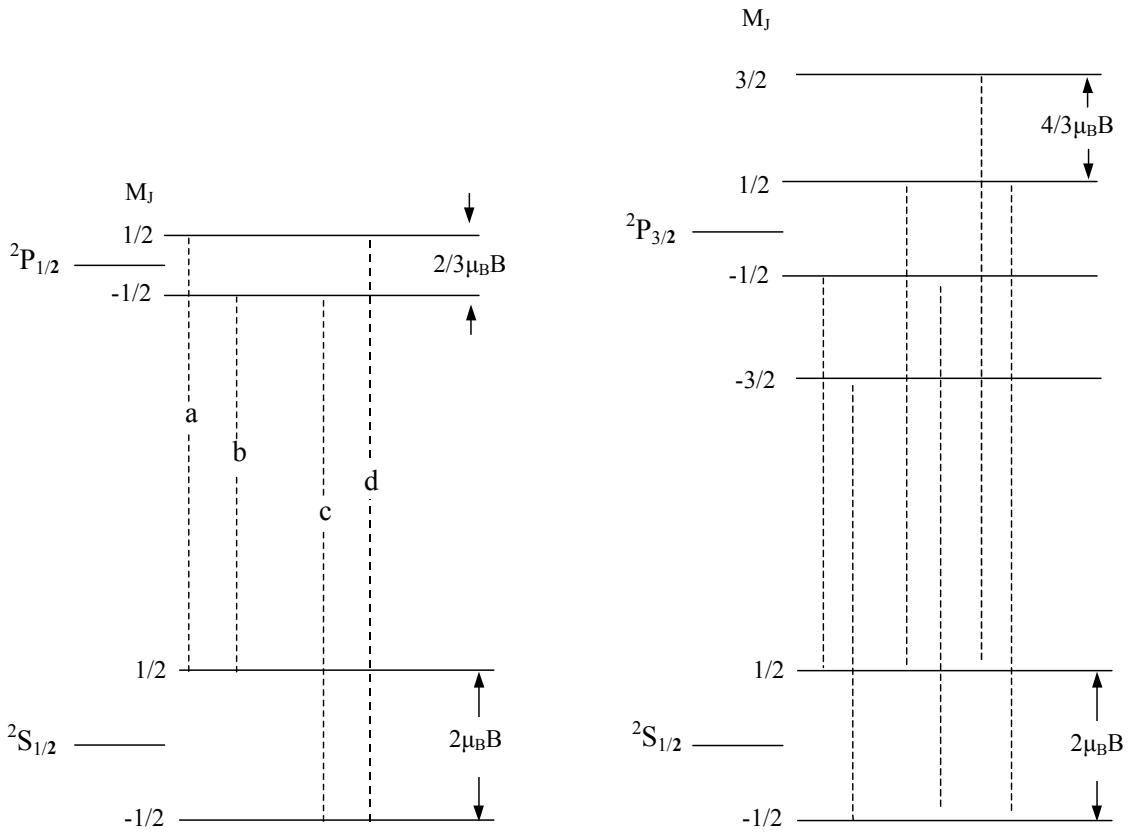


Figure 4-1: Schematic diagram of the Zeeman effect of the fine structure of Rb, ${}^2S_{1/2} - {}^2P_{1/2}$ and ${}^2S_{1/2} - {}^2P_{3/2}$ and the allowed transitions, $\Delta M_J = 0, \pm 1$.

for $M_J$,

$$\Delta M_J = 0, \pm 1 \tag{4.11}$$

where the transition $M_J = 0 \rightarrow M'_J = 0$ is not an allowed transition if $\Delta J = 0$ [51]. From Eq. 4.9, the spacings between the magnetic sublevels of the $^2S_{1/2}$, $^2P_{1/2}$, and $^2P_{3/2}$ states are $2\mu_B B$, $2/3\mu_B B$ and $4/3\mu_B B$ respectively. The $S$ states are chosen to be analyzed in the following parts due to their large intervals when compared to the intervals of the $P$ states (Fig. 4-1). However, this procedure can be applied to the $P$ states as well.

The formalism of the Zeeman effect of the hyperfine structure is similar to that of the fine structure. However, they have significantly different orders of magnitude. Whereas the strong-field case is rare in fine structure, this is not so in hyperfine structure. Furthermore, since the nuclear magnetic moment $\mu_I$ is much smaller than the electronic magnetic moment $\mu_J$, it does not take a particularly strong external field to make the Zeeman effect comparable in magnitude to the strength of the hyperfine interactions. Thus, the approximation of a small external field is not practical when discussing the Zeeman splitting of hyperfine structure. However, these splittings can be calculated for any level using the Breit-Rabi formula [52],

$$\begin{aligned} \Delta E(F, M_F) &= -\frac{h\Delta\nu}{2(2I+1)} - g'_I \mu_B B M_F \pm \frac{1}{2} h\Delta\nu * \{1 + \frac{4M_F}{2I+1} x + x^2\}^{1/2} \\ \Delta E(F, M_F) &= \frac{I}{2I+1} h\Delta\nu \pm \frac{1}{2} g_J \mu_B B, \qquad \text{for} \quad M_F = \pm(I + 1/2) \end{aligned} \tag{4.12}$$

where,

$$x = \frac{(g_J + g'_I)\mu_B B}{h\Delta\nu} \tag{4.13}$$

and $\mu_B$ is the Bohr magneton, $h = 6.62617636 \times 10^{-34}(\mathrm{J\,s})$ is Planck's constant, $B$ is the magnitude of the magnetic field. The upper sign in Eq. 4.12 is taken for states which belong at low field to $F = I + 1/2$ and the lower sign for states which belong to $F = I - 1/2$. For $^{85}$Rb, the total nuclear angular momentum, $I$, is 5/2 and the constants $g'_I$ and $g_J$ are $-0.0002936400$ and 2.00233 respectively [24].In the above equation, $\Delta\nu$ is the separation between the levels $F = I \pm 1/2$ at zero field, which is equal to 3036 MHz for the ground state of $^{85}$Rb.

The results of the Zeeman splitting for the hyperfine levels in the ground state of $^{85}$Rb are shown in Fig. 4-2. The atom has a $2F + 1$ degeneracy associated with the different

possible values of $M_F$. The degeneracy of the states is lifted such that each state has a different corresponding energy in the presence of an external field. As illustrated in Fig.4-2, the energy shifts are linear for a small external field. In order to show the Zeeman splitting of both hyperfine states, $F = 3$ and 2, a stronger magnetic field is considered in Fig. 4-2, compared to typical magnetic fields ($\sim 1.6 \times 10^{-4}\,\mathrm{T}$) in the MOT. The Zeeman splitting of the $F = 3$ hyperfine state in Fig. 4-2 has been magnified in Fig. 4-3, in order to show the separation of the different $M_J$ energy levels for a typical magnetic field in the MOT.

Fine and hyperfine splitting depend on the principal quantum number, $n$. As $n$ increases, the splitting becomes smaller. Wenhui Li *et al.* [8] experimentally measured the $ns$ hyperfine intervals of $^{85}$Rb and $^{87}$Rb for $n = 28$ to $n = 33$, and found the following relationship for the $ns$ hyperfine intervals, $\nu_{hfs}$, and $n^*$,

$$\nu_{hfs} = 14.6(\pm 1.4)\,\mathrm{GHz}(n^*)^{-3}, \tag{4.14}$$

where $n^* = n - \delta_s$ is the effective quantum number of the $s$ states and $\delta_{s_{1/2}} = 3.1311804$ [8] is the quantum defect of the $ns_{1/2}$ states. The hyperfine intervals of the $47s_{1/2}$ state can be obtained from Eq. 4.14, resulting in 0.173 MHz. Similarly, the $np$ fine-structure intervals, $\nu_{fs}$, of $^{85}$Rb can be calculated by [8], [53],

$$\nu_{fs} = 86.9357(\pm 7 \times 10^{-4})\,\mathrm{THz}(n^*)^{-3} - 23.3(\pm 5)\,\mathrm{THz}(n^*)^{-5}. \tag{4.15}$$

Using Eq. 4.15, the $47p_{1/2} - 47p_{3/2}$ fine-structure interval of $^{85}$Rb is 996.218 MHz. Since these two levels are not lifted evenly from the non fine-structure level, the quantum defect $\delta_p$ in $n^* = n - \delta_p$ is the center of gravity of $\delta_{p_{3/2}}$ and $\delta_{p_{1/2}}$ [8],

$$\delta_{p(COG)} = \frac{2}{3} \times \delta_{p_{3/2}} + \frac{1}{3} \times \delta_{p_{1/2}}. \tag{4.16}$$

Considering the Zeeman effect of hyperfine structure in the ground state of $^{85}$Rb with a typical maximum magnetic field $B \simeq 1.6 \times 10^{-4}\,\mathrm{T}$ in the trap, the Zeeman shift, $\Delta E = 4.48\,\mathrm{MHz}$ (using Breit-Rabi formula, Eq. 4.12), is small compared to the hyperfine splitting, $\nu_{hfs} = 3036\,\mathrm{MHz}$ (Fig. 4-2). Thus, the Zeeman shift can be treated as a perturbation. However,

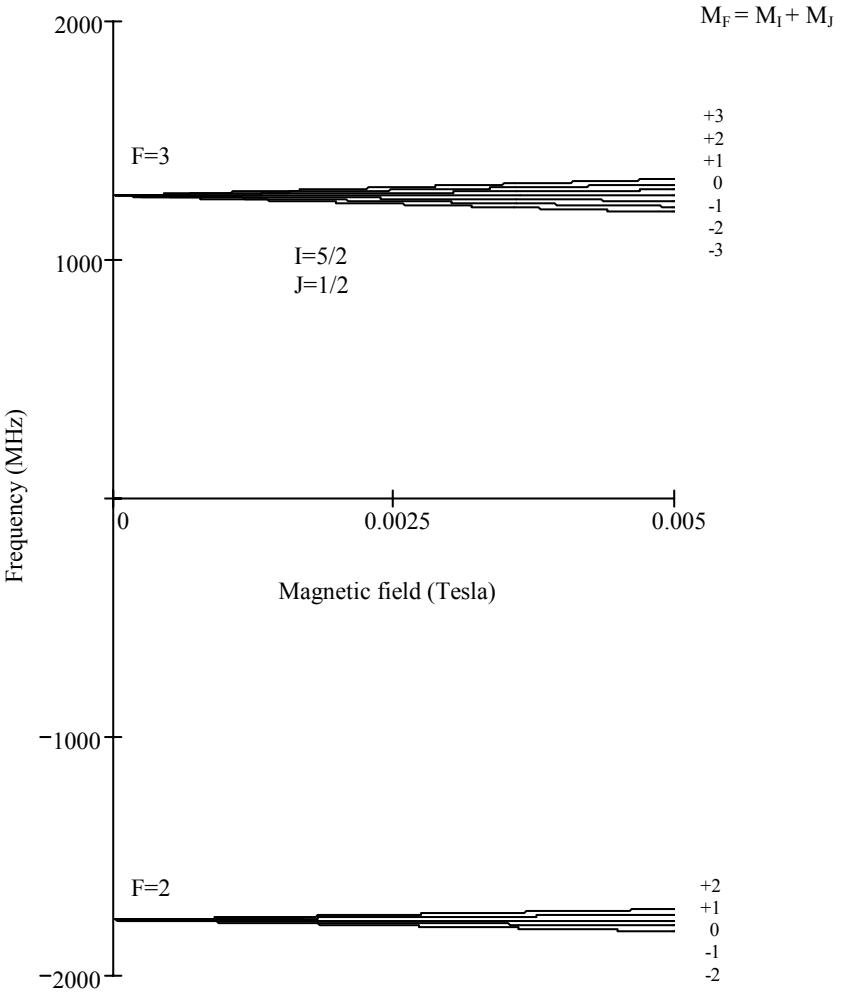


Figure 4-2: Zeeman splitting of the hyperfine levels in the ground state, $5^2S_{1/2}$ ($F = 2, 3$), of $^{85}$Rb using the Breit-Rabi formula [51].

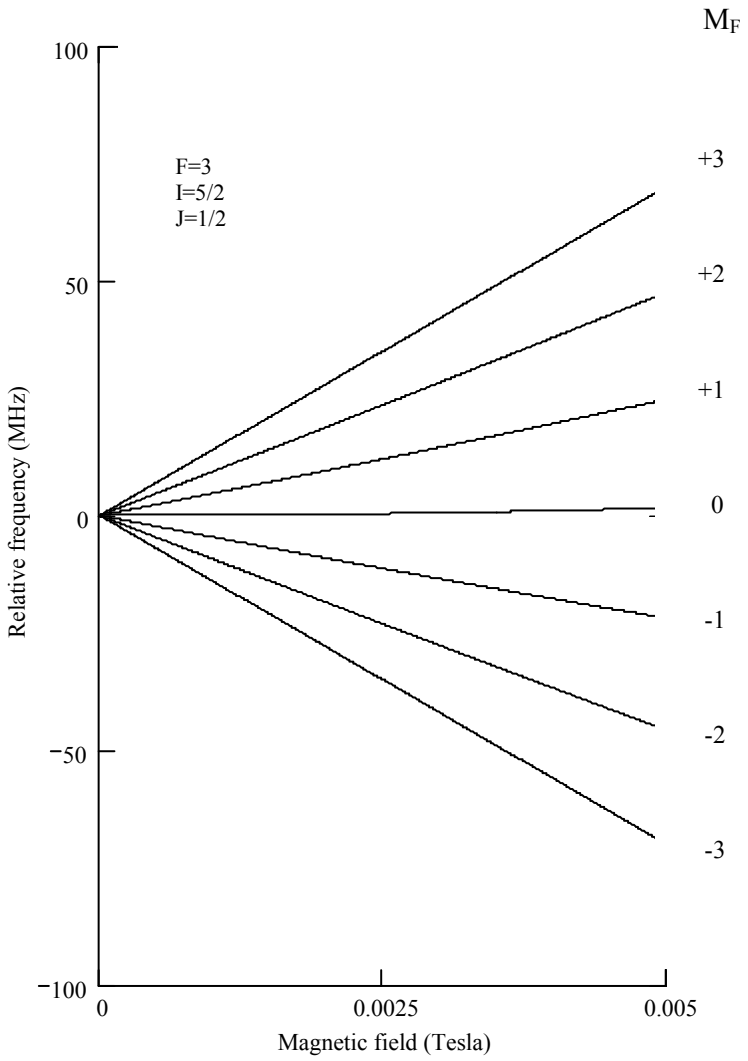


Figure 4-3: Zeeman splitting of the hyperfine level $F = 3$ in the ground state $5^2S_{1/2}$ of $^{85}$Rb using the Breit-Rabi formula [51]. In this plot the $y$ axis shows the relative frequency to the zero field frequency.

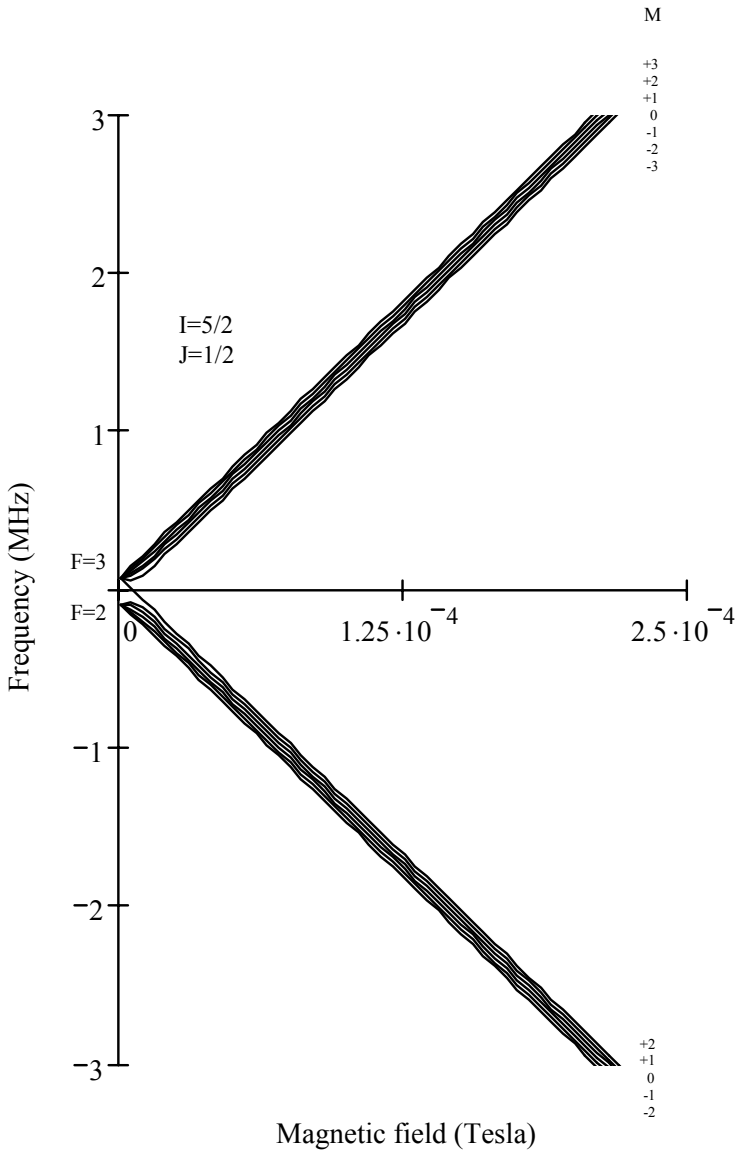


Figure 4-4: Energy level diagram showing the Zeeman splitting of the hyperfine levels in the excited state, $47^2S_{1/2}$ ($F = 2, 3$), of $^{85}$Rb using the Breit-Rabi formula [51].

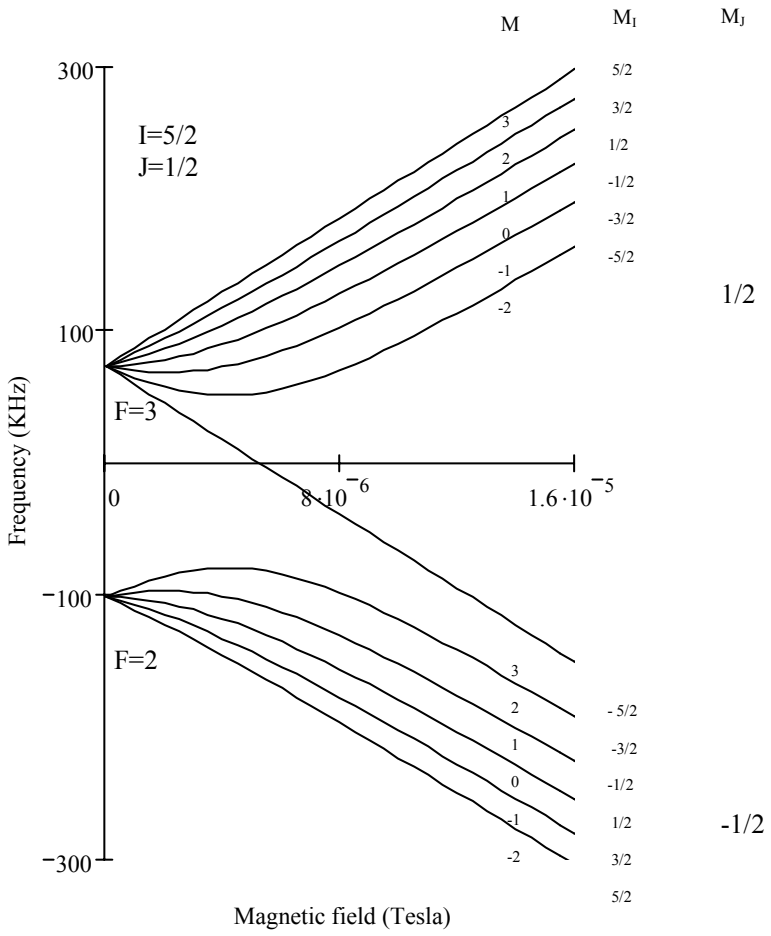


Figure 4-5: Effect of weak and strong magnetic field on the energy levels of $47^2S_{1/2}$ ($F = 2, 3$), of $^{85}$Rb, showing the Zeeman splitting of the hyperfine levels in the excited state.

for the excited state, $47s_{1/2}$, the hyperfine splitting, $\sim 0.173\,\mathrm{MHz}$, is smaller than the Zeeman shift. Therefore, the same magnetic field which is considered to be a weak field for the ground state, is a strong field in the excited state. Thus, for the excited states the hyperfine structure is treated as a perturbation.

Figure 4-4 shows the Zeeman shifts of hyperfine states for the $47s_{1/2}$ $(F = 2, 3)$ state. As illustrated in the graph, the Zeeman shifts are larger compared to the hyperfine splitting and a magnetic field $\gtrsim 1.5 \times 10^{-5}\,\mathrm{T}$ is considered to be a strong field. In Fig. 4-5 the Zeeman shift of the same states are shown using a smaller scale. This figure shows both weak and strong field effect on the energy levels using the Breit-Rabi formula, Eq. 4.12. When a weak field, $B \lesssim 2 \times 10^{-6}\,\mathrm{T}$, is applied, the frequency is linearly dependent to the magnetic field. This dependence does not hold for strong field, $\gtrsim 1.5 \times 10^{-5}\,\mathrm{T}$.

For a magnetic field of $1.6 \times 10^{-4}\,\mathrm{T}$, which is a typical magnetic field inside the trap, the Zeeman separation of the adjacent hyperfine states of $47s$, is on the order of 25 kHz (see Fig. 4-4). This separation is less than the resolution of the observed transitions, therefore they are barely observable. The same applies for the $47p(J = 1/2$ and $3/2)$ states. Since the hyperfine interval of the $p$ states is expected to be less than that of the $s$ states, the Zeeman splitting of the $47p(J = 1/2$ and $3/2)$ hyperfine states is even less than that of the $47s_{1/2}$ states and is not resolvable. However, as mentioned earlier the energy shift caused by the Zeeman effect of the fine structure is much larger than hyperfine structures. According to Eq. 4.9 and Fig. 4-1, the energy shift caused by the Zeeman effect of the fine structure is linear in $B$ and $M_J$. For a typical magnetic field in the trap, this splitting is equal to 4.48 MHz for $s_{1/2}$ states, 1.5 MHz for $p_{1/2}$, and 2.9 MHz for $p_{3/2}$. These splittings are resolvable in the observed transitions.

In the following sections, the aforementioned theory and calculations are used to investigate the experimentally observed transitions.

## 4.3 Magnetic Field Inside the Trap

Due to the field inhomogeneity inside the trap, each atom experiences a different magnetic field depending on where they are located. The shifts of the energy levels of the atoms are proportional to the magnetic field that is experienced by each atom (Eq. 4.9).

Figure 4-6 compares the output of a CCD camera for two clouds of cold atoms obtained on different days. The first two lower graphs show the profile of a slice through each trap and the two upper graphs show the magnetic field as a function of distance from the center of the cloud. As explained in chapter 2, at the center of the cloud the magnetic field is zero and the magnitude of the magnetic field increases through the extent of the trap. The maximum magnetic field that atoms see depends on the size of the cloud. The size of the trap can be changed by different variables such as the power and alignment of the trapping and repump lasers (due to fluctuations in temperature), the amount of Rb being released into the MOT and also the field gradient induced by the AHC. The amount of Rb being released into the trap and the field gradient can be controlled by using reliable power supplies. Any small changes in the alignment of the lasers can change the size of the trap, and hence the maximum magnetic field that atoms see in the MOT.

As illustrated in Fig. 4-6, with a typical field gradient equal to 18.75 G / cm, for a trap size of $\sim 1.2$ mm, the atoms see a magnetic field ranging from 0 to 1.125 G, and for a trap size of $\sim 1.9$ mm, the atoms see a magnetic field ranging from 0 to 1.875 G.

## 4.4 Experimental

The experiments described in this section were carried out following the same procedure explained in Sec. 3.1. Microwave transitions, $47s_{1/2} \rightarrow 47p_{1/2}$, were first driven in the presence of an external magnetic field induced by the AHC. Since the $47p_{3/2}$ state has four magnetic sublevels ($M_J = 3/2, 1/2, -3/2, -1/2$) and the $47p_{1/2}$ state has only two magnetic sublevels ($M_J = 1/2, -1/2$), the $47s_{1/2} \longrightarrow 47p_{1/2}$ resonance was chosen for observing microwave transitions in the following experiments. Some common features of the experiment will now be discussed.

Figure 4-7 shows a spectra of the microwave transitions of $47s_{1/2} \rightarrow 47p_{1/2}$ states in the presence of an external magnetic field $B$. As illustrated in this figure, the observed transitions correspond to $47s_{1/2}(M_J = 1/2) \rightarrow 47p_{1/2}(M_J = 1/2, -1/2)$ and $47s_{1/2}(M_J = -1/2) \rightarrow 47p_{1/2}(M_J = 1/2, -1/2)$. The fine structure energy levels are Zeeman shifted in the presence of the external magnetic field. The $47p_{1/2}(M_J = 1/2, -1/2)$ states are not resolved in this

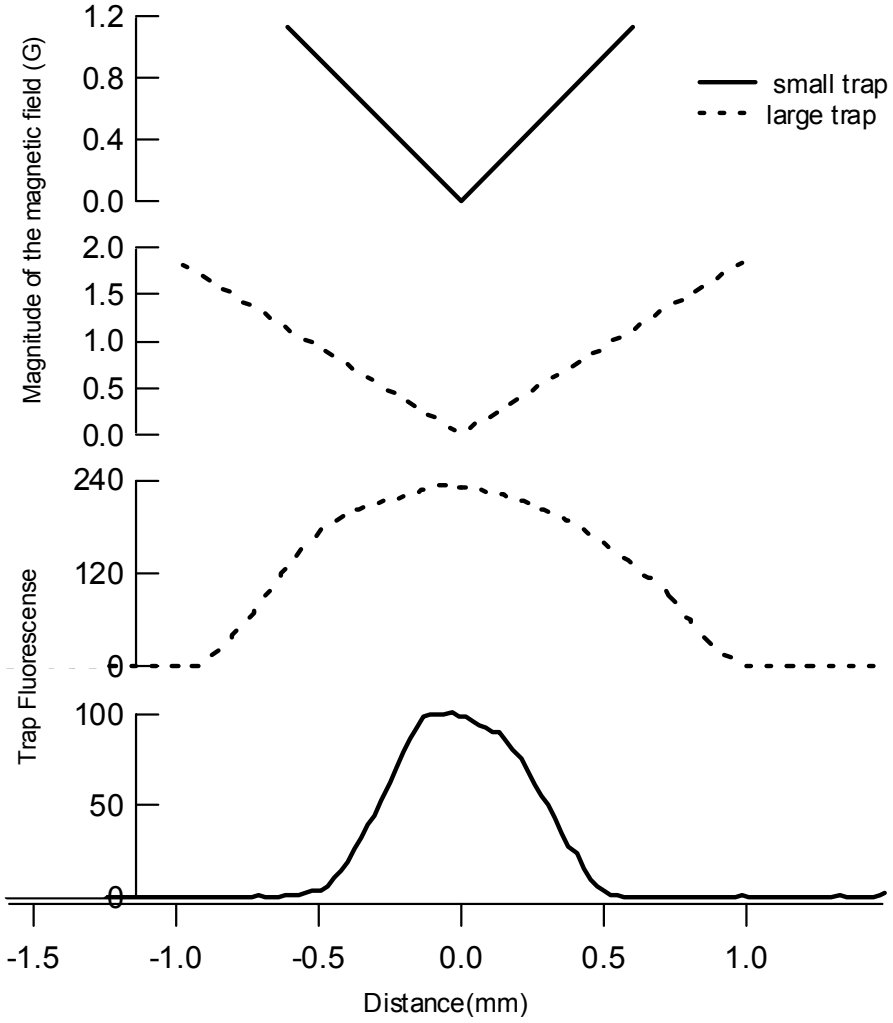


Figure 4-6: Comparison of two different sized traps and their relative magnetic fields. The two upper graphs are plots of the magnitude of the magnetic field $B$ with respect to positionn in the trap. The two bottom graphs are the output of a CCD camera, showing the profile of a slice through the traps. The amplitude of the profile is proportional to the number of atoms. The horizontal axis has been calibrated to correspond to the actual size of the traps. Solid line: AHC's current = 10.4 A, Rb getter's current = 12 A. Dashed line: AHC's current = 6.7 A, Rb getter's current = 10.5 A.

experiment due to the AHC's inhomogeneous magnetic field which broadens the transitions. The peak labeled (a,b) has a FWHM of $\sim 1.23\,\mathrm{MHz}$ in this spectrum.

The spectrum of Fig. 4-7 can be used to measure the magnetic field experienced by the atoms excited to the $47p_{1/2}$ states. As indicated in Fig. 4-6, magnitude of the magnetic field varies from 0 to $\leq 1.85\times10^{-4}\,\mathrm{T}$ depending on the size of the trap. Using Eq. 4.9 and knowing the fine structure interval of $47s$ from the spectra, $2.01\pm0.02\,\mathrm{MHz}$, the relative magnetic field would be equal to $(0.72\ \pm0.01)\times10^{-4}\,\mathrm{T}$ (Fig. 4-6). The Zeeman splitting of the $47p_{1/2}(M_J=1/2,-1/2)$ states in the presence of this magnetic field is $0.672\pm0.006\,\mathrm{MHz}$ (Eq. 4.9). A comparison between this interval and the experimental resolution of the resonances (FWHM$\sim 1.23\,\mathrm{MHz}$) explains why these states are not separated at our experimental resolution.

Considering the applied magnetic field $(0.72\ \pm0.01)\times10^{-4}\,\mathrm{T}$ and Fig. 4-6, it is realized that the signal shown in Fig. 4-7 is mostly contributed by the excited atoms around the center of the trap. This result is expected, because at the outermost shell of the trap there are few atoms and at the center of the trap, despite the fact that the trap is more intense, there is no Zeeman shift, due to the magnetic field being zero in this region.

It should be noted that the spectrum shown in Fig. 4-7 was taken in slightly different conditions from the traps shown in Fig.4-6 and the size, and hence the range of the magnetic field is not exactly the same as what is shown in this figure. In the experiments described in this thesis, the size of the trap was between 1.1 mm to 1.9 mm and the maximum magnetic field inside the trap was ranged from $1.14\ \times10^{-4}\,\mathrm{T}$ to $1.85\times10^{-4}\,\mathrm{T}$.

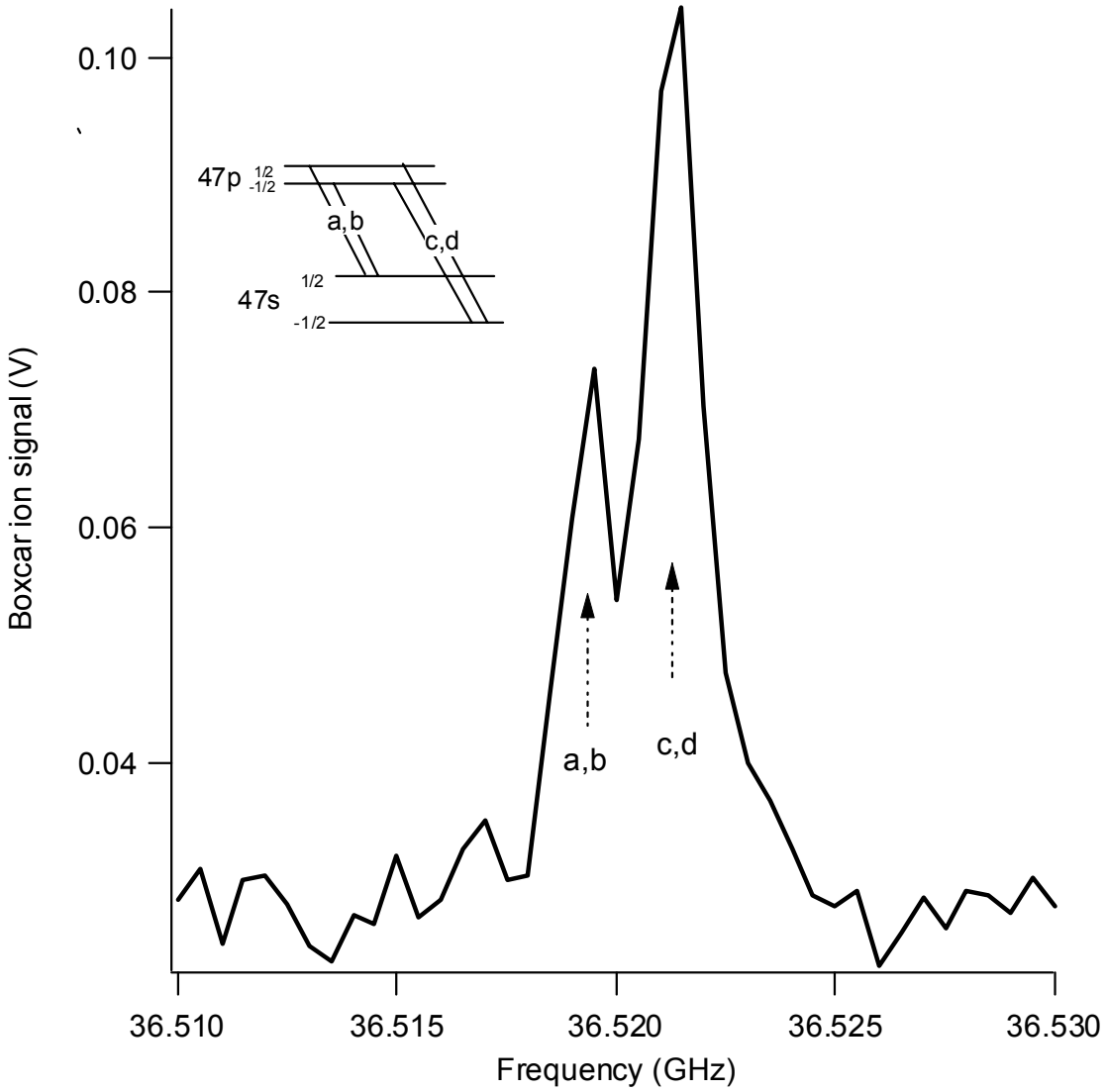


Figure 4-7: Experimental scans of the $47s_{1/2} \rightarrow 47p_{1/2}$ microwave resonances in the presence of an external magnetic field (AHC's current on). The microwave frequency is stepped in increments of 500 kHz, and at each frequency the boxcar signal was averaged over 20 laser shots. Microwave power is $-50$ dBm. Labels in the insert give the line assignment.

### 4.4.1 Pulsed Magnetic Field

In order to minimize the magnetic field inhomogeneity contribution to the width of the transitions, rapid AHC's winding current switching is used instead of having the winding current on continuously. In this section it will be shown that by switching the AHC's winding current on and off, the induced "inhomogeneous" magnetic field is reduced inside the cloud and the atoms feel stronger "homogeneous" magnetic field due to the Helmholtz configuration of nulling coils. In this work, only one pair of the compensating coils has a positive effect on the trap (the ones along the $z$ axis of the MOT in Fig. 2-6) and they produce a field of 6.37 G with typical operating current of 2.7 A. Figure 4-8 shows the circuit used for rapidly switching the AHC's current [44].

Every current winding forms an inductor, for which the following relationships between the back emf ($\epsilon$), the inductance ($L$) and the current ($I$) apply:

$$\epsilon = -L\frac{dI}{dt} \tag{4.17}$$

The circuit shown in Fig. 4-8 permits the inductor (AHC) to generate a large back emf (200 V) in order to maximize $dI/dt$. The SPW47N60C2 metal-oxide-semiconductor field effect transistor (MOSFET) is able to withstand 600V, which is much higher than the winding back emf in this case. This transistor (SPW47N60C2 - MOSFET) is controlled by a MOSFET driver (TPS2814). This driver is triggered by a 5 V pulse signal. The 100VTVS zener diodes are used for power dissipation. When the MOSFET switches off, a positive high voltage builds up and eventually breaks down through the 100VTVS zener diodes until current stops flowing. According to the Eq. 4.17 the higher the back emf the faster the current turns off. Figure 4-9 shows the measured AHC's winding current using the circuit shown on Fig. 4-8, with the current decreasing linearly to zero in 100 $\mu s$.

The winding current of the AHC is switched off 3 ms before the flash lamps of the YAG laser fire and is switched back on 0.5 ms after it fires. The flash lamps have a delay of 240 $\mu$s with respect to the Q-switch of the YAG laser. A timing diagram is shown in Fig. 4-10.

The circuit shown on Fig 4-8 can switch AHC's winding current to zero in 100 $\mu$s, but the magnetic field may take much longer to decay due to eddy currents induced in electrically con-

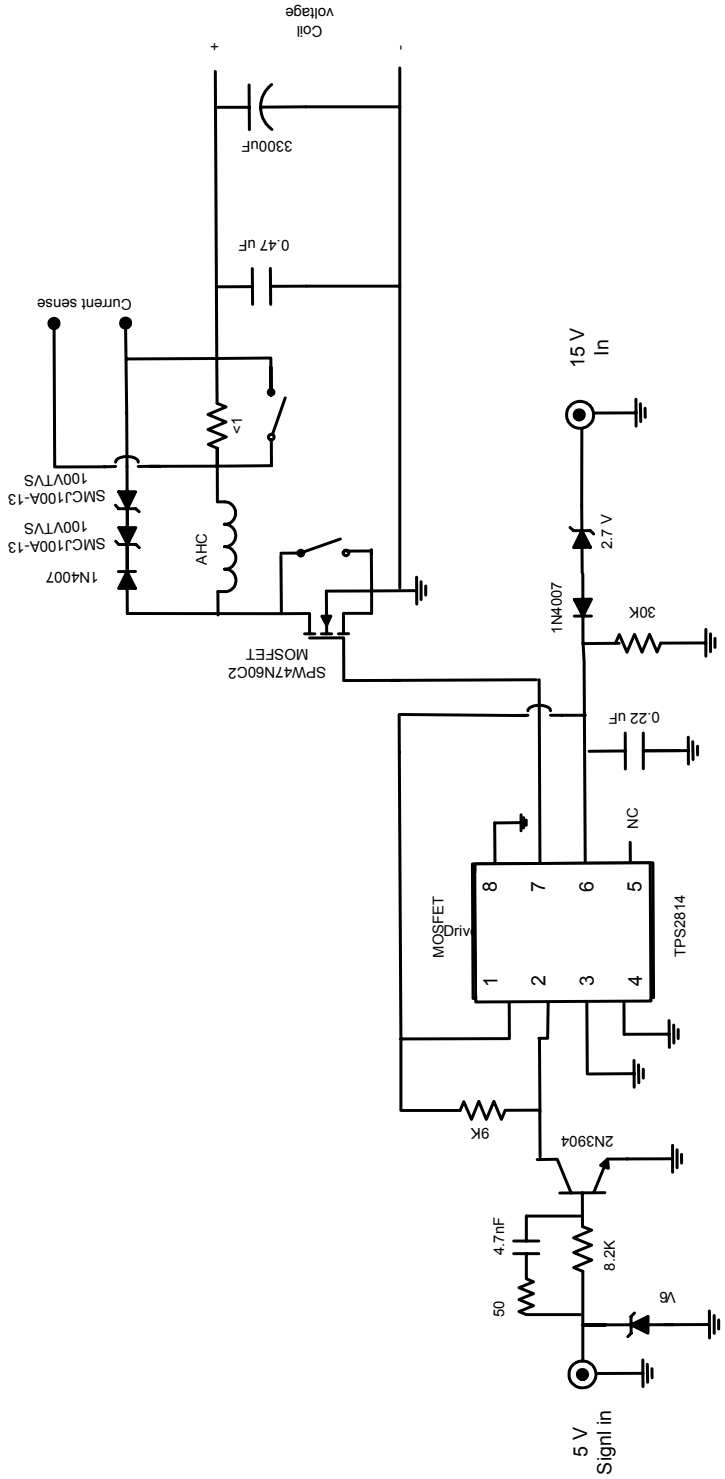


Figure 4-8: Schematic diagram of the circuit for rapidly switching the AHC's winding current [44].

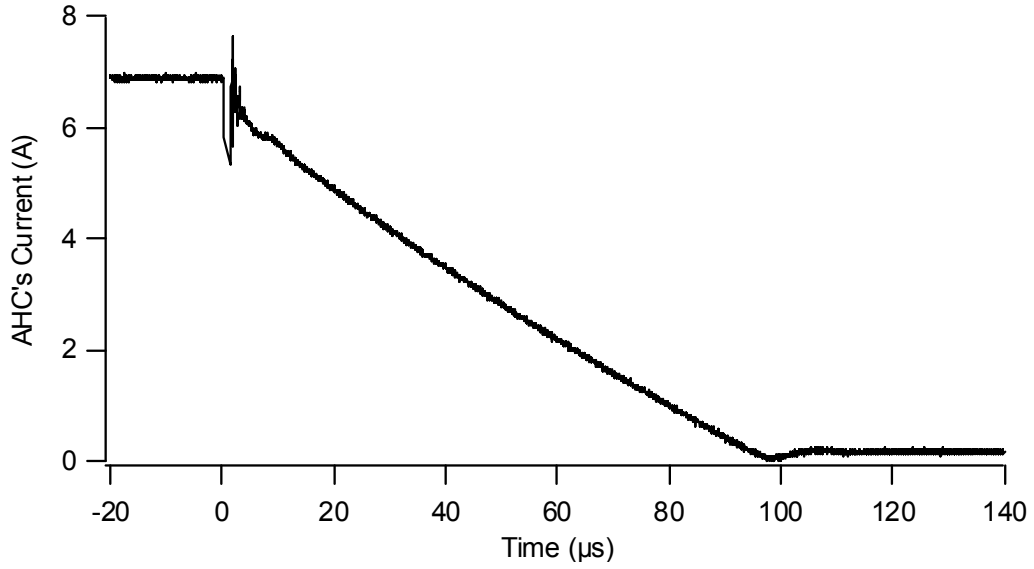


Figure 4-9: AHC's current wave form for the circuit used in Fig. 4-8.

ducting objects near the windings, such as the vacuum chamber, flanges and support structures. Eddy currents induced in these objects will dissipate at a relatively slow rate dictated by the inductance and resistance of the conducting objects.

The spatial inhomogeneity of the transition frequency was minimized through rapidly switching the AHC's winding current which in turn reduces the AHC's field inhomogeneity, rather than turning it off completely because of the induced eddy currents.

Figure 4-11 shows the $47s_{1/2} \longrightarrow 47p_{1/2}$ resonances in the presence of a pulsed magnetic field for three different delay times between switching off the AHC's winding current and the flash lamps of the YAG laser. As shown in this figure, as the delay time is increased from 1 ms to 6 ms the widths of the transitions decrease from 1.38 MHz to 0.778 MHz. Recall Fig.4-7, the Zeeman splitting of fine structure of the $47p_{1/2}$ state is not resolved. However, by reducing the field inhomogeneity, the Zeeman splitting of fine structure of the $47p_{1/2}$ state is clearly resolved with the delay time of 3 ms and 6 ms (Fig. 4-11).

Gaussian fits for two microwave scans of Fig. 4-11 are illustrated in Fig. 4-12 to clearly show the shift of the frequency of the transitions as the delay between switching off the winding current and the flash lamps increases. This is due to the varying homogeneous and inhomoge-

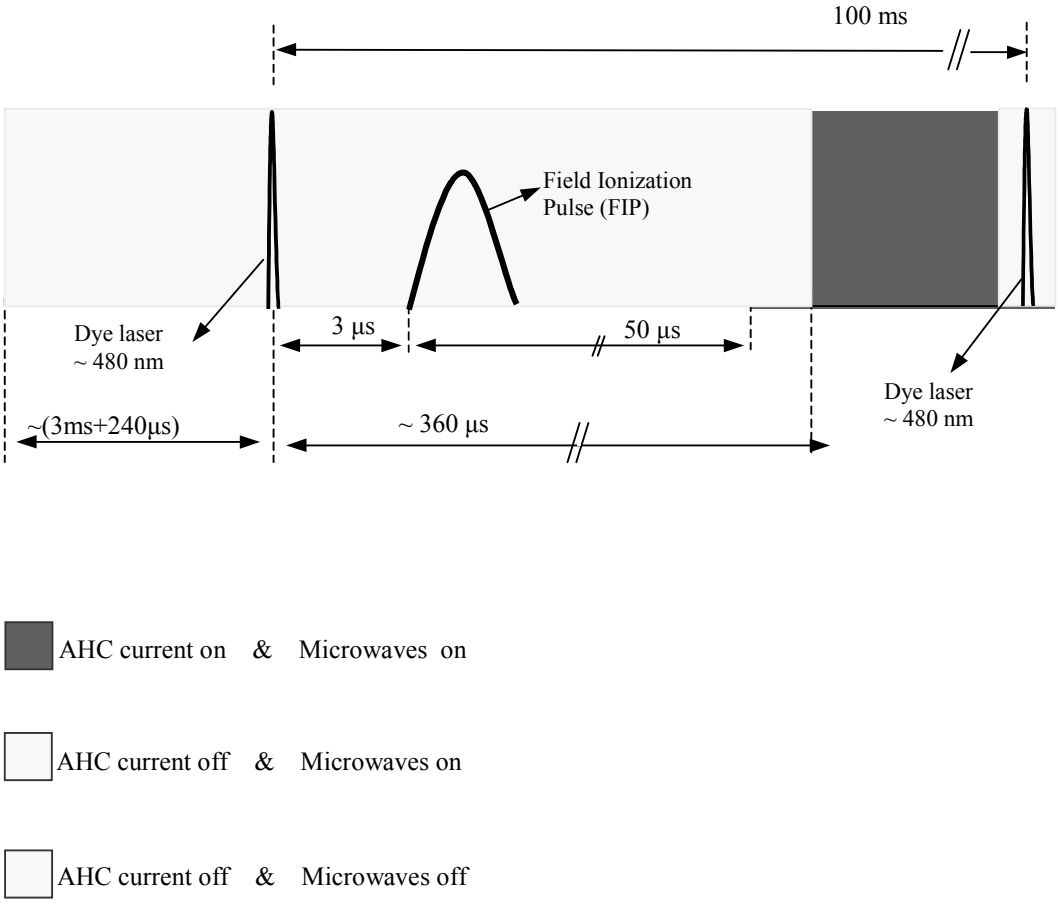


Figure 4-10: Timing diagram for rapidly pulsing the AHC's winding currents.

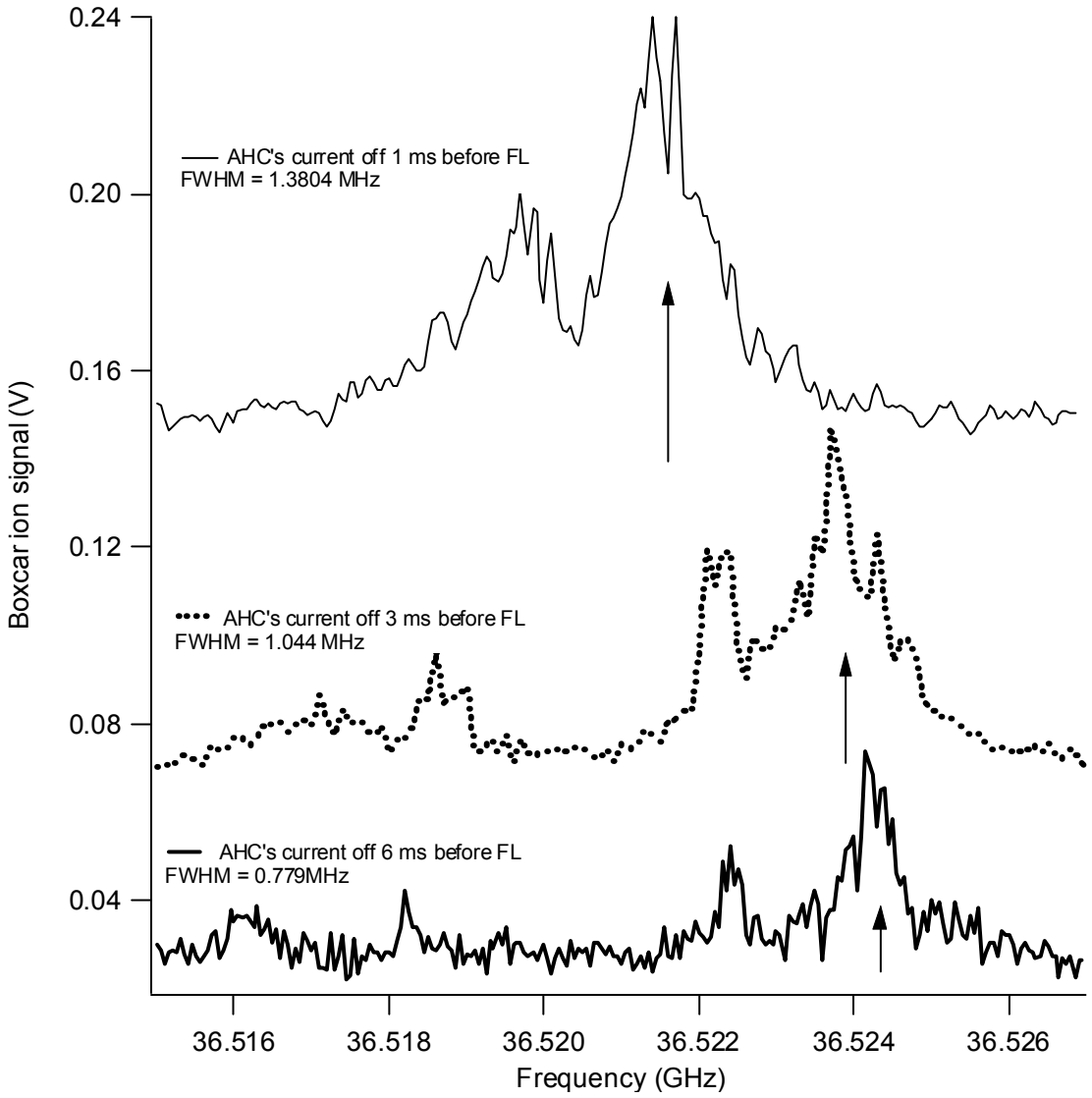


Figure 4-11: Effect of switching off the AHC's winding current on a microwave transition ($47s_{1/2} - 47p_{1/2}$) with different delay times between switching off the current and the flash lamps (FL) of the YAG laser. The microwave frequency is stepped in increments of 80 kHz, and at each increment the boxcar signal was averaged over 40 laser shots. For the sake of clarity, the top spectra has an offset of $y = 0.12\,\mathrm{V}$ and the middle spectra has an offset of $y = 0.06\,\mathrm{V}$ with respect to their initial origins.

neous magnetic field that is applied to the atoms by changing the delay time. As mentioned previously, the inhomogeneous magnetic field induced by the AHC is reduced by rapidly switching their windings current. However, due to the presence of the nulling coils, which produce a field of 6.37 G with operating current of 2.7 A at the center of the coils axis (Sec. 2.3.6), a homogeneous magnetic field is applied to the atoms which becomes stronger as the inhomogeneous magnetic field is minimized. The energy shift caused by the Zeeman effect is linear in $B$ and $M_J$, so for the $47s_{1/2}$ and $47p_{1/2}$ states, the individual states with different $M_J$ will be equally spaced in energy separated by $g_J\mu_B B$. Hence, as $B$ increases the energy separation of the states increases as well (see Eq. 4.9 and Fig. 4-1 ). The difference in the Zeeman shifts of the transitions can be observed as the delay time increases in Fig. 4-12.

Figure 4-13 presents a recording of the $47s_{1/2} \longrightarrow 47p_{1/2}$ resonances with an insert giving the assignment of the lines. This spectrum allows us to measure the magnetic field seen by the Rydberg atoms excited inside the trap.

The frequency difference of the peaks b and c, and also of the peaks a and d, indicate the Zeeman splitting of the $47s_{1/2}$ state which is $5.15 \pm 0.05$ MHz for both sets. Similarly for the $47p_{1/2}$ state the Zeeman splitting can be measured from the frequency difference of the peaks b and a, and from the peaks c and d, which for both sets is $1.59 \pm 0.01$ MHz. Therefore, using Eq. 4.9 the magnitude of the magnetic field can be measured using either the energy separation of the $47s_{1/2}$ states or the $47p_{1/2}$ states. The measured magnetic field should be the same using either of these two intervals. However, the magnitude of the magnetic field due to the $47s_{1/2}$ interval is $(1.84 \pm 0.02) \times 10^{-4}$ T and it is $(1.70 \pm 0.01) \times 10^{-4}$ T if the $47p_{1/2}$ interval is considered.

If a magnetic field of $(1.84 \pm 0.02) \times 10^{-4}$ T (from the separation of the $47s_{1/2}$ states) is applied, the separation of the Zeeman splitting of the $47p_{1/2}$ state is expected to be equal to $1.72 \pm 0.01$ MHz, using Eq. 4.9. A comparison between this separation and the one from the spectra of Fig. 4-13, which is $1.59 \pm 0.01$ MHz, gives rise to 0.13 MHz error. The reason for this discrepancy is unknown.

Let's call the average of the magnetic fields due to the separation of the $47s_{1/2}$ states and of the $47p_{1/2}$ states, $B_1 = 1.77 \times 10^{-4}$ T. Now, recall the field due to the current in the compensating coils. That is $2.36 \times 10^{-4}$ T / A with an operating current of 2.7 A resulting in

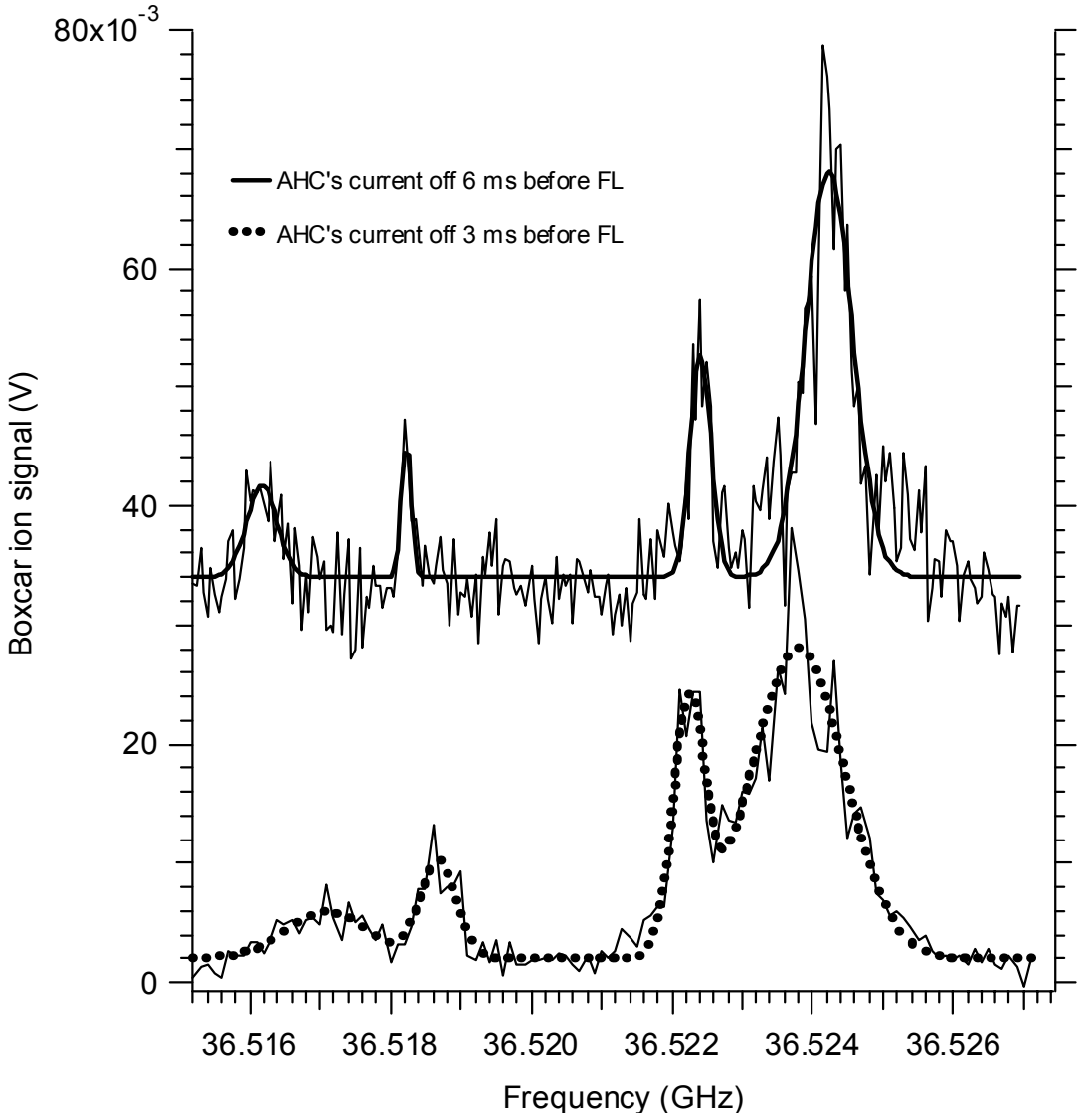


Figure 4-12: Two microwave spectra with different delays between switching off the AHC's winding current and the flash lamps of the YAG laser. Apparent from the data is the difference in the Zeeman shifts of the transitions as the delay increases. The microwave frequency is stepped in increments of 80 kHz, and at each frequency the boxcar signal was averaged over 40 laser shots.

a homogeneous magnetic field of $B_2 = 6.37 \times 10^{-4}\,\mathrm{T}$. The typical magnetic field due to the AHC's before switching the winding current off is $B_3 = 0.72 \pm 0.01 \times 10^{-4}\,\mathrm{T}$.

As explained in Sec. 4.4.1, when the AHC's current is pulsed, the eddy currents induced in electrically conducting objects near the windings prevent the magnetic field from decaying to zero. Therefore, when comparing $B_1$, $B_2$, and $B_3$, it is concluded that the effect of switching the AHC's winding current on and off is to reduce the field inhomogeneities and allow the homogeneous magnetic field due to the compensating coils to have more effect on the observed transitions.

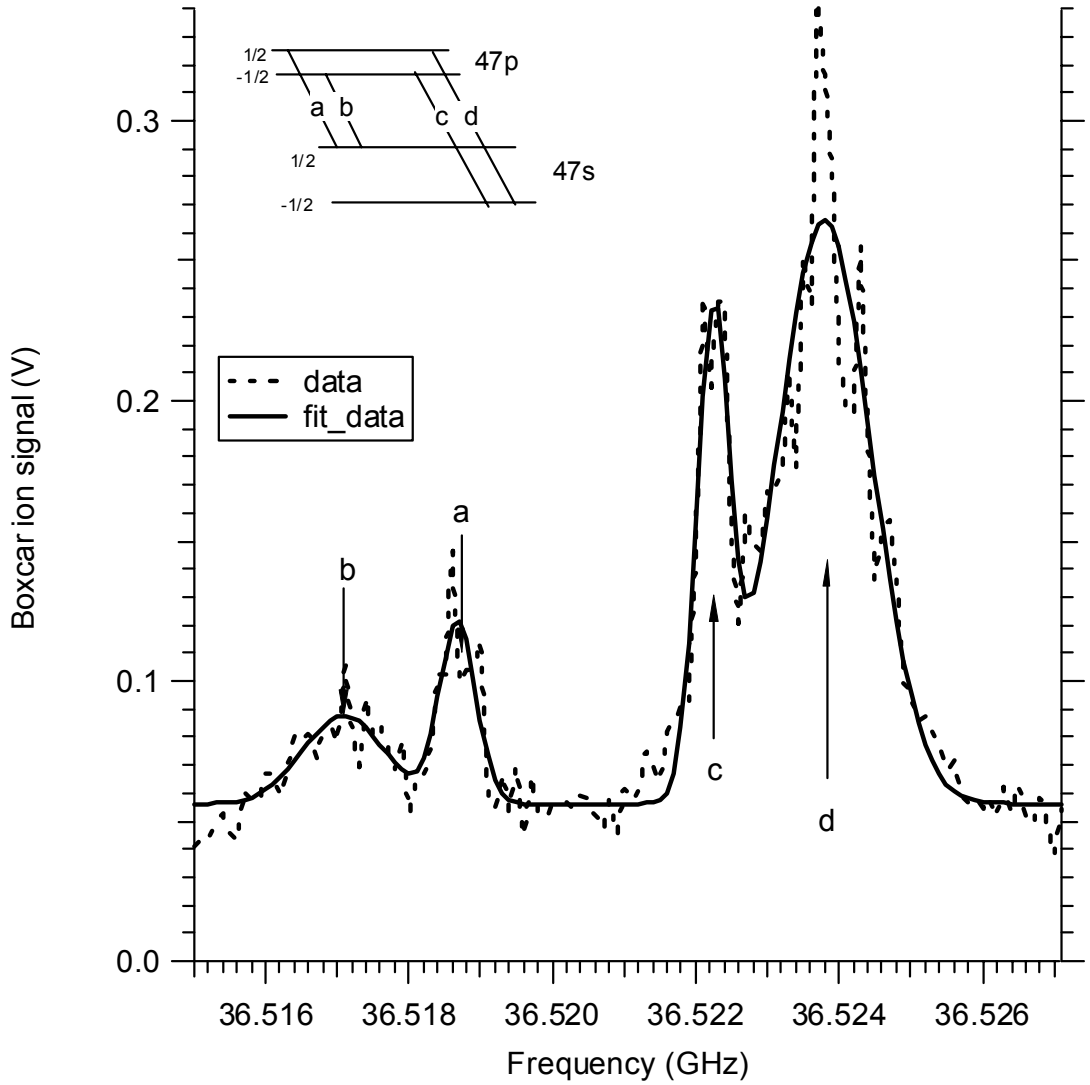


Figure 4-13: The $47s_{1/2}-47p_{1/2}(\Delta M_J = 0, \pm 1)$ transitions as a function of microwave frequency for $^{85}$Rb. The $47s_{1/2}$ is excited by a tunable dye laser. A microwave field is applied and atoms which have made the transition to the $47p_{1/2}$ states are detected by field ionization. The microwave frequency is stepped in increments of 80 kHz, and at each increment the boxcar signal was averaged over 40 laser shots. Labels in the insert give the line assignments.

# Chapter 5

# Electric field

## 5.1 Introduction

Highly excited Rydberg atoms are very sensitive to electric fields, as well as magnetic fields, and they can be used for the measurement and compensation of such fields.

Reducing the effect of inhomogeneous magnetic fields on the microwave transition of Rydberg atoms, was described in chapter 4. In this chapter, measurement and compensation of stray electric field inside the trap by application of a dc electric field and observing the spectral shifting of the microwave transitions between Rydberg states will be described.

In the following section, the effect of electric field on Rydberg atoms is explained. This effect will be illustrated for H and Rb atoms. In section 5.3, experimental results for measuring and compensating the stray electric field are presented. A comparison between a theoretical calculation of the effect of the electric field on Rydberg states (Stark map) and the experimental results is made in this section. The electric field distribution due to two typical cold plasma densities are estimated by the Holtsmark distribution method in section 5.4. Using this technique, the density of an expanding plasma can be diagnosed by measuring the spectral broadening of a microwave transition due to the effect of the electric field.

## 5.2 Stark Effect

The effect of an electric field on Rydberg states is known as the Stark effect which is of great practical importance for the study of Rydberg atoms.

In the presence of an electric field, Rydberg state energies are shifted; spherical symmetry is lost and $l$ ceases to be a good quantum number as the electric field mixes different $l$ states. Some parts of the following explanations are adapted from Ref. [1].

### 5.2.1 Hydrogen

It is easiest first to consider the behavior of the Hydrogen atom in a static field. The effect of electron and nuclear spins are small, thus neglected. If the applied field $E$ is in the $z$ direction, the potential seen by the electron is given by,

$$V = -\frac{1}{r} + Ez. \tag{5.1}$$

Using the zero field $nlm$ angular momentum eigenstates, the matrix elements $\langle nlm\,|Ez|\,n'l'm'\rangle$ of the Stark perturbation to the zero field Hamiltonian can be calculated. The matrix element in spherical coordinates is

$$\langle nlm\,|Ez|\,n'l'm'\rangle = E\langle nlm\,|r\cos\theta|\,n'l'm'\rangle \tag{5.2}$$

where the quantization is along the $z$ axis. The $Ez$ matrix elements are non vanishing if $m' = m$ and $l' = l \pm 1$ due to the properties of the spherical harmonic angular functions. The $E$ field lifts the degeneracy of the $lm$ states of a particular $n$ state. For all the diagonal elements, the Hamiltonian matrix has the same term, $-1/2n^2$. If the electric dipole coupling to other $n$ states is neglected, when the matrix is diagonalized all of its eigenvalues will be proportional to $E$. That means the H atom shows a linear Stark shift. Stark states having linear Stark shifts, have permanent electric dipole moments. These states have positive Stark shifts if their electron is localized on the up field side of the atom, and they have negative Stark shifts if their electron is localized on the down field side of the atom.

Therefore, for non-relativistic Hydrogen, the highly degenerate zero-field states fan out into

a "manifold" for each $m_l$, which remains a good quantum number (see Fig. 5-1). At low $E$ fields, the first order energies are [1]:

$$W = -\frac{1}{2n^2} + \frac{3}{2}E(n_1 - n_2)n \tag{5.3}$$

where $n_1$ and $n_2$ are non-negative integers labeling different members of the manifold, and are related to $|m_l|$ and $n$ by

$$n_1 + n_2 + |m_l| + 1 = n. \tag{5.4}$$

For $m_l = 0$, the extreme "blue-shifted" (up shifted) state of the manifold has $n_1 - n_2 = n - 1$, while the extreme "red-shifted" (down shifted) state has $n_1 - n_2 = -n + 1$. The energy separation between these extreme states of the manifold increases with $n$.

Figure 5-1 shows the Stark structure and field ionization of the $|m_l| = 1$ states of the H atom. The Stark shifts are quite linear, except at the highest fields shown, and the first order energies of Eq. 5.3 are adequate for many purposes. Figure 5-1 also shows that the levels of $n$ and $n + 1$ cross.

### 5.2.2 Alkali-Metal Atoms

Alkali-metal atoms, have similar characteristics to the H atom in an electric field. However, the presence of the finite sized ionic core in these atoms results in important differences. The presence of the core in zero field reduces the energies, especially those of the lowest $l$ states. With a finite sized ionic core, the wave function is no longer separable in parabolic coordinates. Hence, the parabolic quantum number $n_1$ is not a good quantum number, unlike in the H atom.

In the region below the classical ionization limit, the blue and red states of adjacent $n$ do not cross as they do in H. Since these states are coupled in alkali atoms, they exhibit avoided crossings.

An efficient method of calculating the energy levels (Stark maps) for alkali metals in Rydberg states is described by Zimmerman *et al.* [55]. Using the same method, the Stark map of Rb for high $n$ Rydberg states is calculated and illustrated in Fig. 5-2 [49].

Here the Stark effect in nonhydrogenic atoms like Rb is calculated. Ignoring the spin of the Rydberg electron, the Hamiltonian is given by [1],

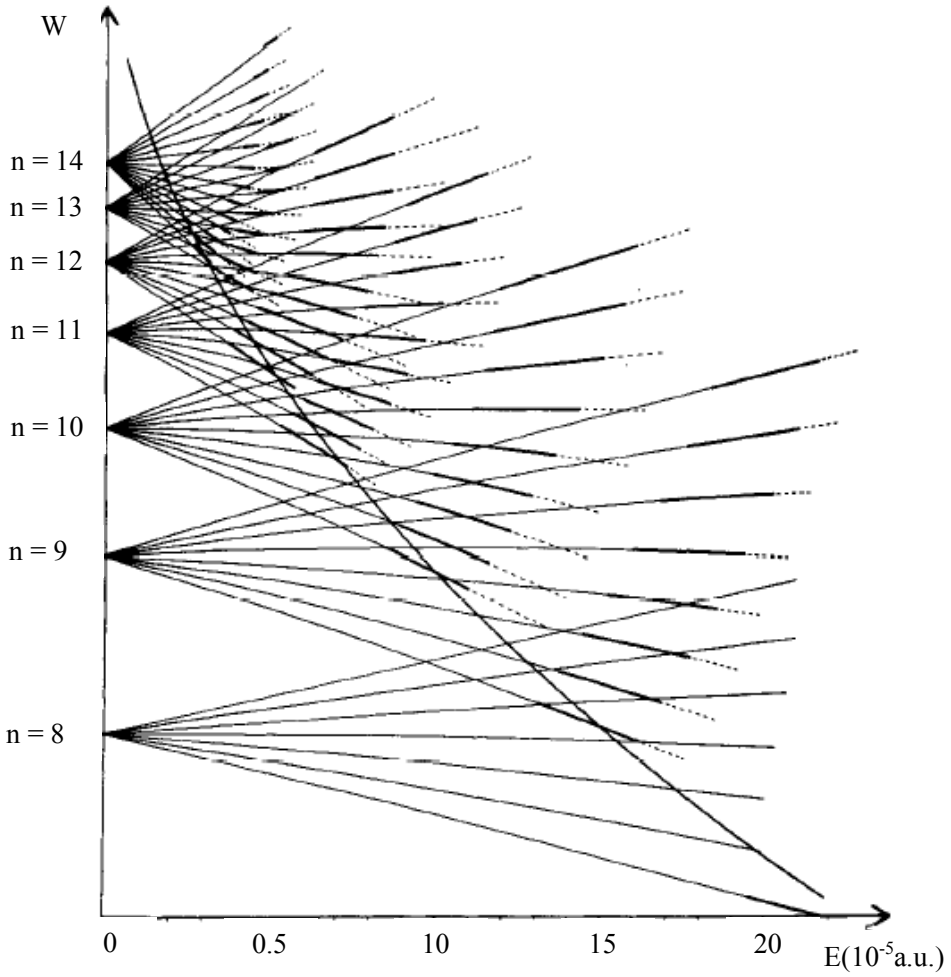


Figure 5-1: Stark structure and field ionization properties of the $|m_l| = 1$ states of the H atom. The zero field manifolds are characterized by the principal quantum number $n$ (from Ref. [54]).

$$H = -\frac{\nabla^2}{2} + \frac{1}{r} + V_d(r) + Ez \tag{5.5}$$

where $V_d(r)$ is the difference between the Rb potential and the Coulomb potential,$-1/r$ and is only nonzero near $r = 0$. A straightforward and effective method of calculating the energies and wave functions is direct diagonalization of the Hamiltonian matrix. If we use the Rb $nlm$ spherical states as basis functions, the diagonal matrix elements are given by the energies of the zero field $nlm$ states. These are well approximated by [1],

$$\langle nlm\,|H|\,nlm\rangle = \frac{1}{2(n-\delta_l)^2} \tag{5.6}$$

where $\delta_l$ is the quantum defect, and off diagonal matrix elements are given by,

$$\langle nlm\,|Ez|\,n'l \pm 1m\rangle = \delta_{m,m'}\delta_{l,l'\pm1}E\langle l, m\,|\cos\theta|\,l \pm 1, m\rangle\langle n, l\,|r|\,n', l \pm 1\rangle \tag{5.7}$$

where $\delta_{m,m'}$ and $\delta_{l,l'\pm1}$ are the selection rules,

$$\delta_{m,m'} = \left\{ \begin{array}{ll} 1, & m = m' \\ 0, & m \neq m' \end{array} \right\}$$

$$\delta_{l,l'\pm1} = \left\{ \begin{array}{ll} 1, & l = l \pm 1 \\ 0, & l \neq l \pm 1 \end{array} \right\} \tag{5.8}$$

and $\langle l, m\,|\cos\theta|\,l \pm 1, m\rangle$ is the angular matrix component derived using spherical harmonics,

$$\langle l, m\,|\cos\theta|\,l-1, m\rangle = \left(\frac{l^2-m^2}{(2l+1)(2l-1)}\right)^{1/2}$$

$$\langle l, m\,|\cos\theta|\,l+1, m\rangle = \left(\frac{(l+1)^2-m^2}{(2l+3)(2l+1)}\right)^{1/2} \tag{5.9}$$

The radial matrix component, $\langle n, l\,|r|\,n', l \pm 1\rangle$, is calculated by numerical integration. The fastest and the most accurate method of integration is Numerov's algorithm [55]. If several $n$ manifolds of $l$ states are included, the eigenvalues of the Hamiltonian matrix give the energy levels of the Rb atom in the field and the Stark maps are generated by simply connecting the

| **Atom** | $l$ | $j$ | $\delta_0$ | $\delta_2$ |
|---|---|---|---|---|
| $^{85}$Rb | 0 | 1/2 | 3.131 180 4 ($\pm 10\times 10^{-7}$) | 0.1784 ($\pm 6\times 10^{-4}$) |
| | 1 | 1/2 | 2.654 884 9 ($\pm 10\times 10^{-7}$) | 0.2900 ($\pm 6\times 10^{-4}$) |
| | 1 | 3/2 | 2.641 673 7 ($\pm 10\times 10^{-7}$) | 0.2950 ($\pm 7\times 10^{-4}$) |
| | 2 | 3/2 | 1.348 091 71 ($\pm 40\times 10^{-8}$) | -0.602 86 ($\pm 26\times 10^{-5}$) |
| | 2 | 5/2 | 1.346 465 72 ($\pm 30\times 10^{-8}$) | -0.596 00 ($\pm 18\times 10^{-5}$) |

Table 5.1: The quantum defects for s, p, and d series of $^{85}$Rb, from Ref. [8].

eigenvalues of the matrix.

In Eq. 5.6, the quantum defect, $\delta_l$, reflects how much the average potential experienced by the Rydberg electron deviates from a pure Coulombic point charge interaction. The quantum defect is strongly dependent on the orbital angular momentum quantum number, $l$, and is largest for $l = 0$. The quantum defect of an $nlj$ state is given by [1] :

$$\delta_{nlj} = \delta_0 + \frac{\delta_2}{(n-\delta_0)^2} + \frac{\delta_4}{(n-\delta_0)^4} + \frac{\delta_6}{(n-\delta_0)^6} + \frac{\delta_8}{(n-\delta_0)^8}, ..., \tag{5.10}$$

See Table 5.1 for the quantum defects of Rb for the $s$, $p$, and $d$ series. The coefficients, $\delta_4, \delta_6$, and $\delta_8$, can be found in Ref. [1]. For high $n$ states, the first two terms of Eq. 5.10 are often sufficient.

Since Stark maps can be directly compared to spectroscopic measurements, it is convenient to define the magnitude of the electric field, $E$, in $\mathrm{V\,/\,cm}$ and the energy in $\mathrm{cm}^{-1}$. The zero field energies (diagonal matrix elements) from Eq. 5.6 are calculated in atomic units and can be converted into $\mathrm{cm}^{-1}$ using the following relationship,

$$1 \text{ atomic unit (in Eq. 5.6)} = 2 \times R_{Rb}\,\mathrm{cm}^{-1} \tag{5.11}$$

where $R_{Rb} = 109736.605\,\mathrm{cm}^{-1}$ is the Rydberg constant for the Rb atom [1] (Eq. 1.2). Using the atomic unit of electric field, the off diagonal matrix elements ( Eq. 5.7) can be converted into atomic units using the following relationship [3]:

$$1 \text{ atomic unit} = 5.14220624 \times 10^9\,\mathrm{V\,/\,cm} \tag{5.12}$$

In Fig. 5-2, the Stark energy states of the Rb atom from the $n = 43$ to $n = 45$ manifolds for

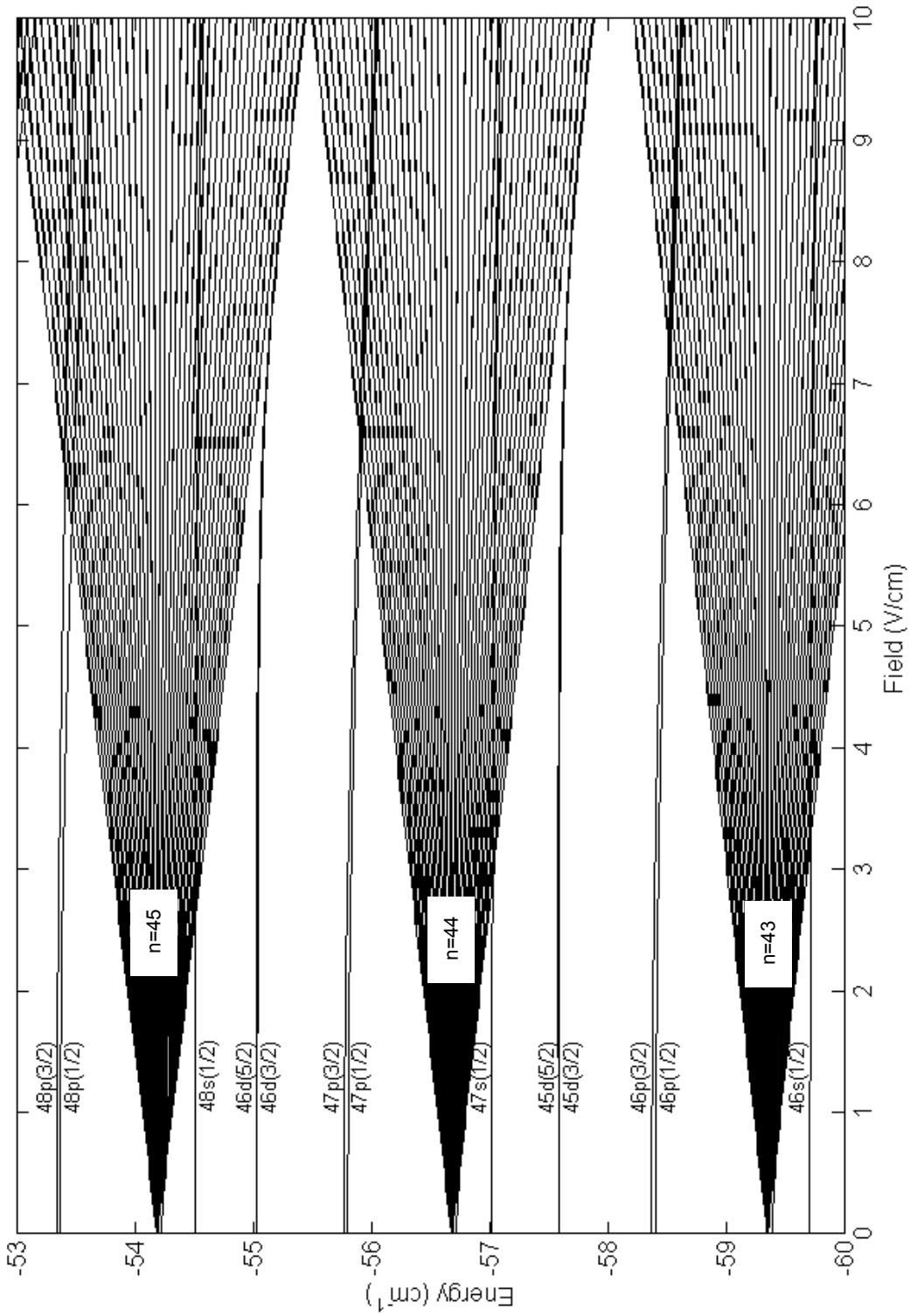


Figure 5-2: Calculated Stark structure of the $|m_j| = 1/2$ states of the Rb atom for the $n = 43$ to $n = 45$ manifolds [49].

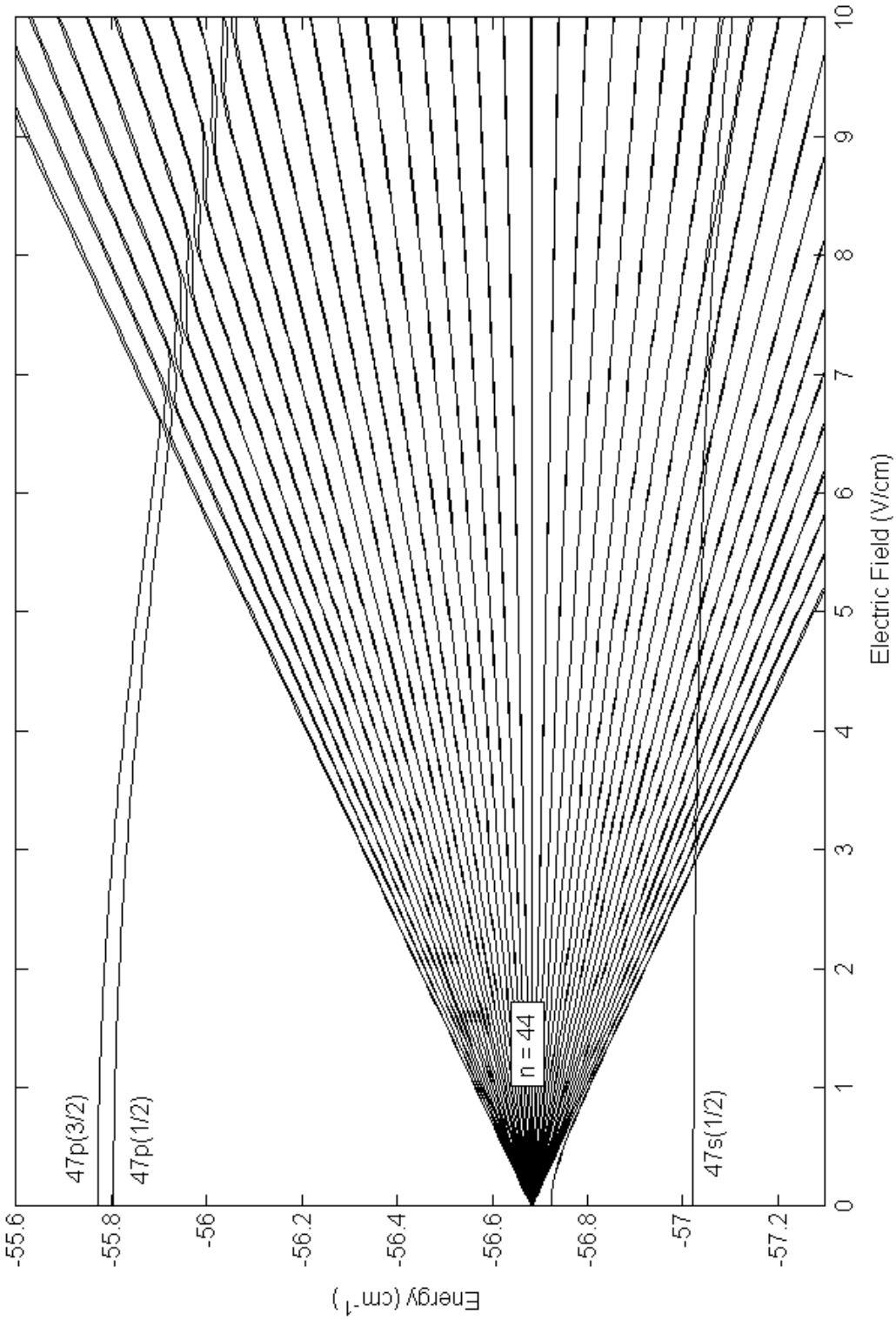


Figure 5-3: Closer look at calculated Stark structure of the $|m_j| = 1/2$ states of the Rb atom at the $n = 44$ manifold [49].

$|m_j| = 1/2$ are shown. This Stark map is obtained by direct diagonalization of the Hamiltonian matrix [49]. In zero field, the quantum defects $\delta_{s_{1/2}}$, $\delta_{p_{1/2}}$, $\delta_{p_{3/2}}$, $\delta_{d_{3/2}}$, and $\delta_{d_{5/2}}$ of the Rb states displace them ($s, p$, and $d$ states) from the high $l$ states and they only exhibit large Stark shifts when they intersect the manifold of Stark states. As shown in Fig. 5-2 and Fig. 5-3, these states undergo quadratic Stark effect at low fields. Unlike the Stark map of Hydrogen, shown in Fig. 5-1, the energy levels of different $n$ do not cross in the Rb stark map.

For a heavy alkali metal such as Rb, the fine structure interaction is large enough to influence the Stark structure and must be taken into account. The fine structures of the $p$ and $d$ states of Rb are large and can not be neglected, so that $|m_j|$ rather than $|m_l|$ is the "good " quantum number. Each $|m_j|$ manifold is a mixture of states with $m_l = m_j \pm \frac{1}{2}$. As illustrated in Figs. 5-2 and 5-3, the fine structure interaction has been implemented into the Stark calculation [49]. The Stark shifts of the fine structure of $p$ and $d$ states are apparent in these figures. In Fig. 5-3, the $47p_{1/2}$ and $47p_{3/2}$ states have quadratic Stark shifts until they intersect the $n = 44$ manifold.

Since high $l$, ($l > 3$), states have negligible quantum defects at zero field, they fan out into a "manifold" for each $m_l$. These states have hydrogenic Stark shifts, as illustrated in Fig. 5-3 for the $n = 44$ manifold.

In order to minimize the stray electric field and eventually measure a plasma density, the shifting of the transitions between $47s_{1/2} \longrightarrow 47p_{1/2}$ due to the presence of an $E$ field are experimentally observed. The theoretical calculation of the Stark map is very helpful to estimate the shifting and broadening of the transitions due to stray and applied $E$ fields.

Figure 5-4 is a schematic diagram showing the field dependence of the energy levels of Rydberg states undergoing quadratic Stark shifts. In this figure the inhomogeneous electric field distribution is shown by two vertical dashed lines on both sides of the central field with values $E_1$ and $E_2$. Due to the field inhomogeneity, the Rydberg states are subject to slightly different electric fields. On the right side of the graph, the line broadening for Rydberg states due to the electric field distributions, are presented. The line broadening for the Rydberg states depends on the strength of the electric field distribution due to the parabolic character of the quadratic Stark shifts. This means that the line broadening that results from the same inhomogeneous electric field distribution increases as the average electric field increases.

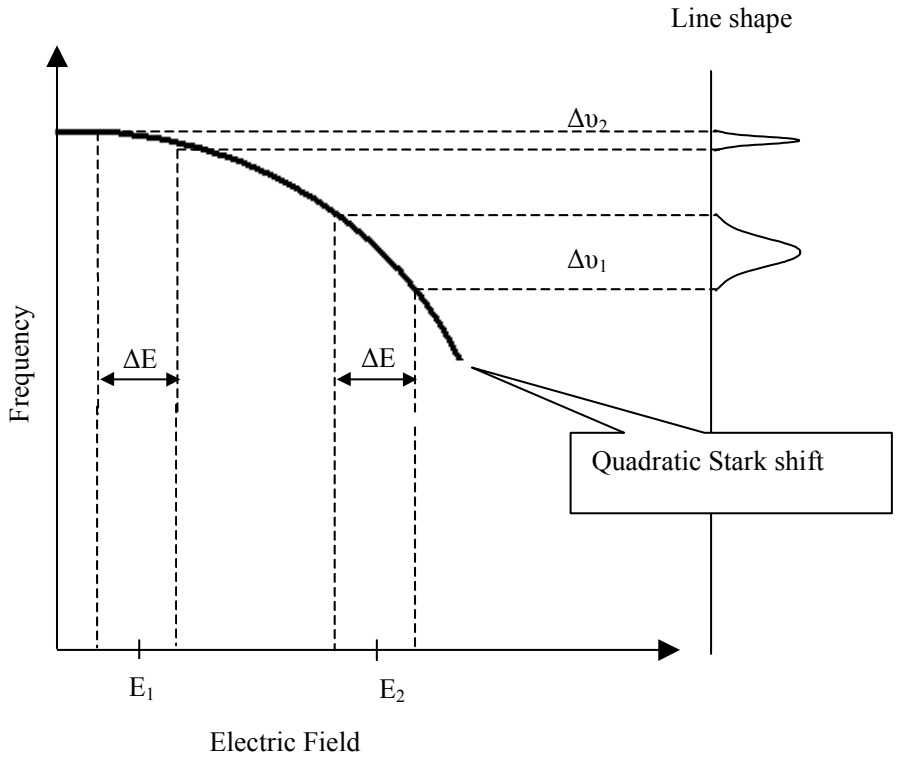


Figure 5-4: Schematic diagram showing the dependence of the energy levels of Rydberg states to the applied electric field. The quadratic Stark effect and its relative line shapes are shown as a function of the electric field distribution around the central fields $E_1$ and $E_2$ ( after Ref. [56]).

## 5.3 Experimental

High resolution spectra of high Rydberg states can be modified by electric fields. Even weak dc electric fields strongly modify the spectra. Stray fields may be precisely measured and compensated due to the strong dependence of the spectral features on the electric fields. Almost field-free conditions can be achieved, which are required to obtain resolved spectroscopic information from the highest Rydberg states. This section demonstrates the measurement and the compensation of stray electric field, by observing the line shifting of the microwave transitions between the $47s_{1/2}$ and $47p_{1/2}$ states of Rb due to a varying dc $E$ field.

The AHC's current is turned off 3 ms before the flash lamps of the YAG laser fire, and is turned back on 0.5 ms after, to optimize the spectroscopic resolution. Microwave transitions are monitored by SFI. Following each laser pulse, a voltage ramp is applied to the lower electric field plate and ions resulting from ionization of the Rydberg atoms are detected by a MCP.

Stray $E$ field can be compensated in two perpendicular directions in this apparatus. One direction is along the perpendicular axis to the plane of the electric field plates (axis $x$ in Fig. 2-6). The other direction is along the axis of the AHC (axis $z$ in Fig. 2-6). As explained is Sec. 2.9.2, a dc voltage is applied to the electric field plates. The top plate is connected to the AWG which is used as a GPIB controllable variable power supply. The bottom plate is connected to the slowly rising FIP circuit, which allows a dc bias voltage to be applied to the plate prior to the HV pulse. This voltage is controlled using a digital to analogue output of a data acquisition board.

A grounded flange of the vacuum chamber is on one side of the plates. There is an insulating fused silica window on the other side of the plates (Fig. 5-5). Therefore, changing the average voltage of the electric field plates induces an electric field in the $z$ direction towards the grounded flange of the vacuum chamber that is connected to the plates by four ceramic insulators. However, the magnitude of this effect is difficult to estimate. For compensating the stray field in $x$ direction it is possible to change the differential voltage of the two plates. Changing the differential voltages of the plates results in an applied $E$ field in the $x$ direction that can be estimated by,

$$E = \frac{\Delta V}{d} \tag{5.13}$$

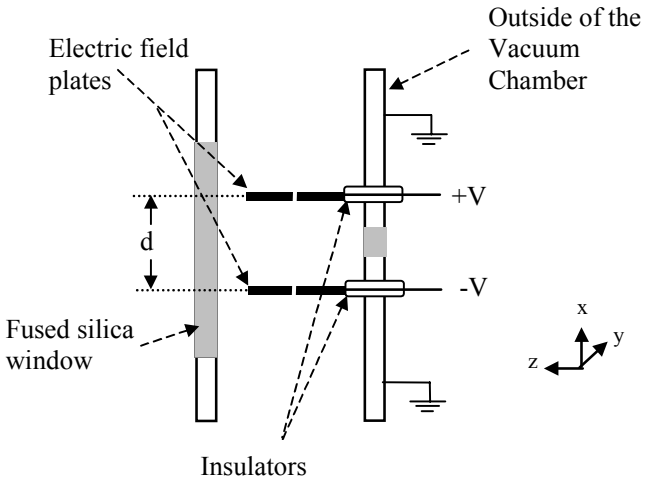


Figure 5-5: Schematic diagram of the connections for the electric field plates. They are near a grounded flange on one side and there is an insulating fused silica window on the other side. The separation of the plates is $d = 3.556\,\mathrm{cm}$.

where $d = 3.556\,\mathrm{cm}$ is the separation between the plates and $\Delta V$ is the potential difference across them. A Labview program sets the differential and average voltages of the plates.

This experiment was performed in three steps:

1) In the first step, the attempt was to compensate the $E$ field in the $x$ direction by varying the differential voltage between the two plates. The average voltage was set to $2.4\,\mathrm{V}$ and the differential voltages of , $-0.2, 0.1, 0.4, 0.7$, and $1\ \mathrm{V}$ were applied to the plates. This resulted in estimated electric fields of $-0.056, 0.028, 0.112$, and $0.281\,\mathrm{V/cm}$ respectively. Figure 5-6 shows the effect of dc electric field on the $47s_{1/2} \rightarrow 47p_{1/2}$ transitions in Rb for different differential voltages across the plates.

As explained in section 4.4.1, the $47s_{1/2} \rightarrow 47p_{1/2}$ transitions splits into 4 components due to the Zeeman effect. They also undergo a quadratic Stark shift (see Fig.5-3) due to the applied $E$ field. The Stark shifts in this case, are proportional to the square of the magnitude of the electric field, but do not depend on its sign. Therefore, the line centers of the components lie on a parabolic curve of the form shown in Fig. 5-7.

Figure 5-7 illustrates the line center of one of the microwave components of each spectra, shown by an arrow in Fig. 5-6, as a function of the applied field. The maximum point of the

parabola indicates for the minimum $E$ field. The minimum $E$ field is achieved with an average voltage of 2.4 V and a differential voltage of 0.2944 V .

2) The same procedure is used to determine and cancel the stray field component in the orthogonal direction, $z$, by keeping the differential voltage equal to 0.2944 V and changing the average voltage. The average voltages of $-7, -4, 2.4, 5$ and 7 V were applied to the plate. Figure 5-8 shows the effect of changing the average voltages on the $47s_{1/2} \rightarrow 47p_{1/2}$ transitions with differential voltage set at 0.2944 V. Figure 5-9 shows the center line frequency of the marked transitions in Fig. 5-8 as a function of the applied $E$ field. In this case, the minimum field is obtained using an average voltage of 2.685 V and a differential voltage of 0.2944 V .

3) Finally, in third step of this experiment, step 1 is repeated but this time the average voltage is set to 2.685 V and the differential voltage is varied. The differential voltages of $0.0, 0.1, 0.5$ and 0.75 V were applied to the plates resulting in applied electric fields of $0.0, 0.028, 0.14$ and 0.22 V / cm. Figure 5-10 shows the effect of changing the differential voltages on the $47s_{1/2} \rightarrow 47p_{1/2}$ transitions with the average voltage set at 2.685 V. Figure 5-11 shows the center line frequency of the marked transitions in Fig. 5-10 as a function of the relative $E$ field. The minimum electric field is attainable with the average voltage of 2.685 V and differential voltage of 0.312 V, as shown in Fig. 5-11.

Steps 1 to 3 are an iterative procedure that can be repeated indefinitely to get to a point where the stray $E$ field is minimized. Sources of the measured stray field in the apparatus are as follows,

- The voltage of 1300 V applied to the MCP detector at the top of the electric field plates, which leaks into the photoexcitation region.
- The pulsed voltage of $\sim 320$ V (resulting in a pulsed electric field of 89.99 V / cm, see Fig. 3-3) applied on the electric field plates to field ionize the $47p_{1/2}$ Rydberg states. This voltage may not return to zero in the interval separating subsequent pulses.
- The Rb getter, which is being resistively heated by applying 10.5 A current, is in a direction perpendicular to $x$ and $z$ direction ($y$ direction in Fig. 2-6).

The stray field in the $y$ direction can not be compensated by changing either the differential voltage or changing the average voltage of the electric field plates. However, by comparing the

calculated Stark maps and the experimental observations, it will be shown that the field in this direction is negligible.

In Fig. 5-12, theoretical data from the calculated Stark maps and the experimental observation of the $47s_{1/2} \rightarrow 47p_{1/2}$ resonance frequency as a function of the applied $E$ field are illustrated. In the theoretical calculation, the only perturbation considered on the energy levels is due to the applied electric field. However in the experimental observations the magnetic field inside the trap (see chapter 3) Zeeman shifts the energy levels as well. As shown in Fig. 5-12, there is a shift equal to 1.765 MHz at zero field between the theoretical and the experimental graphs. This shift is mainly due to the presence of the magnetic field. As explained in Sec. 4.2, for a set of states with particular values of $n, L$, and $J$, the individual states with different $M_J$ will be equally spaced in energy, separated by $g_J \mu_B B$ (Fig. 4-1). Thus, the zero magnetic field transition frequency for each spectra can be calculated by considering the average frequency of the four microwave transitions, as shown in Fig. 5-10.

This can be used to adjust the experimental data and plot a graph showing the zero magnetic field transition frequency as a function of the applied electric field. In Fig. 5-12, the experimental data have been shifted up in frequency after being adjusted for Zeeman shifts.

Now the theoretical data can be compared to the adjusted experimental data. They almost overlap each other at zero electric field. However, there is a small vertical shift equal to 0.36 kHz between the two graphs. This offset could be due to the quantum defect uncertainties which appear in the theoretical calculations. The absolute uncertainty of the transition frequency at zero field can be calculated to be $\pm 27$ kHz using the uncertainties from Table. 5.1.

The stray field in the $y$ direction adds an additional electric field to the applied $E$ field and it is expected to see a blue shift (lower frequency) in transition frequency. However as shown in Fig. 5-12 the transitions are not blue shifted (the adjusted data), which means that the effect of the stray field in the $y$ direction due to the current running through the Rb getter is so small that can be neglected.

Furthermore, the present inconsistency between the theoretical data and the adjusted experimental data at "non zero fields" can be due to the following approximations: In calculating the electric field between the two electric field plates it is assumed that there is an ideal homogeneous electric field between two "infinite" plates using Eq. 5.13, which is an approximation.

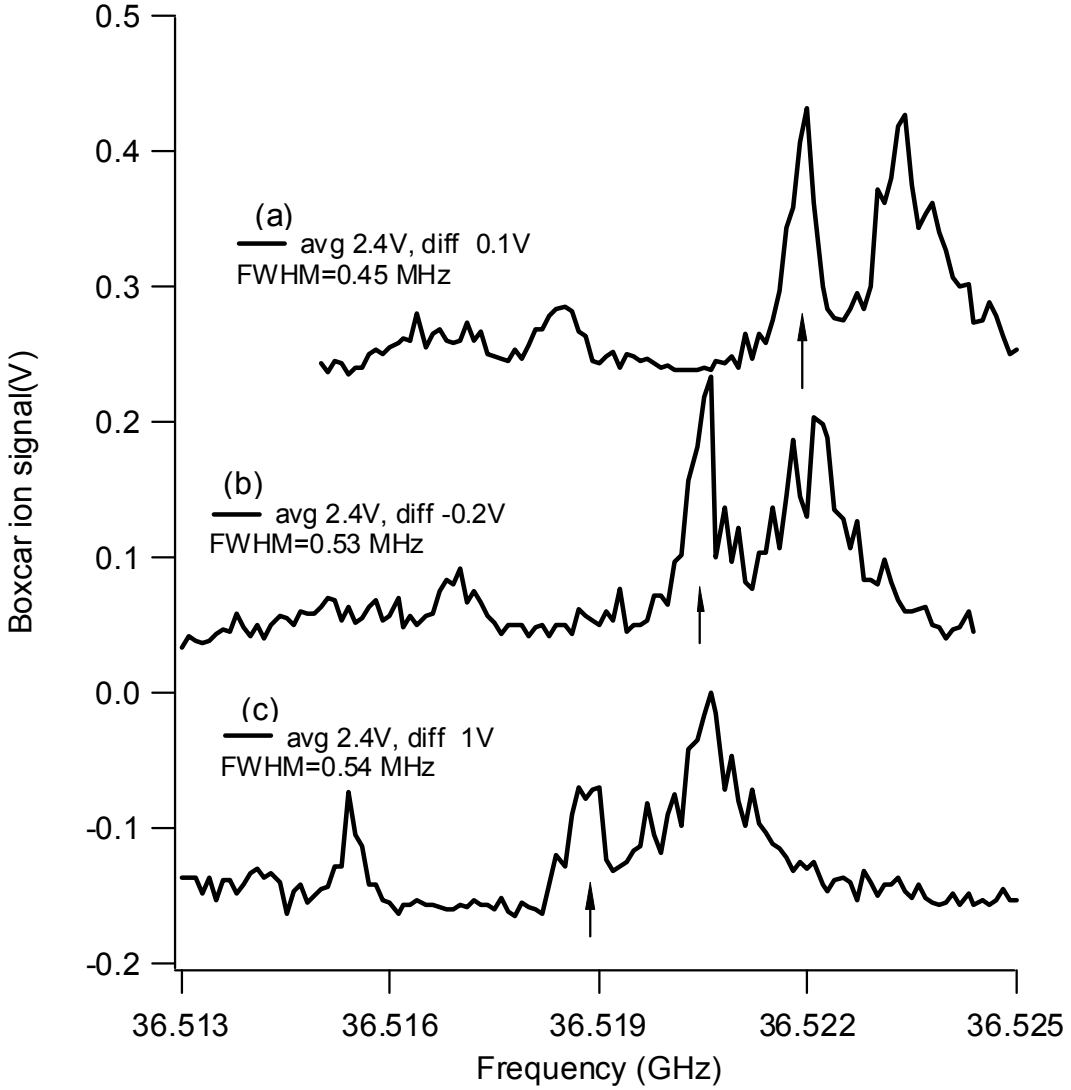


Figure 5-6: Stark shifts of the microwave transitions $47s_{1/2} \rightarrow 47p_{1/2}$ in Rb. To record these traces differential voltages of $-0.2, 0.1, 0.4, 0.7$, and $1\,\mathrm{V}$ were applied to the plates, resulting in applied electric fields of $-0.056, 0.028, 0.112$, and $0.281\,\mathrm{V/cm}$. Only three out of the five spectra are shown in this figure. For clarity, trace (a) and trace (c) have a vertical offset of $0.2\,\mathrm{V}$ and $-0.2\,\mathrm{V}$ respectively.

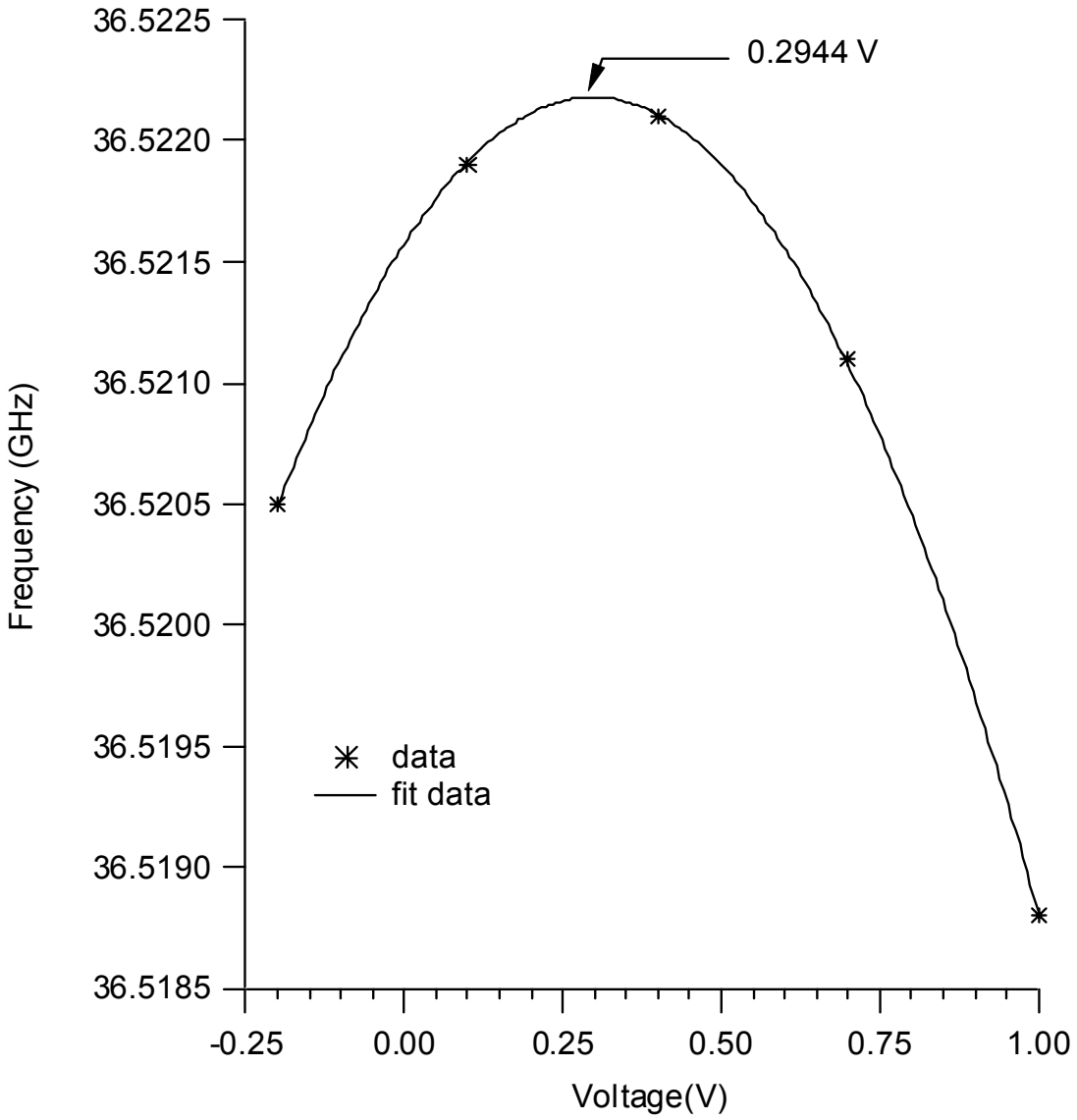


Figure 5-7: Microwave transition $47s_{1/2} \rightarrow 47p_{1/2}$ of Rb as a function of applied electric field. Apparent from the figure is the quadratic Stark shift of the $47s_{1/2}$ and $47p_{1/2}$ energy levels. To compensate the stray field in $x$ direction different differential voltages were applied to the electric field plates. The vertex of the parabola (average 2.4 V, differential 0.2944 V) represents the minimum electric field.

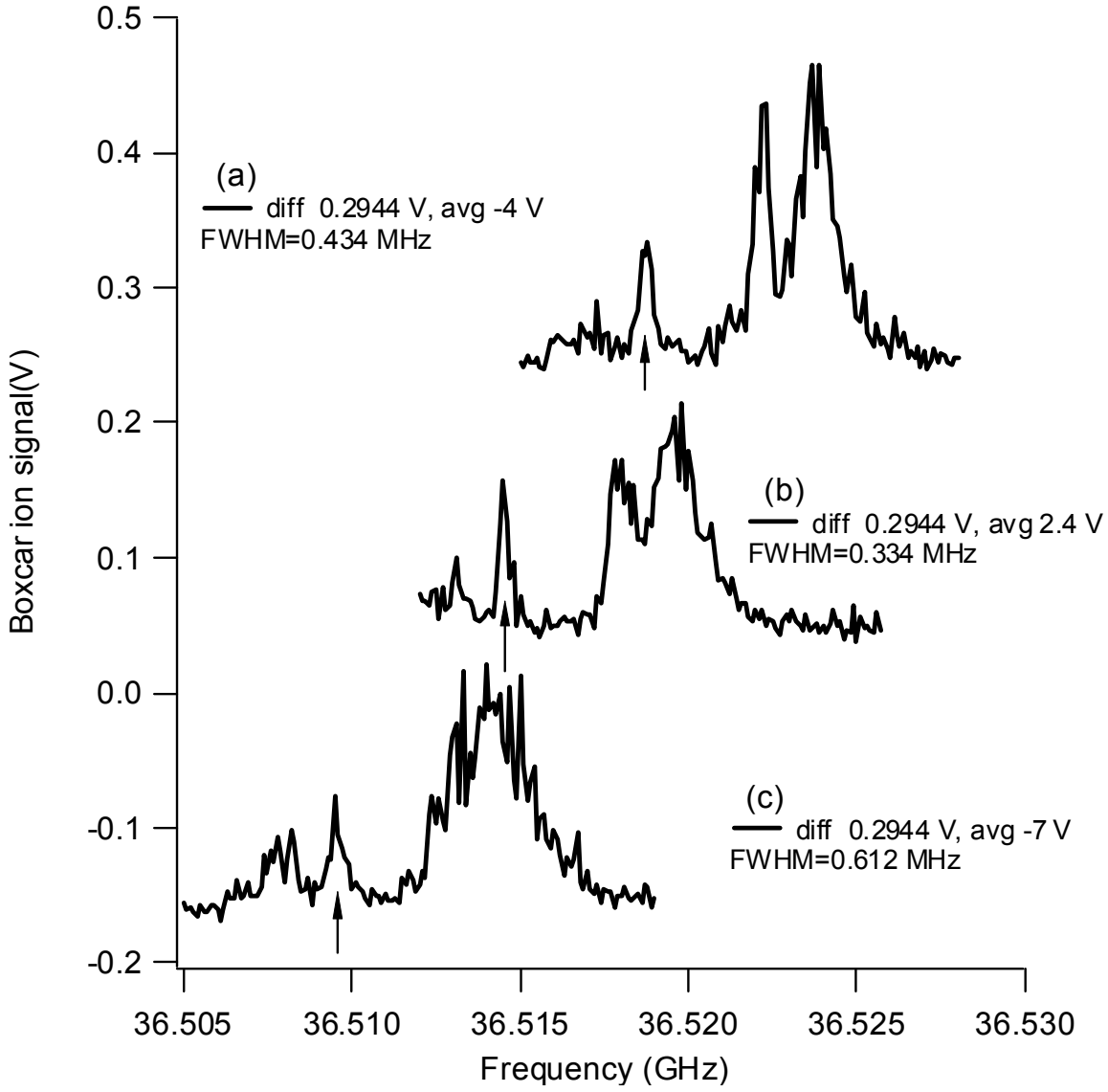


Figure 5-8: Changing the average voltage of the electric field plates and its effect on the $47s_{1/2} \rightarrow 47p_{1/2}$ transition in Rb. To record these traces, average voltages of $-7, -4, 2.4, 5$, and $7\,\mathrm{V}$ were applied to the plates. For clarity, trace (a) and (b) have a vertical offset of $0.2\,\mathrm{V}$ with respect to the adjacent trace.

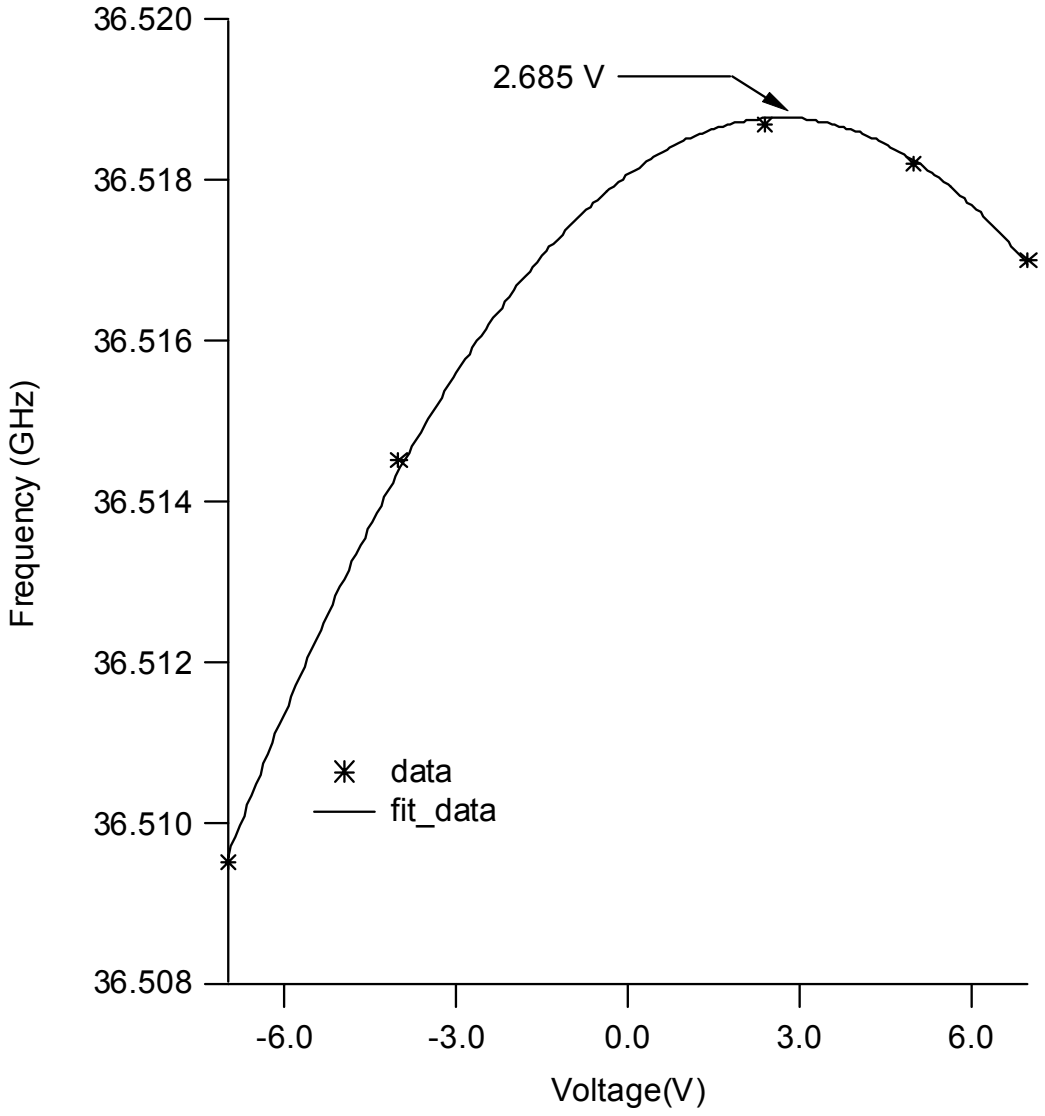


Figure 5-9: Plot of the electric field dependence of the transitions by changing the average voltage of the plates and therefore compensating the stray field in $z$ direction. The vertex of the parabola (average 2.685 V, differential 0.2944 V) represents the minimum electric field.

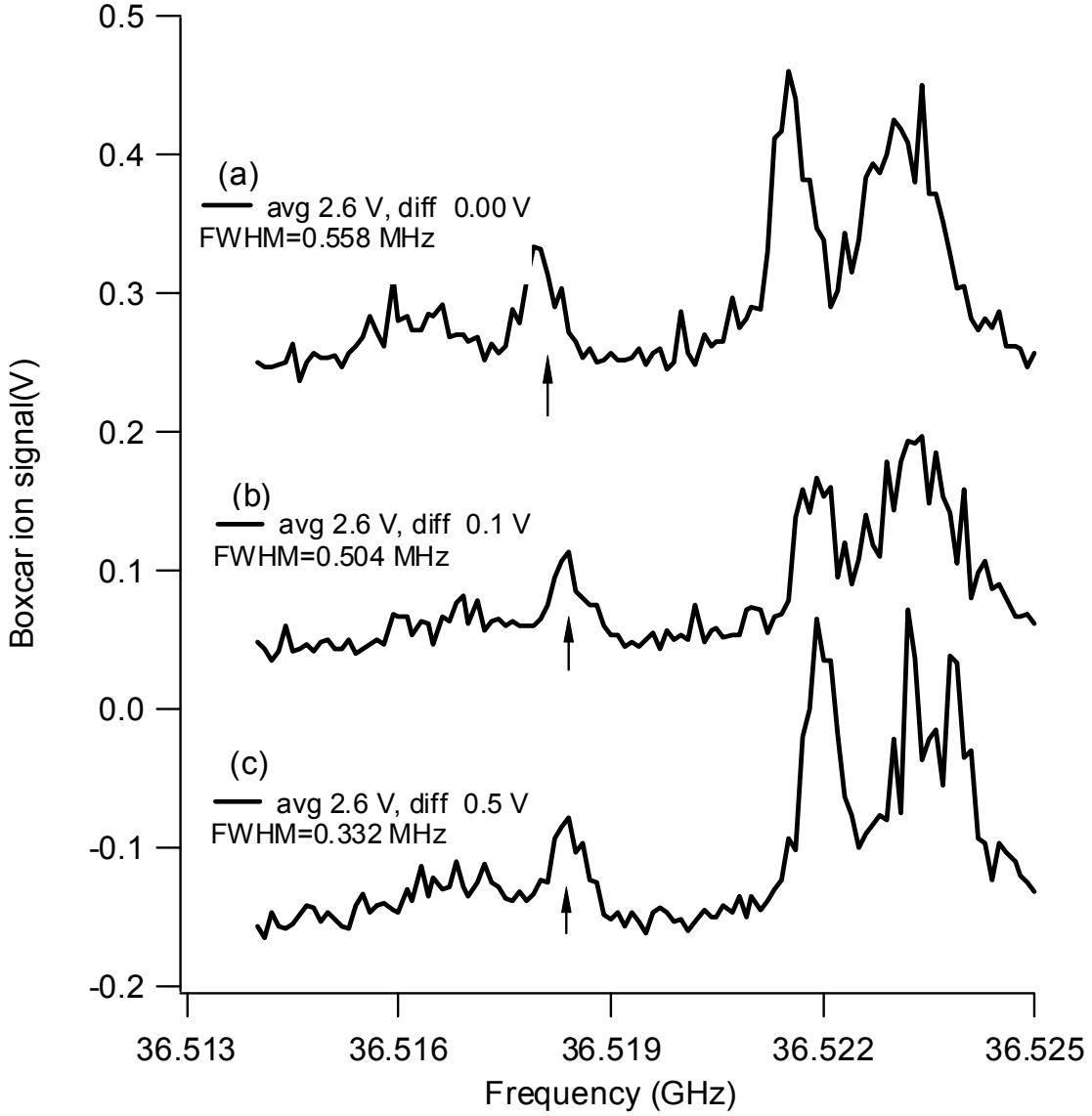


Figure 5-10: Effect of changing differential voltages of the electric field plates on the $47s_{1/2} \longrightarrow 47p_{1/2}$ transition in Rb. Differential voltages of $0.0, 0.1, 0.5$, and $0.75\,\mathrm{V}$ were applied to the plates resulting in applied electric field of $0.0, 0.028, 0.14$, and $0.22\,\mathrm{V/cm}$. Trace (a) and (b) have $0.2\,\mathrm{V}$ vertical offset with respect to the adjacent trace.

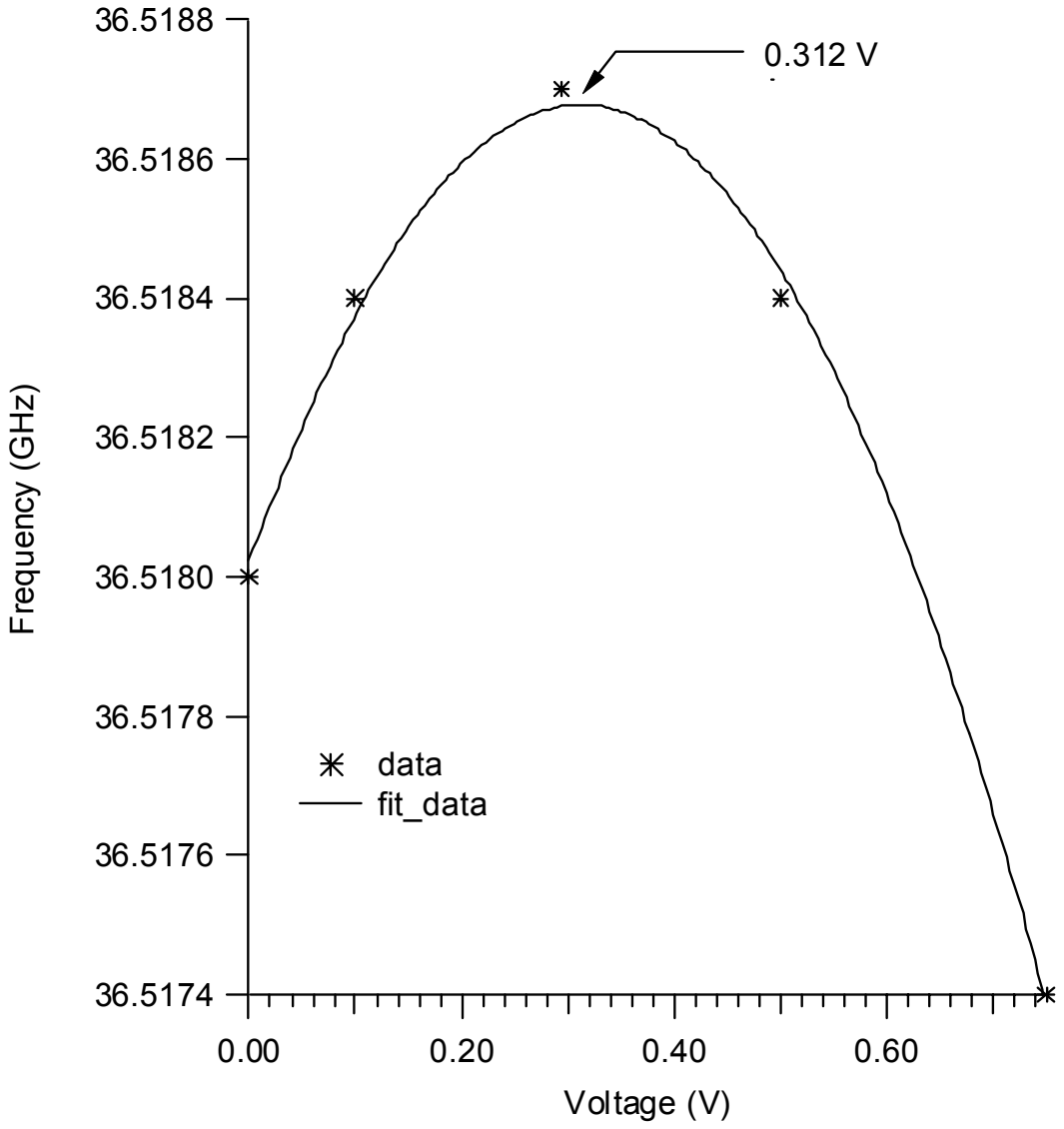


Figure 5-11: Changing the differential voltage of the plates and its effect on $47s_{1/2} \longrightarrow 47p_{1/2}$ transition in Rb. Apparent from the figure is the quadratic Stark shift of the energy levels. The vertex of the parabola (average 2.685 V, differential 0.312 V) represents the minimum electric field.

It was also assumed that only $E_x \neq 0$.

## 5.4 Holtsmark Distribution of Electric Field in an Ultra-Cold Neutral Plasma (UCNP)

The electric field distribution of a UCNP can be studied using Rydberg-atom spectroscopy. As shown in the previous sections, highly excited Rydberg atoms are very sensitive to static and ac electric fields and can be used for the measurement of plasma induced electric fields.

In a plasma, the electric field typically follows a probability distribution centered about a most probable electric field. In this section, a technique to estimate the density of a UCNP using the Holtsmark distribution of electric fields will be described. A model showing the distribution of the electric field in a typical plasma gives information about the Rydberg states that should be excited in order to measure the electric field by mm-wave spectroscopy (Fig. 5-4).

Holtsmark theory is one of the most successful theories of line broadening by the particles of a plasma [57], [58]. The main idea used to derive the Holtsmark distribution is that, the charged particle positions are assumed to be completely uncorrelated. In our case, this means that ions are assumed to be randomly placed right after the creation of the plasma by photoionization. This field of randomly placed ions determines the ion microfield (see Sec. 1.3).

The Holtsmark distribution function $P(\beta)$, $\beta = E/E_0$, can be obtained by plotting

$$\frac{1}{E_0} H(\frac{E}{E_0}) \tag{5.14}$$

as a function of the electric field, $E$, where $H(\beta)$ is presented by [58],

$$H(\beta) = \frac{2}{\pi\beta} \int_0^\infty \exp(-(\frac{x}{\beta})^{3/2}) x \sin(x) dx \tag{5.15}$$

and $E_0$ is defined as,

$$E_0 = \frac{q}{4\pi\epsilon_0} \frac{1}{r_0^2} \tag{5.16}$$

where $q = 1.602177 \times 10^{-19}\,\mathrm{C}$ is the electron charge and $\epsilon_0 = 8.854187817 \times 10^{-12}\,\mathrm{C}/(\mathrm{V}\,.\,\mathrm{m})$ represents the permittivity of vacuum. The term $r_0$ is the radius of a sphere whose volume is

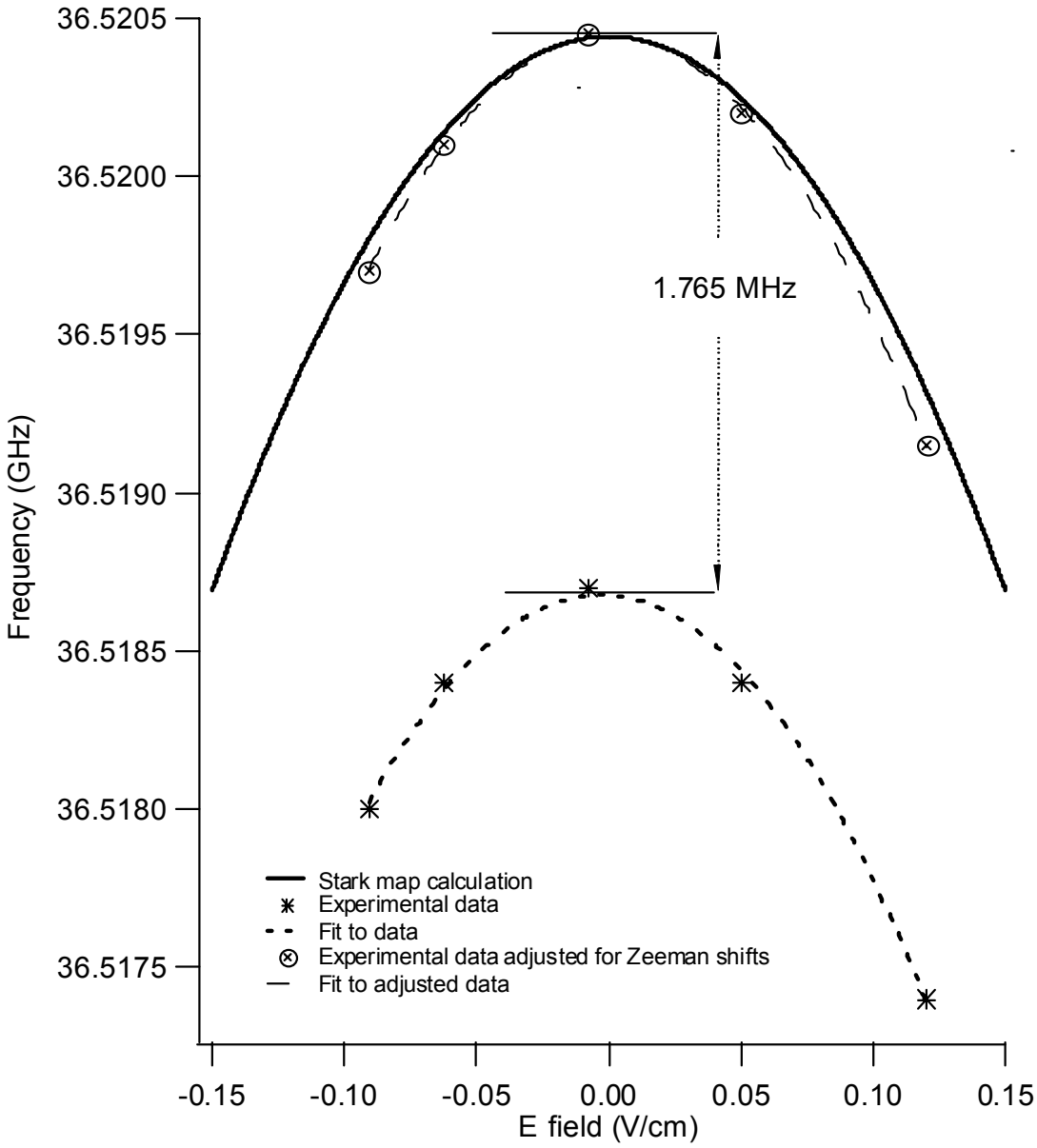


Figure 5-12: Comparison between the Stark map calculation [49] and experimental observations of the $47s_{1/2} \rightarrow 47p_{1/2}$ resonance frequency as a function of the applied $E$ field. The data have been offset by $-0.0855\,\mathrm{V}\,/\,\mathrm{cm}$ in the $x$ direction so that their maxima are at zero field.

equal to the mean volume per ion in a plasma and can be calculated using,

$$r_0 = (\frac{3}{4\pi}\frac{1}{n_p})^{1/3} \tag{5.17}$$

where $n_p$ is the plasma number density.

One of the objectives for studying the frequency broadening of the cold Rydberg states is to use it as a tool for estimating the density of a UCNP.

Assume a typical cold plasma density, produced by photoionizing laser-cooled atoms, equal to $4 \times 10^9\,\mathrm{cm}^{-3}$[10]. Using Eqs. 5.14, 5.15, 5.16, and 5.17, the Holtsmark distribution of the inhomogeneous $E$ field induced by the plasma of this density is plotted in Fig. 5-13.

Recall that in Fig. 5-12, a line fit to the experimental data yields a relationship between transition frequency of $47s_{1/2}$ to $47p_{1/2}$ as a function of the applied $E$ field,

$$\nu_{47_s \to 47_p} = 36.519 - 0.089E^2 \tag{5.18}$$

where $\nu_{47_s \to 47_p}$ represents the transition frequency in GHz and $E$, the applied electric field, is in $\mathrm{V}/\mathrm{cm}$. Using the transformation Jacobian, $|d\nu/dE|$, the frequency broadening of the transition can be obtained by,

$$P(\nu) = P(\beta)\frac{1}{|\frac{d\nu}{dE}|} \tag{5.19}$$

where $P(\nu)$ is the probability of frequency distribution due to inhomogeneous electric field distribution inside the plasma, and $P(\beta)$ represents the Holtsmark distribution function. Figure 5-14 shows the frequency distribution of the transition due to the inhomogeneous electric field induced by a plasma of density $n_p = 4 \times 10^9\,\mathrm{cm}^{-3}$.

As mentioned in section 5.2.1, the energy separation between the extreme states of a manifold increases with $n$ (Eq. 5.3). In other words as $n$ increases, the manifolds fan out more and there are larger Stark shifts (Fig.5.2). Hence, low $l$ states such as $p_{1/2}$, $p_{3/2}$, $d_{3/2}$ and $d_{5/2}$ intersect the manifolds at lower electric fields. To measure the electric field distribution in a UCNP, it is easier to work in a region where these states have not intersected the manifold. Otherwise, for a specific $E$ field more than one frequency resonance may be presented (for example, see Fig. 5-3 for microwave transition between $47s_{1/2}$ and $47p_{1/2}$). This makes it more complicated

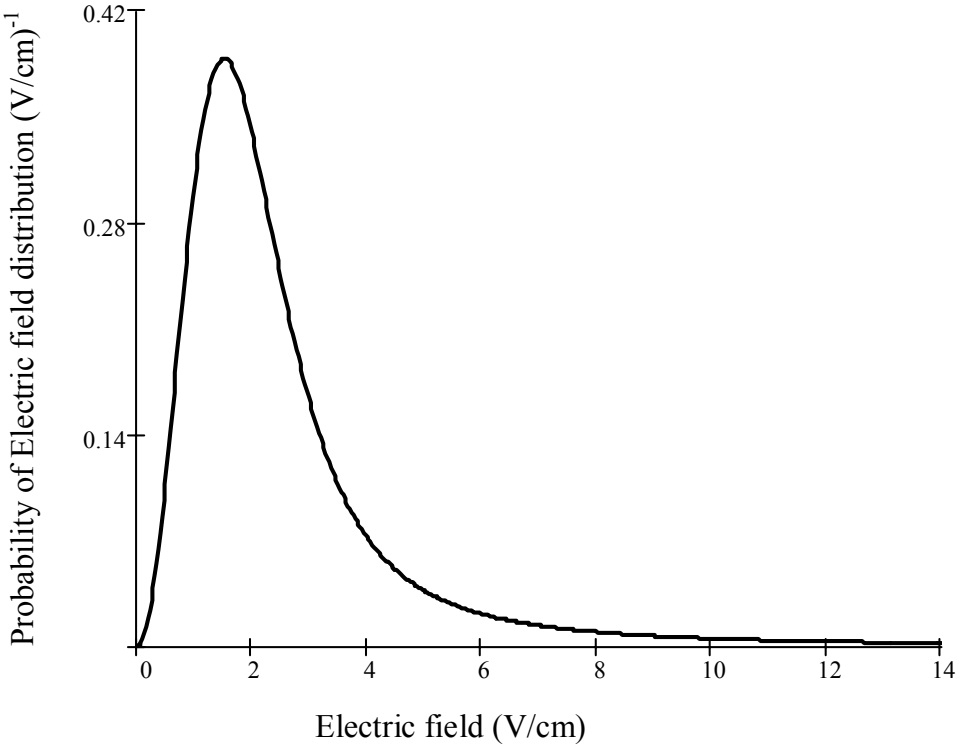


Figure 5-13: Theoretical calculation of the Holtsmark electric field distribution probability for a plasma with density $n_p = 4 \times 10^9\,\mathrm{cm}^{-3}$ .

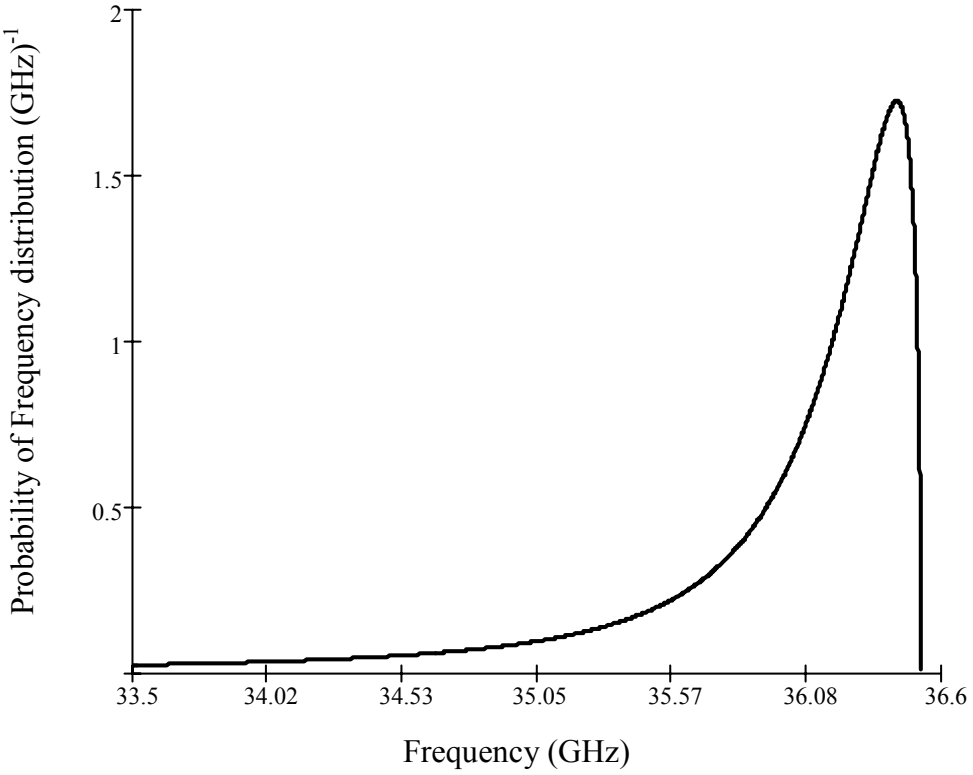


Figure 5-14: The probability of frequency distribution of the microwave transition $47s_{1/2}$ to $47p_{1/2}$ due to the inhomogeneous electric field induced by a plasma with density $n_p = 4 \times 10^9\,\mathrm{cm}^{-3}$.

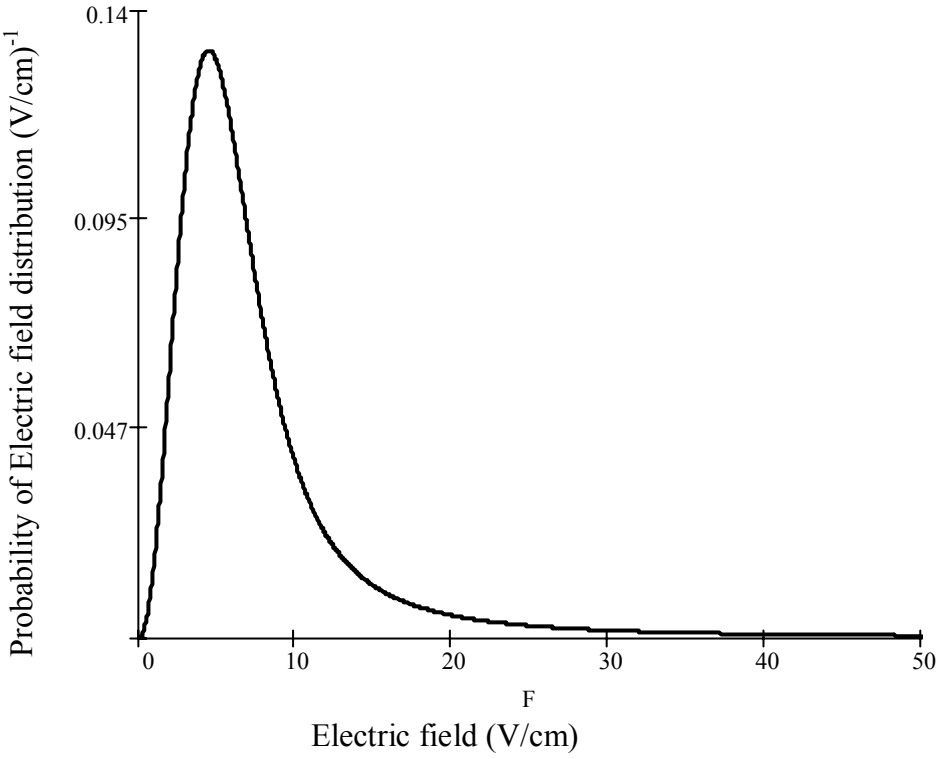


Figure 5-15: Holtsmark electric field distribution probability for a plasma with density $n_p = 2 \times 10^{10}\,\mathrm{cm}^{-3}$.

to determine the inhomogeneous electric field inside the plasma using line broadening.

In what follows it is useful to define an effective maximum field for the Holtsmark distribution. The field $E_{max}$ is the field for which 94.4% of the fields are less than. It is given by,

$$E_{max}(n_p) = 7.436\ E_0(n_p). \tag{5.20}$$

For a plasma density of $n_p = 4 \times 10^9\,\mathrm{cm}^{-3}$, the maximum electric field $E_{max}(n_p)$ is $\sim 7\,\mathrm{V/cm}$. Now recall Fig 5-3; for the $n = 44$ manifold, the maximum electric field that can be applied without having the low $l$ state ($47p_{1/2}$) intersect with the manifold, is approximately $7\,\mathrm{V/cm}$. Hence, to measure the electric field induced by this specific plasma density the $47s_{1/2} \rightarrow 47p_{1/2}$ transition can be used.

Another UCNP obtained experimentally has a density, $n_p = 2 \times 10^{10}\,\mathrm{cm}^{-3}$ [20]. Figure 5-15

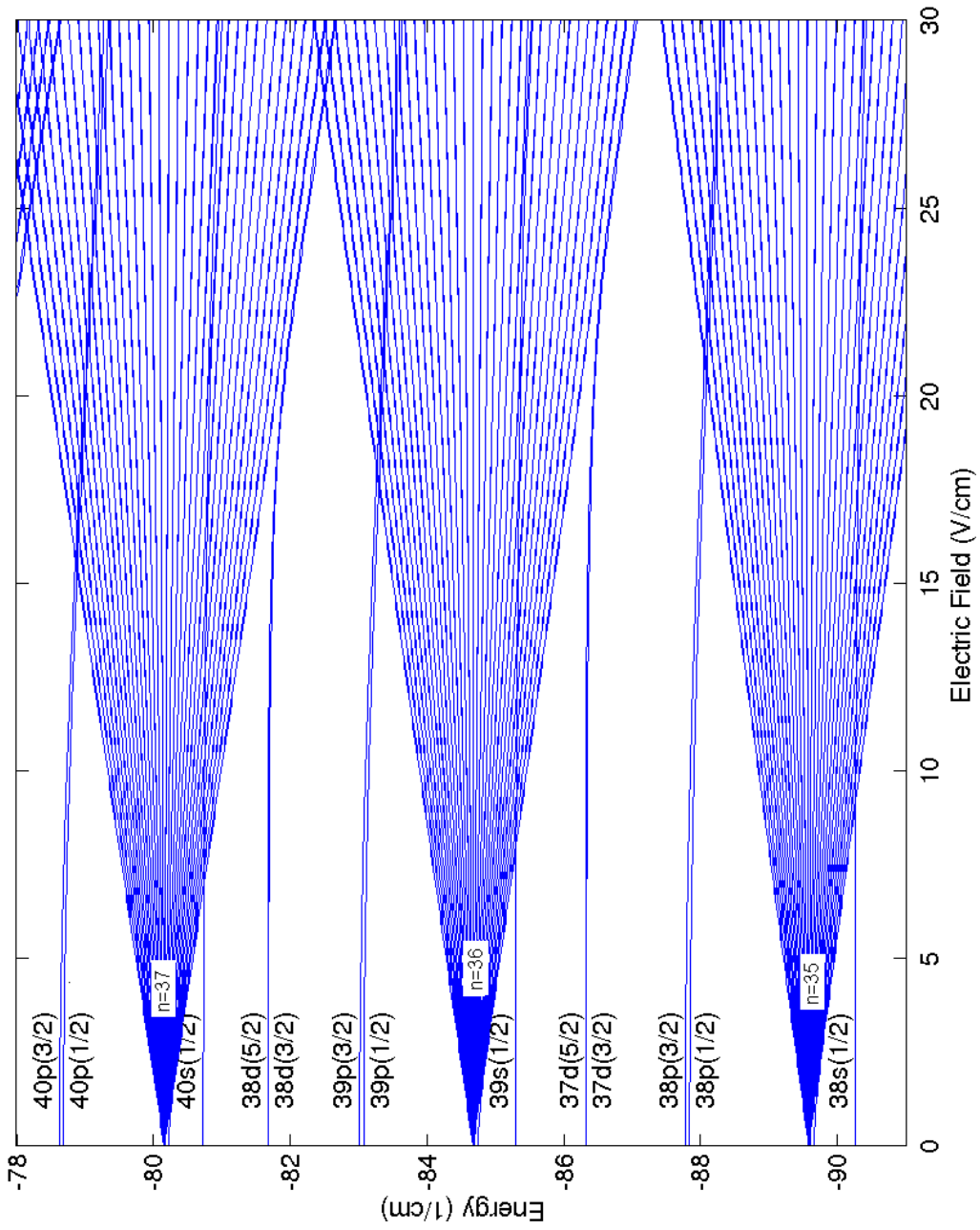


Figure 5-16: Calculated Stark maps of the $|m_j| = 1/2$ states of $^{85}$Rb for the $n = 35$ to $n = 37$ manifolds [49].

shows the theoretical Holtsmark electric field distribution of this plasma. In this case $E_{max}(n_p)$ is $\sim 20.5\,\mathrm{V\,/\,cm}$. This field can not be measured using the $47s_{1/2} \rightarrow 47p_{1/2}$ transitions, since an electric field less than $7\,\mathrm{V\,/\,cm}$ is sufficient to make the low $l$ state, $47p_{1/2}$, intersect with the manifold $n = 44$. Thus, a lower $n$ state must be chosen to satisfy the requirement for measuring the electric field distribution.

Figure 5-16 shows the calculated Stark map for the manifolds $n = 35$ to $n = 37$. In this figure, the $38p_{1/2}$ state intersects the manifold $n = 35$ in the presence of an electric field equal to $20.5\,\mathrm{V\,/\,cm}$. Thus, microwave transitions between the $38s_{1/2}$ and $38p_{1/2}$ states are suitable to study the electric field distribution of a plasma with density $n_p \leq 2\times10^{10}\,\mathrm{cm^{-3}}$. The transition frequency of the $38s_{1/2} \longrightarrow 38p_{1/2}$ resonance is $72.43\,\mathrm{GHz}$ and can be calculated by [8],

$$\Delta\nu_{n_s\rightarrow n_p} = R_{Rb}c\left[\frac{1}{(n-\delta_p)^2} - \frac{1}{(n-\delta_s)^2}\right] \tag{5.21}$$

where $R_{Rb}$ is the Rydberg constant for Rb (Eq. 1.2), $c$ is the speed of light, and $\delta_p$ and $\delta_s$ are the quantum defects of the $38p_{1/2}$ and $38s_{1/2}$ states.

If a certain plasma density, $n_p$, is given, the maximum observable electric field, $E_{max}(n_p)$, can be obtained from Eq. 5.20, in which $E_0(n_p)$ is a function of $n_p$ defined by Eqs. 5.16 and 5.17. Equation 5.20 can be rewritten as,

$$E_{max}(n_p)(\mathrm{V\,/\,m}) = 1.726\times10^{-8}(\mathrm{V\,.\,m})\times n_p^{2/3}(\mathrm{m^{-3}}). \tag{5.22}$$

The principal quantum number, $n$, required in the $ns \rightarrow np$ transitions for different observable $E_{max}(n_p)$ scales as,

$$E_{max}(n_p) \propto \frac{1}{n^5}. \tag{5.23}$$

These relationships may be used to determine the maximum $n$ which can be used to measure a plasma density.

It is desirable to work at the highest $n$ possible. Polarizability increases with $n$, therefore as $n$ increases, sensitivity to low electric fields improves. However, exciting the atoms to high $n$ states is limited by the laser linewidth. The line broadening of the transitions due to the laser linewidth, makes the higher $n$ ($n > 61$) states unresolvable (Fig. 3-2).

The highest $n$ states that the atoms can be selectively excited to, with the present dye laser linewidth ($FWHM \approx 14\,\mathrm{GHz}$), is $n = 61$. The transition frequency of the $61s_{1/2} \rightarrow 61p_{1/2}$ resonances is equal to $15.97\,\mathrm{GHz}$, which can be generated using the same microwave generator that was used to drive the $47s_{1/2} \rightarrow 47p_{1/2}$ transitions. The maximum electric field observable in this case is $E_{max}(n_p) \approx 6.09\,\mathrm{V\,/\,cm}$.

Low electric fields such as microfields (Sec. 1.3) are expected to be detectable. This is in contrast to the previous work on the detection of the electric fields induced by a non-neutral plasma in a MOT [15], in which only electric fields as low as $12\,\mathrm{V\,/\,cm}$ were detected by optical excitation.

# Chapter 6

# Summary and Future Work

Rubidium atoms were laser cooled and trapped in a magneto optical trap (MOT) by semiconductor diode lasers ($\sim 780\,\text{nm}$). The frequencies of the diode lasers were locked and stabilized using dichroic atomic-vapor laser lock (DAVLL) and saturated absorption spectroscopy (SAS) techniques. The cooled and trapped atoms were excited to the Rydberg states ($47s_{1/2}$) using a tunable modeless dye laser ($\sim 480\,\text{nm}$) being pumped by the third harmonic of a Nd:YAG laser ($355\,\text{nm}$). Microwaves were used to drive the transitions from the $47s_{1/2}$ states to the $47p_{1/2}$ states. The Rydberg atoms were detected using selective field ionization (SFI).

The power broadening of the microwave transitions was studied experimentally. The effect of inhomogeneous magnetic fields, inherent in the MOT, on the microwave transitions of the Rydberg atoms was reduced by switching the AHC's current on and off. This improved the spectral resolution.

Taking advantage of the fact that highly excited Rydberg atoms are sensitive to electric fields due to their loosely bound orbits, the spectral shifting of the microwave transitions ($47s_{1/2} \rightarrow 47p_{1/2}$) were observed and used for measurement and compensation of the stray electric fields present at the trap region. The electric field distributions due to two typical cold plasma densities were estimated using the Holtsmark distribution.

Using the techniques and the results described in this thesis, it is planned to use the millimeter wave transitions as a probe of electric fields in a plasma. This requires another dye laser to be added to the present set up in order to partially ionize the trapped atoms and make an ultra-cold neutral plasma (UCNP). Expansion of the UCNP can be studied by observing the

evolution of the microfields and the macroscopic electric fields as the time delay between the two dye laser pulses is varied.

The Stark line broadening of the spectra obtained in this work can be used to determine the electric field distribution, $P(\beta)$, in an expanding UCNP. The use of a dye laser with a narrower bandwidth (less than 14 GHz FWHM ) would allow excitation of atoms to higher Rydberg states. Hence, more precise measurements of the detailed $P(\beta)$ can be obtained. As concluded in Sec. 5.4, unlike the previous work on the detection of the electric fields induced by a non-neutral plasma in a MOT [15], low electric fields such as microfields will be detectable. If the detected microfields follow the Holtsmark distribution, the density of the expanding UCNP can be measured. However, if the detected microfields do not follow the Holtsmark distribution, the positions of charged particles in the plasma are correlated. Precise measurements of $P(\beta)$ could reveal Wigner crystallization [59].

# Bibliography


[1] Thomas. F. Gallagher, *Rydberg Atoms*, Cambridge, first edition, 1994.

[2] J. P. Connerade, *Highly Excited Atoms*, Cambridge, 1998.

[3] National Institute of Standards and Technology, *The NIST Reference on Constants, Units, and Uncertainty: Conversion factors for energy equivalents*, http://physics.nist.gov/cuu/Constants/energy.html, 1998.

[4] P. Filipovicz, P. Meystre, and G. Rempe nd H. Walther, "Rydberg atoms - A testing ground for quantum electrodynamics," *Optica Acta*, vol. 32, pp. 1105–1123, 1985.

[5] W. E. Lamb, Jr., and T. M. Sanders, "Fine structure of n=3 Hydrogen by a radio-frequency method," *Phys. Rev.*, vol. 103, pp. 313, 1956.

[6] P. Goy, J. M. Raimond, G. Vitrant, and S. Haroche, "Millimeter-wave spectroscopy in cesium Rydberg states. Quantum defects, fine- and hyperfine-structure measurements," *Phys. Rev. A.*, vol. 26, pp. 2733.

[7] F. Merkt and H. Schmutz, "Very high resolution spectroscopy of high Rydberg states of the argon atom," *J. Chem. Phys.*, vol. 108, pp. 10033–10045, 1998.

[8] Wenhui Li, I. Mourachko, M. W. Noel, and T.F. Gallagher, "Millimeter-wave spectoscopy of cold Rb Rydberg atoms in a magneto-optical trap: Quantum defects of the ns, np, and nd series," *Phys. Rev. A.*, vol. 67, pp. 052502–1, 2003.

[9] F.F. Chen, *Introdution to Plasma physics*, Plenum, 1974.

[10] T.C. Killian, S. Kulin, S.D. Bergeson, L. A. Orozco, and S. L. Rolston, "Creation of an ultracold neutral plasma," *Phys. Rev. Lett.*, vol. 83, pp. 4776, 1999.

[11] B. N. Ganguly, "Measurement of high Rydberg $^1$P spectra of atomic helium and its application to glow-discharge diagnostics," *J. Appl. Phys.*, vol. 60, pp. 571, 1986.

[12] J. R. Shoemaker, B. N. Ganguly, and A. Garscadden, "Stark spectroscopic measurement of spatially resolved electric field and electric field gradients in a glow discharge," *Appl. Phys. Lett.*, vol. 52, pp. 2019, 1988.

[13] G. A. Hebner, K. E. Greenberg, and M. E. Riley, "Electric fields in high-frequency parallel-plate helium discharges," *J. Appl. Phys.*, vol. 76, pp. 4036, 1994.

[14] J. Neukammer, H. Rinneberg, K. Vietzke, A. Konig, H.Hieronymus, M. Kohl, H.-J. Grabka, and G. Wunner, "Spectroscopy of Rydberg atoms at n$\sim$500 : Observation of Quasi-Landau resonances in low magnetic fields," *Phys. Rev. Lett.*, vol. 59, pp. 2947, 1987.

[15] D. Feldbaum, N. V. Morrow, S. K. Dutta, and G. Raithel, "Coulomb Expansion of Laser-Excited Ion Plasmas," *Phys. Rev. Lett.*, vol. 89, pp. 173004–1, 2002.

[16] K. B. MacAdam, Steinbach, and C. Wieman, "A narrow-band tunable diode laser system with grating feedback, and saturated absorption spectrometer for Cs and Rb," *Am. J. Phys.*, vol. 60, pp. 1098, 1992.

[17] Kristan L. Corwin, Zheng-Tian Lu, Carter F. Hand, Ryan J. Epstein, and Carl E. Wieman, "Frequncy-stablized diode laser with the Zeeman shift in an atomic vapor," *Appl. Opt.*, vol. 37, pp. 3295, 1998.

[18] E. Raab, M. Prentiss, A. Cable, S. Chu, and D. Pritchard, "Trapping of neutral-sodium atoms with radiation pressure," *Phys. Rev. Lett.*, vol. 59, pp. 2631, 1987.

[19] P. Ewart, "A modeless, variable bandwidth, tunable laser," *Opt. Commun.*, vol. 55, pp. 124, 1985.

[20] S. Kulin, T. C. Killian, S.D. Bergeson, and S.L. Rolston, "Plasma oscillations and expantion of an ultracold neutral plasma," *Phys. Rev. Lett.*, vol. 85, pp. 318, 2000.

[21] C. S. Adams and E. Riis, "Laser cooling and trapping of neutral atoms," *Progress In Quantum Electronics*, vol. 21, pp. 1–79, 1997.

[22] W. R. Anderson, "Resonant dipole-dipole collisions of Rydberg atoms in a magneto-optical trap," Ph.D. Thesis. University of Virginia, Charlottesville, VA, USA, 1996.

[23] H. J. Metcalf and P. van der Straten, *Laser Cooling and Trapping*, Springer, 1999.

[24] E. Arimondo, M. Inguscio, and P. Violino, "Experimental determinations of the hyperfine structure in the alkali atoms," *Rev. Mod. Phys.*, vol. 49, pp. 31, 1977.

[25] H. Batelaan, S. Padua, D. H. Yang, C. Xie, R. Gupta, and H. Metcalf, "Slowing of Rubidium(85) atoms with isotropic light," *Phys. Rev. A*, vol. 49, pp. 2780, 1994.

[26] Duniway Stockroom Corp.

[27] T. Bergeman, G. Erez, and H. J. Metcalf, "Magnetostatic trapping fields for neutral atoms," *Phys. Rev. A*, vol. 35, pp. 1535, 1987.

[28] Alcatel Scanwire.

[29] D. R. Lide, *CRC Handbook of Chemistry and Physics*, CRC Press, Boca Raton, 1990.

[30] Christopher D. Wallace, Timothy P. Dinneen, Kit-Yan N. Tan, Timothy T. Grove, and Phillip L. Gould, "Isotopic difference in trap loss collisions of laser cooled rubidium atoms," *Phys. Rev. Lett.*, vol. 69, pp. 897, 1992.

[31] M. Fedorov, private communication.

[32] J. Mason, private communication.

[33] C. E. Wieman and L. Hollberg, "Using diode lasers for atomic physics," *Rev. Sci. Instrum.*, vol. 62, pp. 1, 1991.

[34] W. Demtroder, *Laser Spectroscopy: basic concepts and instrumentation*, Springer, second edition, 1996.

[35] Daryl W. Preston, "Doppler-free saturated absorption: Laser spectroscopy," *Am. J. Phys.*, vol. 64, pp. 1432, 1996.

[36] P. Haghnegahdar, private communication.

[37] C. Wieman and G. Flowers, "Inexpensive laser cooling and trapping experiment for udergraduate laboratories," *Am. J. Phys*, vol. 63, pp. 317, 1995.

[38] C. E. Moore, *Atomic energy levels, Vols. I, II and III (NSRDS-NBS35)*, U.S. Goverment Printing Office, Washington, D.C., 1971.

[39] J. Carter, private communication.

[40] M. G. Littman and H. J. Metcalf, "Spectrally narrow pulsed dye laser without beam expander," *Appl. Opt.*, vol. 17, pp. 2224, 1978.

[41] A. R. Striganov and N. S. Sventitskii, *Tables of spectral lines of neutral and ionized atoms*, IFI/Plenum, 1968.

[42] N. J. Dovichi, D. S. Moore, and R. A. Keller, "Use of the optogalvanic effect and the Uranium atlas for wavelength calibration of pulsed lasers," *Appl. Opt.*, vol. 21, pp. 1468, 1982.

[43] R. F. Stebbings and F. B. Dunning, *Rydberg states of atoms and molecules*, Cambridge University Press, 1983.

[44] A. Mugford, private communication.

[45] J. Keller, private communication.

[46] El-Mul Technologies Ltd.

[47] W. Kong, "Photoionization spectroscopy of small molecules using coherent extreme ultraviolet radiation," Ph.D. Thesis. University of Waterloo, Waterloo, On, Canada, 1993.

[48] M. O. Scully, W. E. Lamb, and M. Sargent, *Laser Physics*, Reading, Mass. : Addison-Wesley, Advanced Book Program, 1974.

[49] D. Vagale, private communication.

[50] P. Lorrain, D. R. Corson, and F. Lorrain, *Electromagnetic fields and waves*, Freeman, third edition, 1987.

[51] G. K. Woodgate, *Elementary Atomic Structure*, Oxford, second edition, 1980.

[52] H. G. Kuhn, *Atomic Spectra*, Longmans, first edition, 1962.

[53] Wenhui Li, private communication, Three corrections were made to this equation compared to Eq. (3) of Ref. [8]: 1- The first numerical factor with the unit (THz) should be 86.9357(7) THz, instead of 869357(7). 2- The second numerical factor with the unit (GHz) should be 23.3(5) THz, instead of 233(5) GHz . 3- Both units should be in THz.

[54] E. Luc-Koenig and A.Bachelier, "Systematic theoretical study of the Stark spectrum of atomic hydrogen : Density of continuum states," *J. Phys. B*, vol. 13, pp. 1743, 1980.

[55] M.L. Zimmerman, M. G. Littman, M. M. Kash, and D. Kleppner, "Stark structure of the Rydberg states of alkali-metal atom," *Phys. Rev. A.*, vol. 20, pp. 2251–2275, 1979.

[56] A. Osterwalder and F. Merkt, "Using high Rydberg states as electric field sensors," *Phys. Rev. Lett.*, vol. 82, pp. 1831, 1999.

[57] H. Margenau and M Lewis, "Structure of spectral lines from plasmas," *Mod. Phys.*, vol. 31, pp. 569, 1959.

[58] S. Chandrasekhar, "Stochastic problems in physics and astronomy," *Rev. Mod. Phys.*, vol. 15, pp. 1, 1943.

[59] S. Ichimaru, "Strongly coupled plasmas: high-density classical plasmas and degenerate electron liquids," *Rev. Mod. Phys.*, vol. 54, pp. 1017, 1982.